University of Massachusetts Amherst
ScholarWorks@UMass Amherst

Doctoral Dissertations | Dissertations and Theses

April 2021

SEISMIC CHARACTERISTICS OF THE EASTERN NORTH AMERICAN CRUST AND UPPER MANTLE: THE FORMATION AND EVOLUTION OF CONTINENTAL LITHOSPHERE

Cong Li
University of Massachusetts Amherst

Follow this and additional works at: https://scholarworks.umass.edu/dissertations_2

 Part of the Geophysics and Seismology Commons

Recommended Citation

Li, Cong, "SEISMIC CHARACTERISTICS OF THE EASTERN NORTH AMERICAN CRUST AND UPPER MANTLE: THE FORMATION AND EVOLUTION OF CONTINENTAL LITHOSPHERE" (2021). *Doctoral Dissertations*. 2118.
https://doi.org/10.7275/20225236 https://scholarworks.umass.edu/dissertations_2/2118

This Open Access Dissertation is brought to you for free and open access by the Dissertations and Theses at ScholarWorks@UMass Amherst. It has been accepted for inclusion in Doctoral Dissertations by an authorized administrator of ScholarWorks@UMass Amherst. For more information, please contact scholarworks@library.umass.edu.

SEISMIC CHARACTERISTICS OF THE EASTERN NORTH AMERICAN CRUST AND UPPER MANTLE: THE FORMATION AND EVOLUTION OF CONTINENTAL LITHOSPHERE

A Dissertation Presented
by
Cong Li

Submitted to the Graduate School of the
University of Massachusetts Amherst in partial fulfillment
of the requirements for the degree of

DOCTOR OF PHILOSOPHY

February 2021

Department of Geosciences

© Copyright by Cong Li 2021

All Rights Reserved

SEISMIC CHARACTERISTICS OF THE EASTERN NORTH AMERICAN CRUST AND UPPER MANTLE: THE FORMATION AND EVOLUTION OF CONTINENTAL LITHOSPHERE

A Dissertation Presented

by

Cong Li

Approved as to style and content by:

_____
Haiying Gao, Chair

_____
Michael L. Williams, Member

_____
Vadim Levin, Member

_____
Michele Cooke, Member

_____
Laurie Brown, Member

_____
Ching S. Chang, Member

_____

_____
Stephen J. Burns, Department Head
Department of Geosciences

ACKNOWLEDGMENTS

I would like to express my gratitude to my advisor, Prof. Haiying Gao, for the supervision and support with projects in this thesis. I am so grateful to have learned many life-long skills under her supervision. She always generously supports me to participate in a variety of academic conferences and encourages me to pursue my own ideas. I cannot thank her enough for her time and motivation throughout my Ph.D journey. I would like to thank Prof. Michael Williams, who inspires me to study geology and plate tectonics. I thank Prof. Vadim Levin for his continual help with various questions on receiver function analysis. I benefit from every discussion with Michael and Vadim, as well as their enthusiasm and attitude for science. I appreciate their collaboration and thank for their effort on reading and revising the manuscripts we have published. In addition, I am very grateful to Prof. Michele Cooke for introducing me mechanical modeling and tectonophysics and for advising me on academic matters. I would also like to express my appreciation to Prof. Maureen Long, Prof. Laurie Brown, and Prof. Donald Wise for their thoughtful discussions and suggestions and comments on my studies. I thank Prof. Ching-Shung Chang for kindly agreeing to join my thesis committee and reading every page of this thesis. I am also very grateful to my colleagues and friends who are part of my daily life as a graduate student, especially Carrie Glauner, Kevin Toeneboehn, Phillip Geer, Kaitlyn Suarez, Anna Ruth Halberstadt, Xiaotao Yang, Sampath Rathnayaka, Meng Liu, and Boyang Zhao.

Last but not least, I am especially grateful to my parents and my fiancée for constantly encouraging me to purse my academic goal. I cannot get by without their kind support. I

am sincerely appreciate that they are always there for me and are always proud of me. Their love and support mean the world to me!

ABSTRACT

Seismic Characteristics of the Eastern North American Crust and Upper Mantle: The Formation and Evolution of Continental Lithosphere

February 2021

Cong Li,

B.S., Ocean University of China
M.S., Institute of Crustal Dynamics, Chinese Earthquake Administration
Ph.D., University of Massachusetts Amherst

Directed by: Professor Haiying Gao

The impact of past tectonic events on formation and modification of continental lithosphere over the course of Earth's history remains as an open question of fundamental importance. Physical properties of continental crust and mantle lithosphere, such as their age, thickness, composition, temperature, and velocity, contain crucial information for informing this question. Eastern North America provides at least two complete records of supercontinent assembly and breakup over the past 1.3 Ga, serving as a natural laboratory for our understanding of continental lithosphere evolution and for integrating geologic and geophysical observations.

In this thesis, I have investigated the seismic properties of crust and upper mantle beneath eastern North America with different seismological methods. I first used teleseismic P-wave receiver function analysis to investigate the crustal thickness distribution beneath eastern North America, in order to explore the possible linkage between geologically-defined boundaries and the variation of crustal thickness. The results show a significant

variation in the depths of the Moho and intra-crustal layers within and across the major tectonic units. Specifically, there are distinct differences in crustal thickness between the northern and southern Grenville Province. A dipping intra-crustal feature can be seen within the central Grenville Province, with the depth increasing eastward from 5 to 27 km. The Moho depth decreases southeastward across the Grenville-Appalachian boundary, with a sharp Moho offset of up to 12-15 km in the central segment and a more gradual variation to the north and south. The thickness difference between the southern and northern Grenville-aged crusts suggests different tectonic and/or exhumation histories during and after the Grenville Orogeny. The low-angle eastward dipping crustal feature is interpreted to be a Grenville-aged collisional structure. Differences in the steepness of the Moho offset along the strike of Appalachians probably reflect variation of the steepness of the subsurface boundary between Laurentia and accreted terranes with different intensities of post-orogenic modification. The observed spatial relation between the geologically defined tectonic boundaries and crustal thickness variations provides new constraints on the depth extent of the tectonic units within the crust.

I then used full-wave ambient noise tomography to construct a high-resolution velocity model beneath the southern part of eastern North American margin. The goal is to understand the impact of rifting-related tectonism on the modification of lithospheric structure. The velocity model demonstrates a clear crustal thickening over a transitional zone from ocean to continent, a lower-than-average mantle lithospheric velocity underlying the transitional crust, and a nearly vertical low-velocity column in the uppermost mantle beneath the Virginia volcanoes. I propose that the initial rifting formed the transitional

oceanic-continental crust, and the underlying mantle lithosphere had been partially melted or thermally and chemically modified during and after rifting. A rifting-induced mantle convection flow, together with possible lithospheric delamination, may explain the low-velocity column and volcanism observed within the continental interior.

My study provides tight constraints on the crustal thickness distribution and lithospheric velocity variation beneath eastern North America. These seismic characteristics, together with constraints from other geological and geodynamic studies, have significant insights on the formation and modification of the eastern North American lithosphere through geologic time.

Abstract

TABLE OF CONTENTS

Page

LIST OF FIGURES

Figure Page

Table of Figures

Table of Figures

CHAPTER 1

Introduction

1.1. Importance of eastern North America on understanding of lithosphere evolution

The lithosphere is an outer rigid shell of Earth, which comprises the crust and uppermost mantle. It has experienced a complex process of evolution over the past ~4.5 Ga (Stanley, 1999). Based on the theory of plate tectonics, the Earth's lithosphere is composed of multiple plates which float on a ductile mantle. The rifting process can break up a continental plate into two pieces and form a new ocean basin between them. In the following stages, the two separated continental plates converge back together, leading to mountain building, subduction of oceanic slab, and ultimately the closure of ocean basin. The cycle of opening and closing ocean basins is commonly known as the Wilson cycle, which provides a basic mechanism for the Earth's dynamics.

A fundamental question remains concerning how past rifting and collisional events had formed and modified the structures of lithosphere over the course of geologic time. Eastern North America recorded at least two complete Wilson cycles from assembly of the supercontinent Rodinia to the formation of the modern Atlantic Ocean over the last 1.3 Ga (Heaman & Kjarsgaard, 2000; Thomas, 2006). A variety of geological and geophysical features associated with continental collisional and rifting processes have been well preserved in this region (Hatcher, 2010; Thomas, 2006; Li et al., 2018, 2020; Long et al., 2019; Lynner & Porritt, 2017). Eastern North America therefore serves as a superb setting to advance our understanding of the formation and evolution of lithosphere through geologic time.

1.2. Geological history of eastern North America

Eastern North America involves three major tectonic units (Figure 1.1 a), including the North American craton (~3.8-1.3 Ga), the Grenville Province (~1.3-0.98 Ga), and the Appalachian orogenic region (~495-280 Ma) (David et al., 2009; Hatcher, 2010; McLelland et al., 2010, 2013). The North American craton was formed by the amalgamation of several cratonic blocks, including the Archean Superior Craton, the Paleoproterozoic Penokean Province, and the Mesoproterozoic Granite-Rhyolite Province (Card, 1990; McLelland et al., 2010, 2013; Percival et al., 2004; Whitmeyer & Karlstrom, 2007). The Grenville Province involved a series of collisional and extensional events that ultimately resulted in the assembly of the supercontinent Rodinia (Hynes & Rivers, 2010; Rivers, 1997). The Grenville-aged crust experienced different degrees of extensional collapse and erosion after amalgamation (Jamieson et al., 2010; McLelland et al., 2010, 2013). The breakup of Rodinia at ~750 Ma (Hatcher, 2010) led to rifting along the eastern margin of the Grenville Province (Rimando & Benn, 2005).

The Appalachian orogen was formed during the assembly of the supercontinent Pangea from approximately 495 to 280 Ma and involved a sequence of terrane accretion events and the ultimate collision of Laurentia with Gondwana (Hatcher, 2010; van Staal et al., 2009). In the northern Appalachian region, three major exotic terranes have been recognized (Figure 1.1a): from oldest (inboard) to youngest (outboard), the Taconic belt (and possible Moretown terrane), the Gander terrane, and the Avalon terrane (Hatcher, 2010; Karabinos et al., 2017; van Staal et al., 2009). In the southern Appalachians, two major terranes have been recognized, including the Inner Piedmont terrane and the large

exotic Carolina Superterrane (Thomas, 2006). After assembly, several stages of Mesozoic rifting and exhumation ultimately resulted in the modern continental margin (Hatcher, 2010; Thomas, 2006).

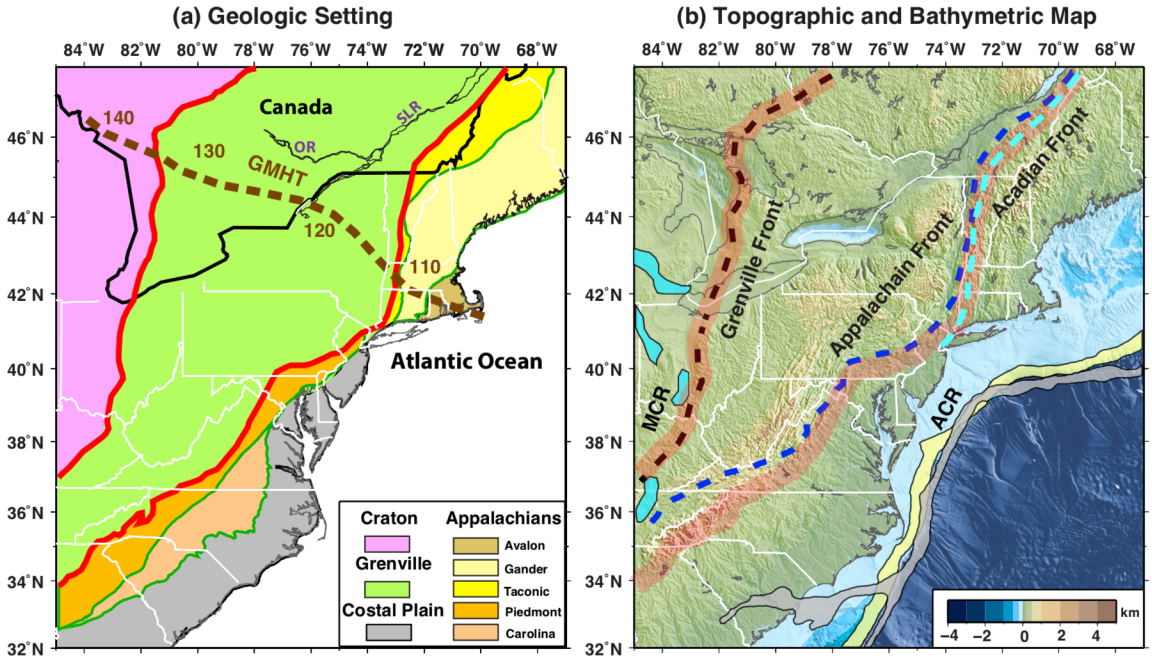

Figure 1.1 (a) Geological map showing the major tectonic units in eastern North America, modified after the lithotectonic map of the Appalachian orogen by Hibbard et al. (2006) and the United States Geological Survey basement domain map (http://mrdata.usgs.gov/ds-898/). The two thick red lines mark the inferred North American craton-Grenville boundary and the Grenville-Appalachian boundary. The dark green lines mark the boundaries between the tectonic subprovinces of Inner Piedmont-Carolina-coastal plain in the southern Appalachian region and Taconic Belt-Gander-Avalon in the northern Appalachian region. The brown dashed line indicates the proposed Great Meteor hot spot track (GMHT), marked with time in Ma. (b) Topographic and bathymetric map in eastern North America. The black, blue, and cyan dashed lines mark the Grenville deformation front, the Appalachian deformation front,

and the Acadian deformation front, respectively. The red shadow zones mark the inferred major tectonic boundaries as shown by the red lines in (a). The cyan patches denote the positive gravity anomaly associated with inferred eastern arm of the Midcontinent Rift (MCR). The yellow and gray patches denote the positive gravity anomaly and the East Coast magnetic anomaly, respectively, which mark the location of Atlantic Continental Rift (ACR). The background color is the bathemetry/topography.

Three first-order deformation fronts, the Grenville Front, the Appalachian Front, and the Acadian Front, can be recognized in parts of eastern North America (Figure 1.1 b). The Grenville Front follows the inferred tectonic boundary between the North American craton and the Grenville Province (Figure 1.1 b). This front has been interpreted as a contractional fault system, dating from the Grenville orogeny. It separates the low metamorphic-grade North American craton from the high-grade outcrops in the Canadian Grenville Province (McLelland et al., 2010). The Grenville Front has been traditionally assumed to extend southward into Ohio and Kentucky in the United States (e.g., Stein et al., 2018a, 2018b), where it is not exposed at the surface. The Appalachian Front is a structurally defined boundary between rocks deformed or transported westward during Appalachian orogenesis and flat-lying Paleozoic rocks and underlying Grenville-aged rocks to the west (Mount, 2014). Grenville-aged rocks have been interpreted beneath Paleozoic rocks to the east of the Appalachian Front in the northern and southern Appalachians, suggesting the subsurface extension of the Grenville terrane under accreted Appalachian elements (e.g., Cook & Vasudevan, 2006; Figure 1.1 b). The Acadian Front is the northern and central Appalachian boundary between rocks (and structures) deformed or reactivated during the

Devonian Acadian orogeny and rocks deformed by earlier Paleozoic or Precambrian events (Bradley et al., 2000; Robinson et al., 1998). Acadian orogenesis has not been widely recognized in the southern Appalachians (Hibbard & Karabinos, 2013).

In addition, two groups of gravity (and magnetic) anomalies are observed in eastern North America, which have been interpreted to be associated with rifting processes over the past 1.3 Ga. The first group of positive gravity anomalies might represent the eastern arm of 1.1-Ga failed Midcontinent Rift (Stein et al., 2018a, 2018b), which extends from southern Michigan and Ohio into Kentucky along the southern Grenville Front (cyan patches in Figure 1.1b). This failed rifting promoted high-density mafic rocks into the crust, leading to the observed gravity anomalies along the Grenville Front (Thomas & Teskey, 1994; Stein et al., 2018a). The second group of gravity and magnetic anomalies marks the location of offshore rifting which contributed to the opening of Atlantic Ocean at ~230 Ma (Austin et al., 1990; Bonvalot et al., 2012; Kiltgord et al., 1988). Those anomalies align approximately along the continental shelf (yellow and gray patches in Figure 1.1b). Previous studies suggest that igneous rocks with magnetic materials underplated or intruded into the crust along the passive margin during the Atlantic rifting, responsible for observed gravity and magnetic anomalies (e.g., Austin et al., 1990; Holbrook et al., 1994).

1.3. Teleseismic receiver function analysis and full-wave ambient noise tomography

In this thesis, we used teleseismic P-wave receiver function analysis to investigate the crustal thickness variations beneath eastern North America and used full-wave ambient noise tomography to image the lithospheric velocity structures.

Teleseismic P-wave receiver function analysis uses P-to-S converted wave to identify discontinuities of velocity (and density) in the Earth. Therefore, this method is appropriate for investigating variations of crust-mantle boundary. The principle of teleseimsic receiver function analysis is rooted in the ray-theoretical assumption of seismic wavefield propagation over velocity discontinuities (Rondenay, 2009). When a teleseismic P-wave encounters a velocity discontinuity such as the crust-mantle boundary (the Moho), the upward incident P-wave will partition into converted P-to-S (Ps) wave (Figure 1.2a). An arrival time delay between P-wave and Ps-wave is expected to be observed in the seismograph, considering that the P-wave velocity is faster than the S-wave velocity (Figure 1.2b). This arrival time delay contains important information about the depth of discontinuity and about the P-wave and S-wave velocities. Furthermore, the relative amplitudes between these P-wave and Ps-wave can be used to estimate the magnitude of velocity change across the discontinuity (Ammon, 1991; Cassidy 1992; Rondenay, 2009).

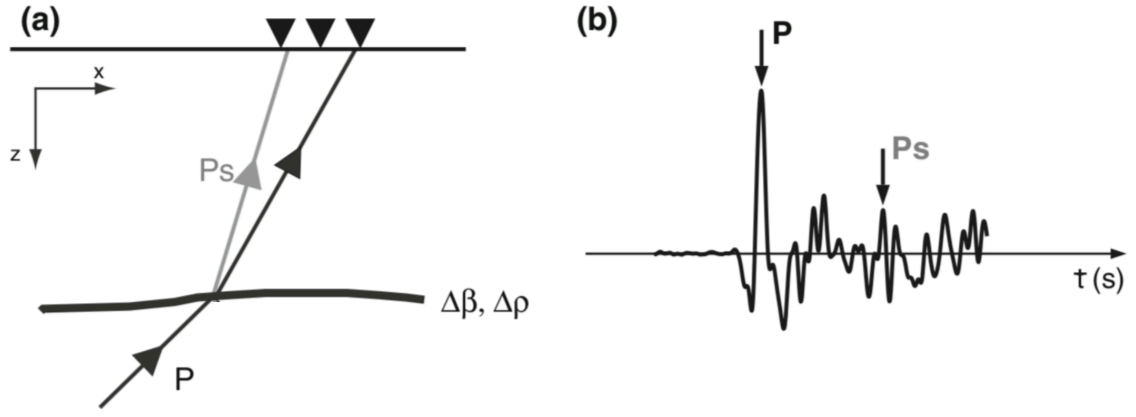

Figure 1.2. Schematic figures showing a) the partitioning of a P-wave incident upon a sub-horizontal discontinuity in S-wave velocity and/or density, and b) the resulting

seismogram. The converted, upward propagating S-wave is the basis of the receiver function technique. The time delay between the incident P and converted Ps waves is related to the depth of the discontinuity, whereas the amplitude of Ps relative to P is indicative of the magnitude of the change of velocity and density. Modified from Rondenay (2009).

Tomography is a common technique in seismology for imaging the Earth's interior structures. Traditional tomographic methods take advantage of arrival time and amplitude of earthquake waves (including body waves and surface waves) in order to infer subsurface velocity structures. The application of those methods therefore are limited by the distribution of earthquakes (Thurber & Aki 1987; Montagner 1994; Das & Rai, 2016). In addition, because the earthquake waves contain both information of subsurface medium they go through and information of source function, the tomographic results from traditional methods can be biased by the uncertainty of earthquake source estimation (Nolet 2008). Over last decades, an advanced approach known as ambient noise tomography has been put forward and widely used. This method is based on ambient noise generated by wind, ocean waves, rock fracturing and anthropogenic activities that constantly travel through the Earth (Das & Rai, 2016). By cross-correlating long time sequences of ambient noise recorded at two different seismic stations, seismologists can extract the information of subsurface medium between the two stations (commonly called empirical Green's Functions) without effects of source functions. The ambient noise tomography thus can provide better constraints on the velocity structure of Earth in comparison with traditional seismic tomography.

We briefly summarize the procedure of full-wave ambient noise tomography method in Figure 1.3. First, we extract the empirical Green's functions from the cross-correlation of continuous ambient noise between each station pair. Second, we simulate seismic wavefield based on a 3-D spherical velocity model and synthesize waveforms propagating between each station pair. Third, Rayleigh-wave phase delays can be measured between the observed empirical Green's functions and the synthetics at a sequence of overlapping periods. Forth, we calculate the 3-D, finite-frequency sensitivity kernels of Rayleigh waves and carry out the inversion for both P- and S-wave velocity perturbations. The reference model is then iteratively updated until the Rayleigh-wave phase misfits between the observed and synthetic waveforms are small enough and meet the threshold we set.

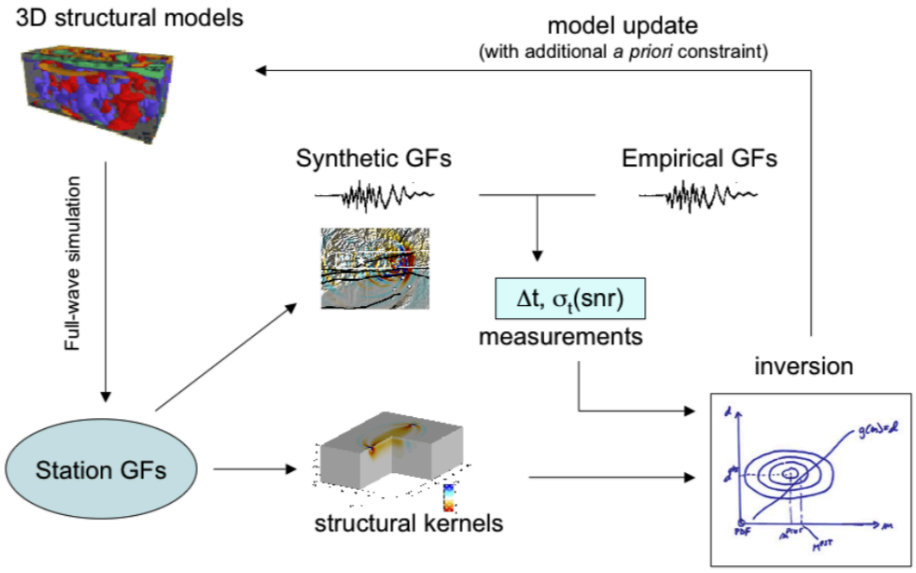

Figure 1.3. Flow chart of full-wave ambient noise tomography. Modified from the user's manual of full-wave ambient noise tomography by Shen et al. (2011)

1.4. Current challenges

Numerous studies have been conducted in eastern North America in order to characterize seismic features within the crust and upper mantle, including active-source seismic surveys (e.g., Ando et al., 1984; Hennet et al., 1991; Hughes & Luetgert, 1991, 1992), P-wave and S-wave receiver function analysis (e.g., Hopper et al., 2017, 2018; Long et al., 2019; Parker et al., 2015), seismic tomography imaging (e.g., Biryol et al., 2016; Lynner & Porritt, 2017; Mustelier & Menke, 2020; Savage et al., 2017; Wagner et al., 2018), seismic anisotropy analysis (e.g., Long et al., 2010, 2016; Lynner & Bodmer, 2017; Wagner et al., 2012) and seismic attenuation analysis (e.g., Byrnes et al., 2019; Dong & Menke, 2017). However, those studies are either regional-scale or are lack of high enough resolution. As a result, a challenge remains concerning how seismologists can provide high-resolution, systematic constraints on lithospheric features for the entire eastern North American region. The Earthscope Transportable Array (IRIS Transportable Array, 2003) and its retaining subset (UC San Diego, 2013) deployment in eastern North America in 2013-2015, together with many other regional seismic networks, has significantly increased the spatial density of broadband observations. This provides a new opportunity to investigate crustal and upper mantle structures beneath eastern North America with a high resolution.

Another challenge is how geoscientists can integrate various geologic and geophysical constraints to understand the formation and evolution process of lithosphere beneath eastern North America. For example, seismic tomography imaging is more sensitive to volumetric velocities, while receiver function analysis is more sensitive to rapid variations of velocity across a discontinuity. Therefore, these two observations provide

complementary constraints on the lithospheric structures beneath eastern North America. In addition, geologic mapping identifies different tectonic terranes and terrane boundaries at the surface, and geochronology studies provide further temporal constraints on these terrane boundaries. Combination of different geologic and geophysical observations thus will give comprehensive insights on the evolution process of lithosphere beneath eastern North America in both temporal and spatial domains.

1.5. Scope of this thesis

The overall goal of this thesis is to understand the impact of past tectonic events on the formation and modification of lithosphere beneath eastern North America. In order to achieve this goal, we investigate the crustal thickness variations beneath eastern North America and image lithospheric velocity distribution beneath the southern part of eastern North American margin. We then interpret those seismic observations by integrating geologic and other geophysical evidences. This thesis is organized as follows:

In **Chapter 2,** we image the distribution of crustal thickness beneath the northern Appalachian mountains using teleseismic P-wave receiver function analysis. The goal of this chapter is to explore the possible relationship between geologically defined tectonic boundaries and variations of crustal thickness. This chapter has been published in Geophysical Research Letters (Li, C., et al. 2018). In **Chapter 3,** we further investigate the variations of Moho depth and intra-crustal layers beneath the entire eastern North American region. The specific questions we address include: 1) Which geologically defined tectonic boundaries can be correlated with subsurface gradients or boundaries in

three-dimensional seismic models? 2) What constraints can seismic data place on the timing and history of these boundaries? This chapter has been published in Journal of Geophysical Research: Solid Earth (Li, C., et al., 2020). In **Chapter 4,** we construct a high-resolution velocity model beneath the southeastern United States by integrating offshore and onshore seismic data using full-wave ambient noise tomography. We focus on the question concerning how past tectonic events had modified the lithospheric velocity structures in the southern part of eastern North America margin. This chapter has been submitted into Geophysical Research Letters and is under review. In **Chapter 5**, the main results of this thesis and proposed future research directions are summarized and discussed.

CHAPTER 2

Crustal thickness variation in the northern Appalachian mountains: Implications for the geometry of 3-D tectonic boundaries within the crust (*Li, C., Gao, H., Williams, M. L., & Levin, V. (2018). Crustal thickness variation in the northern Appalachian Mountains: Implications for the geometry of 3-D tectonic boundaries within the crust. Geophysical Research Letters, 45, 6061–6070. https://doi.org/10.1029/ 2018GL078777*)

2.1. Introduction

The northern Appalachian Mountains include a series of iconic orogenic belts, which have recorded two complete Wilson Cycles from the assembly of the (~1000 Ma) supercontinent Rodinia to the formation of the modern Atlantic Ocean (Heaman & Kjarsgaard, 2000; Thomas, 2006). The first Wilson Cycle began with the assembly of Rodinia, which may have established the fundamental oroclinal geometry of the subsequent collisional margin (Rivers, 2015; Thomas, 1977, 2006). The breakup of Rodinia opened the Iapetus Ocean by 530 Ma (Thomas, 2006). The second Wilson Cycle started at ~480 Ma with a sequence of accretion events involving continental and oceanic terranes (Hatcher, 2010; van Staal et al., 2009). These accreted terranes, from west to east, can be divided into at least three parts (Figure 2.1): the Taconic belt, a peri-Laurentian element interpreted to have been accreted during the Ordovician Taconic orogeny; the peri-Gondwanan Gander terrane (± Moretown terrane) that occupies a large part of central New England and may have accreted in the Salinic orogeny; and the Avalon terrane, accreted during the Acadian orogeny (Hibbard et al., 2006, 2007; Karabinos et al., 2017). Subsequent collisional events involved the accretion of the Meguma Terrane (outboard of Avalon) and ultimately collision with

Gondwana during the Alleghenian orogeny (Domeier, 2016; van Staal et al., 2009). After assembly, several stages of rifting, exhumation, and possibly orogenic collapse ultimately led to the establishment of the modern passive continental margin by ~180 Ma (e.g., Dorais et al., 2012; Hatcher, 2010; van Staal et al., 2009).

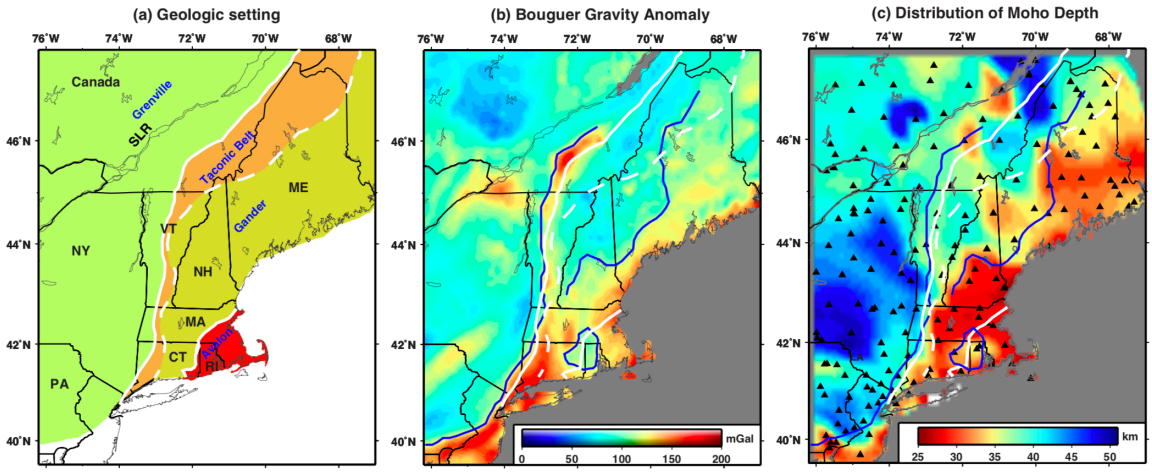

Figure 2.1. (a) Geological map showing the major tectonic units in the northern Appalachian Mountains, modified after the lithotectonic map of the Appalachian orogen by Hibbard et al. (2006) and the United States Geological Survey basement domain map (http://mrdata.usgs.gov/ds-898/). SLR = St. Lawrence River. Black lines mark state boundaries. The white solid lines mark the interpreted Grenville-Taconic and Gander-Avalon boundaries, and the white dashed line is the proposed eastern boundary of Taconic belt by Hibbard et al. (2006) and Karabinos et al. (2017). (b) Distribution of Bouguer gravity anomalies from Bonvalot et al. (2012). (c) Distribution of the Moho depth (in kilometers) extracted from the common conversion point stacking. Black triangles mark the broadband seismic stations used in the calculation of receiver functions. The solid blue lines in Figures 2.1b and 2.1c highlight the sharp gradient in Bouguer gravity discussed in the text.

Geological and geophysical studies have been done to characterize the three-dimensional geometry of the major tectonic units in the Appalachian orogenic belt. The lithotectonic map by Hibbard et al. (2006) provides a first-order compilation of the configuration of tectonic terranes and terrane boundaries in New England and their correlation with the northern and Canadian Appalachian Mountains. The crustal structure has been studied by seismic refraction and reflection methods (e.g., Ando et al., 1984; Hennet et al., 1991; Hughes & Luetgert, 1991, 1992), and by passive seismic methods including receiver function (RF) analysis, wave propagation, tomographic imaging, and surface wave dispersion analysis (e.g., Levin et al., 1995, 2017; Li et al., 2002; Shalev et al., 1991; Taylor & Toksöz, 1982; Viegas et al., 2010). However, due to the relatively sparse station coverage, none of these previous studies was able to characterize the regional-scale crustal seismic structure of the northern Appalachian region. Debates remain about the subsurface extent of the accreted terranes. For example, how does the character of the terranes change along and across orogenic strike, and to what degree do geologically defined surface terranes correlate with variations of seismically defined crustal structure? To answer these questions, a well- constrained three-dimensional crustal model is needed.

The Earthscope Transportable Array (IRIS Transportable Array, 2003) deployment in eastern North America in 2013-2015, retention of many sites by the Central and Eastern United States (UC San Diego, 2013), together with many other regional seismic networks (see supporting information), has significantly increased the spatial density of broadband observations. This provides a new opportunity to investigate the crustal and upper mantle

structure. Here we use teleseismic P-wave RFs to explore the crustal thickness variation from the Atlantic coast to the Grenville Province. The goal of this study is to constrain the geometry of the Moho and crustal thickness of New England, and ultimately to improve our understanding of the impact of past tectonic events on the crustal structure.

2.2. Data and methodology

A total of 87 permanent and 109 temporary broadband seismic stations have been used in this study (see the station distribution in Figures 2.1c and A.1). Descriptions of the various seismic networks are provided in the supporting information. The well-distributed coverage of the broadband seismic stations makes it feasible to obtain a regional-scale Moho geometry using teleseismic RFs. The waveform data were collected from the Incorporated Research Institutions for Seismology Data Management Center for a total of 688 high-quality earthquake events from 1995 to 2016 with body wave magnitude larger than 5.4 at epicentral distance of 30°-95°. The selected teleseismic events demonstrate good back azimuthal coverage from the NW and SW quadrants for the direct P-waves (Figure 2.2), although there are fewer events from the NE and SE quadrants.

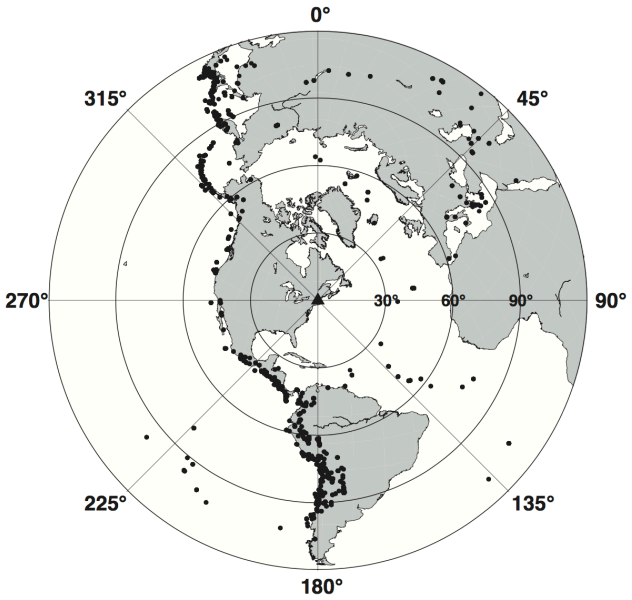

Figure 2.2. Event locations and back-azimuthal coverage for direct teleseismic P-wave arrivals from 1995 to 2016 used for the calculation of receiver functions. The black triangle marks the center of the research region.

The P-wave RFs were obtained using the water level frequency-domain deconvolution method (Ammon, 1991; Langston, 1979; see supporting information). We implemented three steps to evaluate and control the quality of the observed radial-component RFs, based on the primary P_ms phases. First, we visually inspected all of the resulting RFs and manually selected only RFs with signal-to-noise ratios equal to or greater than 3. The signal is referred to as the maximum positive amplitude within the 2-7 s window after the direct P arrival, and the noise is defined as the standard deviation of the 2-10 s waveforms prior to P arrival (see definition in Figure A.2). Second, for each station, data were evaluated to insure that the pattern of the P_ms phase is consistent within similar back azimuth directions. Third, selected RFs were filtered within multiple frequency bands, ranging from 0.05-0.75 Hz and 0.1-1.0 Hz to 0.2-1.2 Hz, to check the stability of the P_ms phases. In total, we selected 5875 RFs. Most long-running stations record high-quality RFs with event numbers ranging from 20 to 190 (Figure A.3 and Table A.1). Some stations, such as LD.PTNY, LD.CFNY, and LD. BNY, have only been operating in recent years, resulting in fewer events selected. The number of RFs for the temporary broadband stations varies within a range of 2-60 (see a detailed description in Table A.1), depending on the operation duration and the data quality. We excluded three EarthScope Transportable Array stations, D62A, E59A, and F62A, due to the poor quality of observed RFs.

The time moveout was applied for the observed RFs with a reference slowness of 0.058 s/km and the IASP91 model in order to correct the impact of ray parameter on P_ms arrival time (Park & Levin, 2016; Yuan et al., 1997; see Figure 2.3). After moveout corrections, individual radial-component RFs from all back azimuths were stacked to represent the average RF for each station. Although the RF patterns at most stations are back azimuth dependent to some extent (Figures 2.3, A.4 and A.5), stacking reduces random variations, increases the signal-to-noise ratio, and highlights the primary phases from major velocity discontinuities. We then automatically picked the time of the maximum positive amplitude of the stacked RF within the time window of 2.5-6.5 s as the average P_ms arrival for each site. The uncertainty of the average P_ms arrival is defined as the standard error of the P_ms arrival times from all the RF events at each station.

To illustrate some of the main features of the radial-component RFs, we describe two permanent stations, US. PKME and NE.BRYW, which demonstrate clear and robust P_ms conversions (see Figures 2.3, A.4 and A.5). For station US. PKME in central Maine, a consistent P_ms signal can be observed at ~3.7 s from all directions, indicating a uniform Moho depth beneath this station. Station NE.BRYW located in Rhode Island shows a clear, distinct P_ms arrival at 3.7-4.6 s. We observe an obvious shift of the P_ms signal from ~4.0 s for events coming from the north to ~4.5 s for events coming from the south. The variation and dependence of the P_ms phase on the back azimuth as observed in this study may be related to a dipping Moho or a combination of dipping Moho and anisotropy. Strong lithospheric anisotropy has been observed beneath eastern North America (e.g., Long et al., 2017; Viegas et al., 2010). However, anisotropy alone would only cause a small amount

of time shift of the P_ms phase from different back azimuths (Levin & Park, 1997). Directional variation in P_ms time on the order of 0.5 s likely requires lateral changes in the Moho depth beneath the site, for example, due to systematic dip. Better directional coverage and the use of transverse component RFs can help resolve such complications for individual sites (see examples in Figures A.4 and A.5). However, this effort falls outside the scope of our regional survey of Moho properties and will be a subject of a follow-up study.

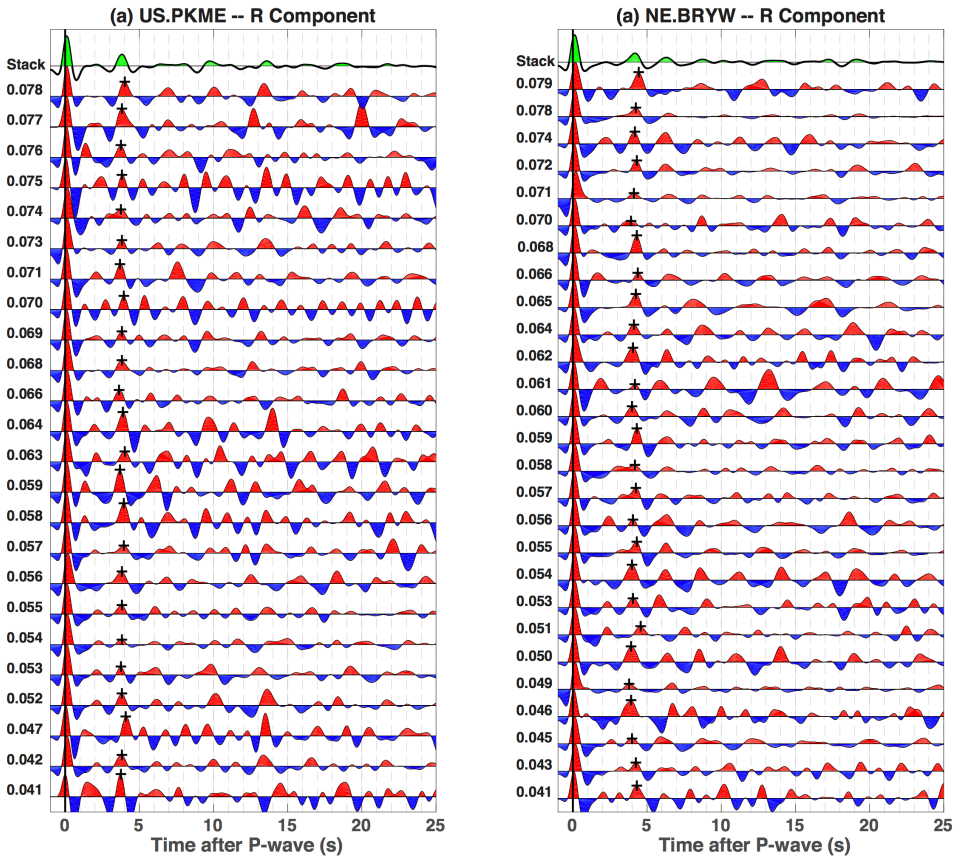

Figure 2.3. Examples of normalized radial-component receiver functions for stations US.PKME and NE.BRYW, sorted by ray parameters. A positive phase (filled with red color) corresponds to a sharp velocity increase with depth. The waveforms are filtered at 0.1-1.2 Hz. The cross signs denote the automatically picked P_ms arrival times. The top

one is the stacked receiver function from all the back-azimuth directions at each station. See station locations in Figure 2.4a.

The RFs were converted to depth using the common conversion point stacking method (Hansen & Dueker, 2009; see supporting information), with the three-dimensional reference velocity model of Shen and Ritzwoller (2016). Shen and Ritzwoller (2016) assumed a constant Vp/Vs ratio of 1.75 in the crust and uppermost mantle. However, the EarthScope Automated Receiver Survey (http://ears.iris.washington.edu) shows that the Vp/Vs ratio varies within a wide range of 1.6-2.1 in the northeastern United States. In order to examine the impact of Vp/Vs ratio on Moho depth estimation, we tested simple RF forward models using the method by Frederiksen and Bostock (2000). Given a P_ms arrival time of 4.5 s, the Moho depth would be 35 km for a crustal Vp/Vs ratio of 1.7 and 39.5 km for a Vp/Vs ratio of 1.9, respectively (Figure A.6). Therefore, a ±4.5 km uncertainty of the Moho depth is expected due to the Vp/Vs ratio alone. We also plotted the piercing point density of the radial-component RFs to demonstrate the spatial resolution of the Moho depth variations (Figure A.7). At 20 km depth, the common conversion point stacking mainly samples the structure directly beneath the seismic station. At 40-km depth, the average RF aperture is about 19 km, similar to the results of Rondenay (2009).

2.3. Results

In this chapter, we focus on the analysis of the P_ms arrival times extracted from the stacked RFs and the corresponding Moho depth, in order to characterize the variation in crustal thickness in our study area. The P_ms time and Moho depth vary from 3 to 6 s and from 27

379 to 52 km, respectively (Figures 2.1c, 2.4a, and A.8). A decrease in crustal thickness can be
380 observed from the Appalachian Plateau toward the Atlantic coast, consistent with previous
381 studies (e.g., Gaherty et al., 2011; Li et al., 2002; Savage et al., 2017; Schmandt et al.,
382 2015; Shen & Ritzwoller, 2016). The lateral distribution of the Moho depth is roughly
383 correlated with the surface topography (Figure A.1) and anticorrelated with the Bouguer
384 gravity anomaly (Figure 2.1b). In general, a lower Bouguer gravity reflects a thicker and/or
385 less dense crust with a higher elevation and vice versa (Li et al., 2003). For example, the
386 thick crust beneath the Appalachian and Laurentian Plateaus correlates with a lower
387 Bouguer gravity anomaly and higher elevation, while the coastal plain has the thinnest crust
388 with a relatively higher Bouguer gravity anomaly and lower elevation.
389
390 We selected three profiles (Figure 2.5) that are nearly perpendicular to the orogenic strike
391 in order to demonstrate the Moho depth variations from the Grenville Province to the
392 accreted terranes along each profile and variations within each tectonic unit by comparing
393 the three profiles. We also provide a NE-SW trending profile in supporting information
394 Figure A.9 to show the Moho depth variations along the strike of the Appalachian terranes.
395 Both the P_ms time and the Moho depth demonstrate a much sharper east-west gradient in
396 the southern part (Figure 2.4; section CC' in Figure 2.5) than in the northern part of the
397 region (Figure 2.4; sections AA' and BB' in Figure 2.5). We observe an offset of the Moho
398 depth of ~15 km within a narrow zone in western Connecticut, western Massachusetts, and
399 southern New Hampshire. For example, the Moho depth is about 45 km and 30 km at
400 stations TA.K61A and TA.L61B that are only 70 km apart (section CC' in Figure 2.5).
401 Note that the actual offset of the Moho depth may differ slightly as our estimate here is

based on the constant Vp/Vs ratio used for the time-depth conversion. According to the EarthScope Automated Receiver Survey (http://ears.iris.washington.edu), Vp/Vs values in this region are between 1.7 and 1.85, thus station-to-station variation in Moho depth due to changes in this parameter cannot exceed 4 km. In contrast, the Moho depth varies more gradually beneath the northern part of the study area. The depth increases on the order of 5-10 km, and the transition appears to be more gradational in northern New England and southeastern Canada compared to southern New England (Figures 2.1c, 2.4, and A.8). For example, between sites CN.A54 and X8.QM15, the Moho depth changes from 47 km to 35 km over a distance of ~300 km.

High lateral resolution derived from the relatively dense coverage of seismic sites highlights small-scale Moho variations. The Moho depth is less than 30 km in southern New England and eastern Maine, and is deeper in northern New Hampshire and western Maine, resulting in a distinct sub-rectangular downward deflection of the Moho along the Atlantic coast (Figures 2.1c and 2.4a). This observed seismic feature is well correlated with the low Bouguer gravity anomaly (Figure 2.1b). A deepening of the Moho was also indicated by previous seismic studies (Hennet et al., 1991; Hughes & Luetgert, 1991; Spencer et al., 1989) but was not well constrained. Local Moho maxima are imaged beneath northern Rhode Island (~35 km; see Figures 2.1c and 2.5) and northwest of the St. Lawrence River in southeastern Canada (~50 km, see Figures 2.1c and 2.5; Levin et al., 2017; Petrescu et al., 2016). Beneath northeasternmost Pennsylvania, a localized Moho minimum (~35 km) corresponds with a local gravity high.

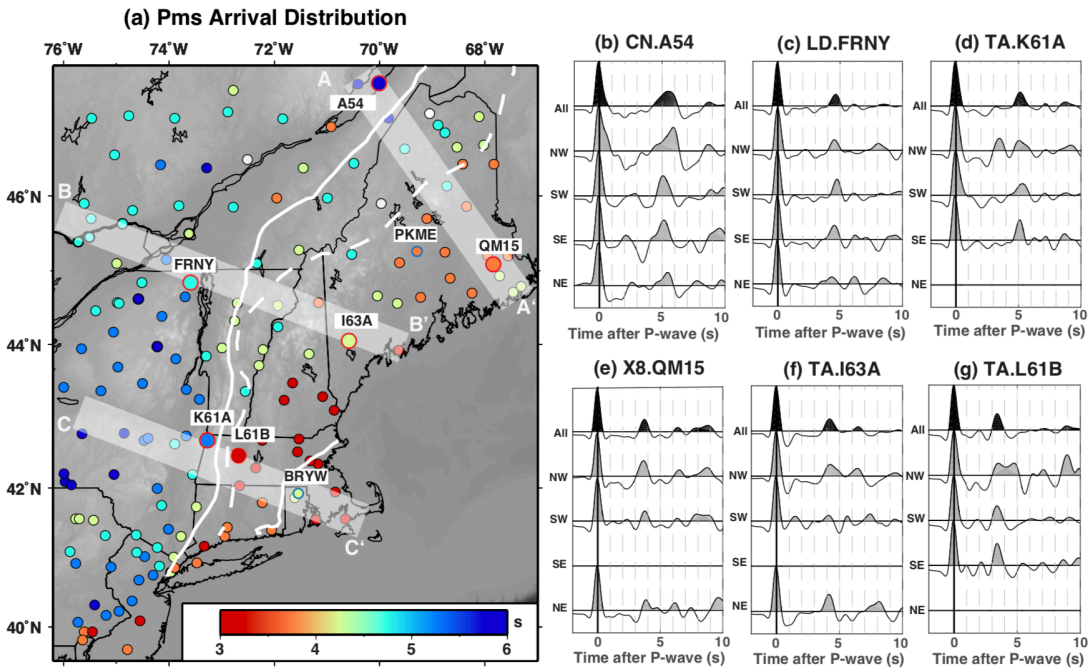

Figure 2.4. (a) Distribution of P_ms arrival time (in seconds), automatically picked from the stacked radial receiver functions for each seismic station. Warm colors denote relatively smaller P_ms arrivals; cold colors denote larger P_ms arrivals. White dots mark stations with poor-quality data. The three shaded zones are profile locations shown in Figure 2.5. The larger dots mark the locations of six selected seismic stations with RFs provided in Figures 2.4b-2.4g (also shown as yellow dots in Figure 2.5). (b-g) Representative radial RFs along AA', BB', and CC' showing variation of P_ms arrivals. The RFs are stacked within each quadrant, ranging within 0-90° (NE), 90-180° (SE), 180-270° (SW), and 270-360° (NW), and from all the back azimuth directions. Waveforms are filtered at 0.1-1.2 Hz. RFs = receiver functions.

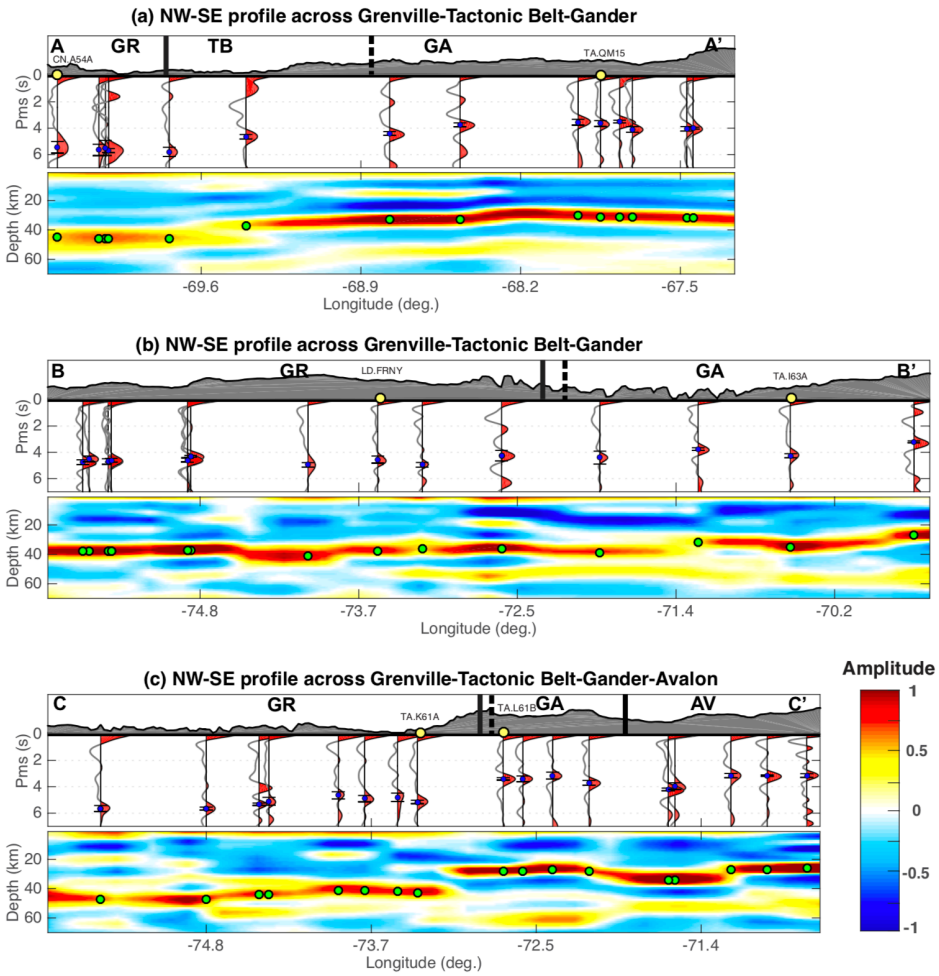

Figure 2.5. Cross sections of stacked radial receiver functions in the time domain along the three profiles (top) and corresponding depth profiles from the common conversion point stacking (bottom). Grey filled lines represent the Bouguer gravity anomalies and major tectonic units boundaries are marked by solid/dashed black lines above each profile. Blue dots denote the P_ms arrival times with estimated uncertainties, and green dots denote Moho depth. AV = Avalon; GA = Gander; TB = Taconic belt; GR = Grenville Province.

2.4. Discussion

Our RF results demonstrate Moho depth variations both across and along the orogenic strike in the northern Appalachian Mountains. Generally, the average P_ms time and Moho depth vary from 4 to 6 s and from 40 to 55 km within the Grenville Province, and 3 to 4.3 s (25 to 35 km) within the accreted terranes (Gander and Avalon; Figures 2.1c, 2.4a, and A.8). In the southern part, the NE-SW trending distribution of the Moho depth roughly follows the trend of major tectonic boundaries (Hibbard et al., 2006). A clear east-west gradient of Moho depth is observed across the eastern margin of the exposed Grenville (Laurentian) basement (section CC' in Figure 2.5). The Moho depth is greater than 45 km in New York within Grenville crust and is less than 30 km across the interpreted Grenville-Taconic Belt boundary (Figures 2.1c and 2.4a). In southern New England, the Moho depth decreases from Grenville to Gander by at least 15 km over a relatively small (70 km) horizontal distance (section CC' in Figure 2.5). The correspondence between the sharp Moho depth variation and the Bouguer gravity anomaly variation (Figure 2.1) further supports the presence of such a distinct crustal thickness change. Only subtle Moho variations are seen farther east, across the Gander and Avalon terranes, with a possible exception of a locally deeper Moho in northernmost Rhode Island.

Several key aspects of the dramatic east-to-west step in Moho depth are important for any interpretation. First, the magnitude of the step decreases from southern to northern New England, from ~15 km in the south to approximately 5 km in the north. Second, the location of the Moho step progressively diverges from the exposed Grenville basement moving

469 northward, roughly corresponding with the widening of the Appalachian orogen from
470 Massachusetts and Connecticut to northern Maine and southeastern Canada. Interestingly,
471 as the Moho step diverges from the Grenville basement northward, it also diverges from
472 the Bouguer gravity anomaly that defines the Appalachian front (Figure 2.1b). The
473 divergence is clear despite the fact that, to some extent, the spatial correlation between
474 Moho depth and surface geology in northern New England is complicated by local
475 anomalies (Figure 2.1c), such as the "subrectangular" downward deflection of the Moho
476 within northern New Hampshire and western Maine (section BB' in Figure 2.5).
477
478 A variety of tectonic processes, at different times in the geologic history, might have
479 contributed to the steep Moho step in southern New England. The step might represent late
480 Paleozoic differential uplift and exhumation of the orogen (Harrison et al., 1989; Wintsch
481 et al., 2003), or it might reflect changes in crustal thickness due to Mesozoic rifting or
482 underplating (Li et al., 2002). However, the close association of the Moho step with the
483 inferred Grenville-to-accreted-terrane boundary and the parallelism with orogenic strike
484 suggest that it may ultimately be related to the fundamental accretionary boundary between
485 Laurentian basement and the exotic terranes. A study of regional seismic wave propagation
486 from an unusually large earthquake in the Adirondacks (Viegas et al., 2010) suggested that
487 the average Vp/Vs ratio and the thickness are about 1.73 and 35 km for the Appalachian
488 crust and 1.80 and 42 km for the Grenvillian crust, respectively. Using RF analysis, Levin
489 et al. (2017) also noted systematic differences in Vp/Vs ratios and crustal thickness values,
490 with Appalachian terranes showing much larger scatter in both parameters, while the region
491 of Grenville Province has a near-uniform Vp/Vs of ~1.75. The difference in Vp/Vs ratio

and crustal thickness has been directly attributed to the difference in crustal compositions as the Grenvillian crust is more mafic than the Appalachian crust (e.g., Musacchio et al., 1997). Due to the sparse coverage of seismic stations within southwestern New England, it is not possible to trace a crustal boundary through the crust from the surface to the Moho. However, we suggest that the distinct Moho offset in southern New England corresponds with a nearly vertical or steep eastward dipping Grenville-Taconic terrane boundary. Previous seismic reflection/refraction studies also suggested the presence of such an eastward dipping boundary (Ando et al., 1984; Hughes & Luetgert, 1991). It should be noted that postglacial rebound certainly contributed to the long-wavelength Moho variation. However, the magnitude would be on the order of hundreds of meters, rather than kilometers (Sella et al., 2007), and the magnitude would be expected to increase from south to north, opposite from the observed Moho step in New England.

The northward divergence of the Moho step from the Appalachian front and the decrease in the magnitude of the step roughly correspond with the widening of the Appalachian orogeny in northern New England. The narrowness of the orogeny in southern New England, at least to some degree, probably reflects differences in the style and intensity of the overprinting Acadian, post-Acadian, and Alleghenian tectonism in the south relative to the north (Figures 2.6 and A.10). If the Moho step does correspond with the eastern margin of Laurentian crust, it seems likely that the steepness and magnitude of the step in the south may reflect the cumulative effects of subsequent tectonic events. That is, the boundary may have been repeatedly reactivated (and steepened?) during subsequent collisional pulses as has been interpreted in surface geology (Cheney & Brady, 1992; Stanley & Ratcliff, 1985).

The boundary in the south may have been further complicated by strike-slip motion during Acadian and post-Acadian tectonism and possibly by differential exhumation and crustal thinning during Mesozoic extension (Thomas, 2006). The lateral offset between the Moho step and the Appalachian front in the north may be a more accurate reflection of the original character of the accretionary boundary. The offset in northern Maine would suggest a dip of approximately 20° to the east, consistent with the hypothesis of an eastward dipping Laurentian margin (van Staal & Barr, 2012).

The lack of a distinct Moho variation between the Avalon and Gander terranes may suggest a similar crustal (and lithospheric) composition between Avalon and Gander than between Grenville basement and accreted terranes (Musacchio et al., 1997; Wintsch et al., 2003). As suggested by many previous studies (e.g., Fischer, 2002; Musacchio et al., 1997; Williams et al., 2014), the crust beneath the Grenville Province may be made denser by composition changes after formation of the continental lithosphere. Alternatively, the Avalon-Gander boundary may have a complex geometry (for example, see Wintsch et al., 2014) that did not (in combination with younger events) result in Moho depth variation. The locally deepened Moho in northernmost Rhode Island may be associated with the boundary, but this cannot be rigorously evaluated at this time due to lack of dense onshore and offshore geophysical data coverage. Other possible candidates for this local Moho deepening would include subsequent partial melting or magmatic underplating related to Mesozoic rifting, which might be supported by the extensive exposure of volcanic rocks in northwestern Rhode Island (Maria & Hermes, 2001).

538 There are several possible interpretations for the sub-rectangular Moho depression in
539 northern New Hampshire and western Maine. One possibility is that the anomaly may
540 represent the eastward dipping Grenville/Laurentian margin that is offset approximately
541 200 km east of the margin to the north or south. The offset would be controlled by early
542 Cambrian transform faults associated with the late Proterozoic rifted margin of Rodinia
543 (Allen et al., 2009; McHone & Butler, 1984; Thomas, 2006). The presence of a Grenvillian
544 geochemical signature in White Mountain plutons of northern New Hampshire might
545 support this hypothesis (Dorais & Paige, 2000). Alternatively, the local Moho may have
546 been modified by younger events, such as magmatic underplating or partial melting in the
547 lower crust during Paleozoic accretion or even Mesozoic rifting (Hughes & Luetgert, 1991;
548 Kuiper, 2016). Local magmatism has been suggested considering the extensive exposure
549 of the White Mountain magma series in northern New Hampshire and southern Maine
550 (Dorais & Paige, 2000).
551
552 The origin of crustal thickness variation and Moho steps under New England also has
553 implications for the mantle lithosphere. If the Moho step in southern New England does
554 correspond with the eastern edge of Laurentian crust, then the steep angle of the boundary
555 makes it unlikely that southern New England is underlain by Laurentian mantle lithosphere.
556 Instead, the various terranes may have arrived with their own exotic mantle lithosphere. If
557 so, the modern lithosphere may be quite heterogeneous. Variations of lithospheric
558 thickness and seismic characteristics have been interpreted across the major tectonic
559 boundaries (e.g., Menke et al., 2016). Alternatively, the crustal fragments may have arrived
560 without stable lithosphere, or the lithosphere may have been removed (delaminated) during

561 the accretion process (e.g., Levin et al., 2000). If so, it is possible that the current
562 lithosphere grew after accretion of the peri-Gondwanan terranes. Such a lithosphere would
563 be distinct from that under Laurentia but similar across the accreted terranes.

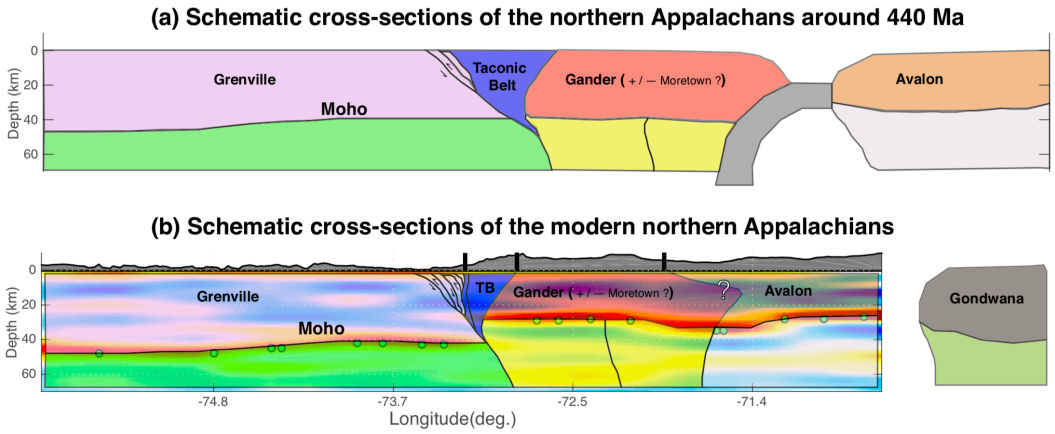

564

565 ***Figure 2.6. Schematic diagrams illustrating variations of the Moho depth due to***
566 ***Appalachian collisional events along cross section CC' (Figures 2.4 and 2.5), modified***
567 ***after Karabinos et al. (2017). Accretion of Avalon to the Gander terrane (i.e., the Acadian***
568 ***orogeny) is interpreted to have further shortened the Gander and Taconic crust in***
569 ***southern New England. The crustal shortening may have resulted in a nearly vertical or***
570 ***steeply dipping Grenville-Taconic boundary and a narrow surface expression of the***
571 ***Taconic belt in southern New England.***

572

573 **2.5. Summery**

574 Teleseismic P-wave RF analysis in the northern Appalachian region has revealed
575 significant Moho depth variations, which are well correlated with the distribution of
576 Bouguer gravity anomalies. We observed a complex Moho depth distribution pattern, both
577 across and along the orogenic strike. In southern New England, a sharp Moho step occurs
578 near the interpreted surface boundary between the Laurentian crust and the accreted

terranes. This may indicate a nearly vertical or steeply dipping Laurentian boundary within the crust, probably reflecting the cumulative effects of Paleozoic accretion and crustal shortening events. In contrast, the Moho variation is more gradual in northern New England, in correspondence with the widening of the Appalachian orogen. The lateral offset between the Moho step and the Appalachian front in the north may indicate a generally eastward dipping Laurentian basement. More geophysical and geologic constraints are required to further test our proposed hypotheses.

CHAPTER 3

Seismic characteristics of the eastern North American crust with Ps converted waves: Terrane accretion and modification of continental crust (*Li, C., Gao, H., & Williams, M. L. (2020). Seismic characteristics of the eastern North American crust with Ps converted waves: Terrane accretion and modification of continental crust. Journal of Geophysical Research: Solid Earth, 125, 5. doi:10.1029/2019JB018727***)**

3.1. Introduction

The Wilson tectonic cycle is one of the most fundamental concepts in the plate tectonic paradigm, central in most models for the growth and modification of continental crust on Earth. However, questions remain concerning the impact of past tectonic events on the composition and growth history of continental crust and mantle lithosphere. Simple but first-order questions include the following: Which geologically defined tectonic boundaries can be correlated with subsurface gradients or boundaries in three-dimensional seismic models, and what constraints can seismic data place on the timing and history of these boundaries? Eastern North America experienced at least two complete Wilson cycles over the last 1.3 Ga from assembly of the supercontinent Rodinia to the formation of the modern Atlantic Ocean (Figure 3.1a; e.g., Hatcher, 2010; Thomas, 2006). Thus, eastern North America provides an excellent tectonic setting to advance our understanding of continental accretion and lithospheric evolution through geologic time as well as the interpretation of deep crustal geophysical data in general.

The deployment of the EarthScope Transportable Array (IRIS Transportable Array, 2003) and its retaining subset (UC San Diego, 2013), together with many other seismic networks,

has significantly increased the spatial density of broadband observations in eastern North America and, thus, provide a new opportunity to constrain crustal thickness variations and the extent of crustal discontinuities at a resolution on the order of tens of kilometers. In this contribution, we report new receiver function (RF) results, which highlight variations in crustal characteristics within the major tectonic units and across the major tectonic boundaries. Comparison of our receiver function results with gravity data and geological observations allows us to explore the linkage of major geologically defined tectonic units with the geometry of seismically defined crustal discontinuities, and ultimately to investigate the formation and modification of the crust from the North American craton through the Grenville Province eastward to the Appalachian accreted region.

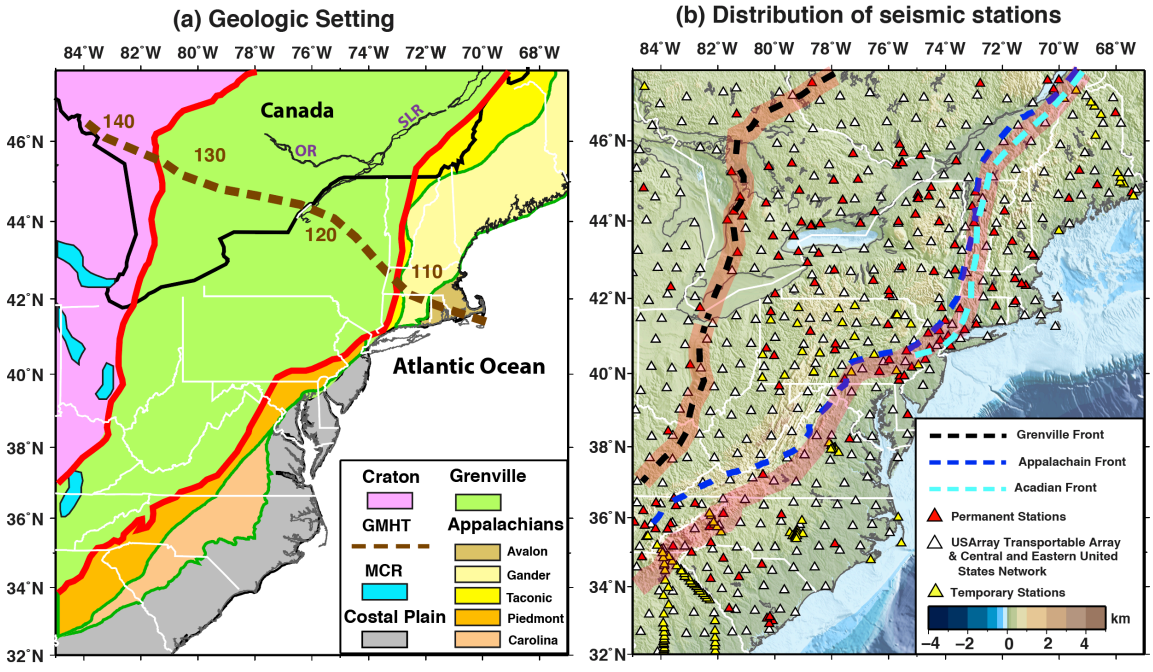

Figure 3.1. (a) Geological map showing the major tectonic units in eastern North America, modified after the lithotectonic map of the Appalachian orogen by Hibbard et al. (2006) and the United States Geological Survey basement domain map (http://mrdata.usgs.gov/ds-898/). The two thick red lines mark the inferred North

American craton-Grenville boundary and the Grenville-Appalachian boundary. The dark green lines mark the boundaries between the tectonic subprovinces of Inner Piedmont-Carolina-coastal plain in the southern Appalachian region and Taconic Belt-Gander-Avalon in the northern Appalachian region. The cyan patches denote the inferred eastern arm of the Midcontinent Rift (MCR). The brown dashed line indicates the proposed Great Meteor hot spot track (GMHT), marked with time in Ma. (b) Distribution of the broadband seismic stations used in the calculation of receiver functions. The red triangles represent the permanent stations, the white triangles for the EarthScope U.S. Transportable Array and the central and eastern United States network, and the yellow triangles for the flexible arrays. The black, blue, and cyan dashed lines mark the Grenville deformation front, the Appalachian deformation front, and the Acadian deformation front, respectively. The red shadow zones mark the inferred major tectonic boundaries as shown by the red lines in (a). The background color is the bathemetry/topography.

Previous studies have demonstrated that the continental crust beneath eastern North America varies within and across the major tectonic units in terms of age, thickness, and seismic velocity. For example, geochronology and lead isotope studies showed that the Grenville-aged crust is on average younger in the United States than in Canada (e.g., Hynes & Rivers, 2010; Loewy et al., 2003). The U.S. Grenville Province is characterized by a thicker crust and is seismically faster above and beneath the Moho in comparison with the Appalachians and the Canadian Grenville Province (e.g., Schmandt et al., 2015; Shen & Ritzwoller, 2016). Receiver function analysis has revealed a low-angle southeastward

dipping intra-crustal feature across the central Grenville Province (Long et al., 2019) and beneath the southern Appalachians in Georgia and South Carolina (Hopper et al., 2017; Parker et al., 2015). In contrast, no such intra-crustal layer was seen in the Appalachian region of New England (Li et al., 2018). Moho depth changes gradually beneath northern New England (Li et al., 2018) and the southern Appalachian orogen in Georgia (Hopper et al., 2017; Parker et al., 2015). In contrast, a sharp Moho step was imaged in southern New England, New Jersey, and northern Virginia (Li et al., 2018; Soto-Cordero et al., 2018). Although significant variations in crustal features were detected, none of those previous studies provide systematic constraints on the crustal structure for the entire eastern North American region.

3.2. Data and methodology

3.2.1. Data

We collected data from a total of 659 broadband seismic stations, including 167 stations from 12 long-running seismic networks (CN, Geological Survey of Canada, 1989; CO, Colorado Geological Survey, 2016; ET, University of Memphis, CERI, 1982; IM; IU, Albuquerque Seismological Laboratory /USGS, 1988; KY, Kentucky Geological Survey/University of Kentucky, 1982; LD, Lamont Doherty Earth Observatory, Columbia University, 1970; N4, UC San Diego, 2013; NE, Albuquerque Seismological Laboratory /USGS, 1994; PE, Penn State University, 2004; PO, Geological Survey of Canada, 2000; WU, University of Western Ontario, 1991), 380 stations from the EarthScope Transportable Array (IRIS Transportable Array, 2003), and 112 temporary stations from 7 dense arrays (X8, Menke et al., 2012; XQ, Wagner, 2012; XY; Penn State University, 2013; YC, Meltzer, 2011; YO, Gaherty et al., 2014; Z4, Wagner, 2009; Z9, Fischer et al.,

2010; Figure 3.1b; see a detailed network description in the supporting information). The well-distributed coverage of the stations across our study region makes it feasible to study the high-resolution variations in crustal thickness beneath eastern North America. Three-component seismograms were requested from the Data Management center of the Incorporated Research Institutions for Seismology (IRIS) for 4,079 earthquakes that occurred between 2010 and 2017. The earthquakes were requested to have an epicentral distance of 30-95° to each seismic station and the body wave magnitude equal to or greater than 5.5. Figure 3.2 shows the distribution of selected earthquakes, which result in a total of 306,942 waveforms obtained for the RF calculations.

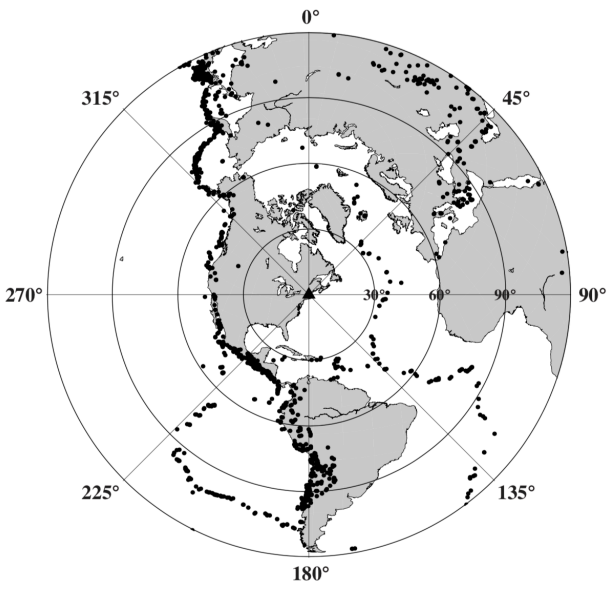

Figure 3.2. Locations of Events from 2010 to 2017 used for the calculation of receiver functions. The black triangle marks the center of the research region.

3.2.2. P-Wave receiver functions

Prior to the calculation of receiver functions, we cut the raw seismograms to 90-s segments, that is, 30 s before and 60 s after the direct P-wave arrival calculated using the one-dimensional velocity model IASP91 (Kennett & Engdahl, 1991). We removed the mean value and the first-order linear trend from the waveforms. The horizontal components were then rotated along the free surface to obtain the radial and transverse components. We calculated teleseismic P-wave RFs using the generalized iterative deconvolution method (Wang & Pavlis, 2016). This method significantly improved the resolution of RFs by applying an inverse wavelet on the time-domain iterative deconvolution, which can be described in three steps.

First, an inverse wavelet of the source is calculated in the frequency domain as

$$S(\omega) = \frac{Z^*(\omega)}{Z(\omega)Z^*(\omega)+\mu} \quad (1)$$

where $Z(\omega)$ and $Z^*(\omega)$ represent the Fourier transforms of the vertical-component seismogram and its complex conjugate, respectively. μ is the background noise level, defined as the standard deviation of the waveforms within a time window of 1-11s prior to the direct P arrival. Second, we cross-correlate the inverse wavelet with the radial-component seismogram in the time domain. The arrival time and amplitude of the peak spike in cross-correlation is then used to define a spike sequence. Third, the residual between the radial-component waveform and the spike sequence is used to replace the original radial-component waveform. Steps two and three are iteratively repeated until the residual reaches a minimum value of 0.01 and the final spike sequence is the calculated

716 radial-component RF. We then applied a low-pass Gaussian filter of 2.4 Hz on the
717 calculated RFs.
718
719 In order to identify plausible phases converted from the Moho (P_ms) and other primary
720 intra-crustal interfaces, we implemented multiple steps to control the quality of the radial-
721 component RFs. The rule of thumb is that the P_ms phase is anticipated as a first-order
722 positive phase, which was taken as our target phase during selection. We first applied a
723 time moveout correction, with an average slowness of 0.058 s/km based on the IASP91
724 model (Park & Levin, 2016), to remove the impact of incident angle on the P_ms phase.
725 After time moveout, we visually inspected all observed RFs and manually selected those
726 with a clear positive phase within a time window of 2-8 s. For each station, we then visually
727 reviewed the selected RFs and insured the consistency of the P_ms phase within similar back-
728 azimuthal directions. Furthermore, the selected RFs were filtered within multiple
729 frequency bands, ranging from 0.05-0.75 Hz and 0.1-1.2 Hz to 0.2-2.0 Hz, to check the
730 stability of the P_ms phase.
731
732 Previous studies by Ammon (1991) and Cassidy (1992) showed that the amplitude ratio of
733 the radial- and vertical-component RFs preserves information on the velocity contrast
734 across sharp boundaries. Therefore, we normalized the radial-component RFs in terms of
735 the maximum amplitude of the corresponding vertical-component RFs. After
736 normalization, we stacked the RFs from all the back-azimuthal directions to represent the
737 average RF feature beneath each station. Stacking highlights the primary phases and
738 increases the signal-to-noise ratio. The time of the maximum positive peak of the stacked

739 RF within a time window of 2-8 s was then automatically picked as the mean P_ms arrival
740 time, with the uncertainty calculated as the standard error of the P_ms arrival times of all
741 individual events at each station (Figure 3.3).
742
743 Here we chose three stations, TA.E54A, TA.S51A, and PE.PSDB (see the station locations
744 in Figure 3.4), to illustrate the RF quality within our study region (Figure 3.3). The two
745 EarthScope Transportable Array stations E54A and S51A have two-year seismic
746 recordings from 2012 to 2014, and the Penn state network station PSDB has been operating
747 since 2010. We took the average of the RF events coming from the same back-azimuthal
748 direction (within 1^o) at each station. As demonstrated in Figure 3.3, a clear P_ms conversion
749 is identified within a time window of 4.5-6.2 s after the direct P arrival at all these three
750 stations. The P_ms arrival time also shows a certain degree of back-azimuthal dependence,
751 which could be related to a dipping Moho or a combination of dipping and anisotropy
752 (Levin & Park, 1997). A further study combining both radial- and transverse-component
753 RFs may help identify possible sources for the directional dependence, but this falls beyond
754 the scope of this study. In addition to the primary P_ms conversions at the Moho, strong and
755 consistent signals are observed within the crust at many seismic stations (Figures 3.3, B.13,
756 B.14, and B.15). For example, station PE.PSDB reveals two positive phases at ~0.5 s and
757 ~2.1 s, respectively, and a strong negative phase within a time window of 2.9-3.5 s (Figure
758 3.3b). Station TA.S51A demonstrates a clear positive signal at approximately 1.6 s from
759 all the back-azimuthal directions (Figure 3.3c).

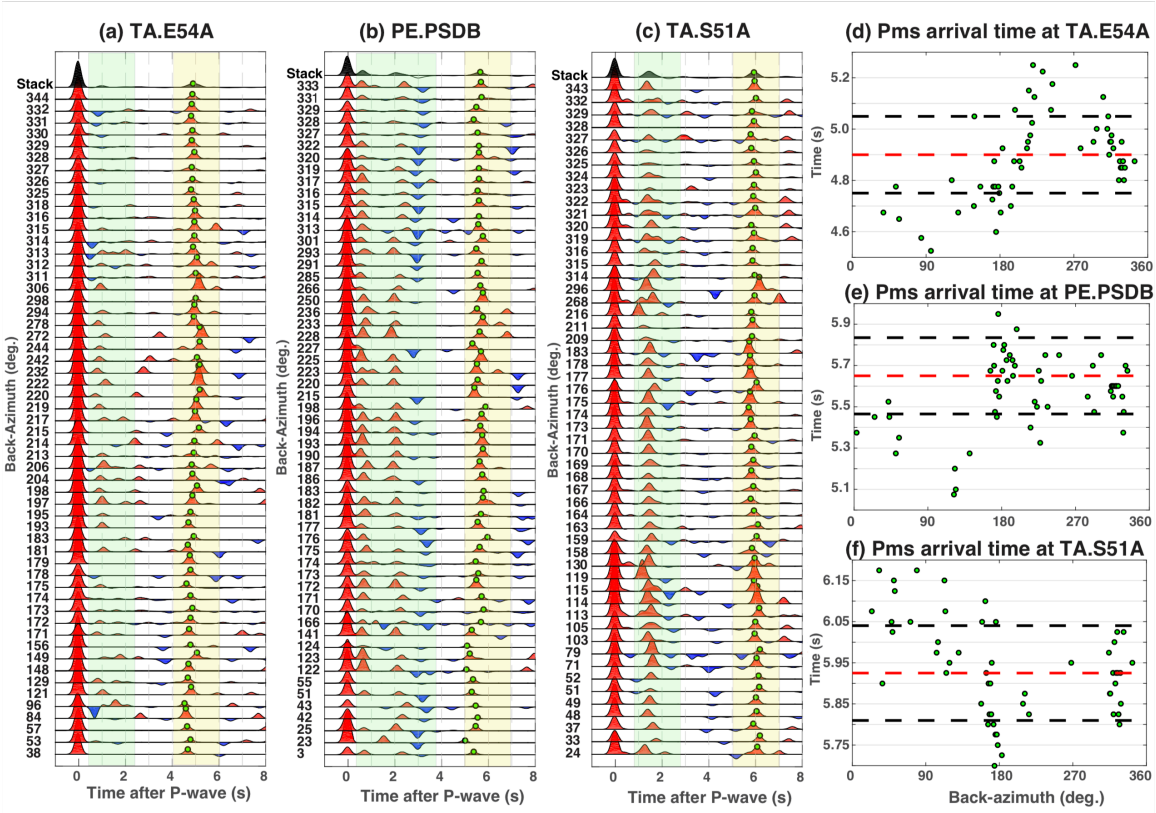

Figure 3.3. (a-c) Examples of normalized radial-component receiver functions (RF) for stations TA.E54A, PE.PSDB, and TA.S51A, sorted by back azimuths. See station locations in Figure 3.4. A positive phase (filled with red color) corresponds to a sharp velocity increase with depth, while a negative phase (filled with blue color) correlates with a velocity decrease. The top trace is the stacked receiver function from all the back azimuth directions at each station. The waveforms are low-pass filtered at 2.4 Hz. The green dots mark the automatically picked P_ms arrivals. The shaded yellow window highlights the variation pattern of the P_ms phase in terms of the back azimuth, and the shaded green window highlights the phases converted from the intracrustal layers. (d-f) Distribution of automatically picked P_ms arrival time (green dots) in terms of the back azimuth for the three stations in (a)-(c). The red and black dashed lines correspond to

772 ***the P_ms arrival time of the stacked radial-component receiver functions and the***
773 ***corresponding uncertainty.***
774
775 The number of selected RF events varies within a broad range among the seismic stations,
776 depending on the operating duration and station location. Most long-running stations
777 recorded high-quality RFs with the event numbers ranging from 40 up to 336 (Figure B.1;
778 Table B.1). A few stations, such as PE.PASH and PO.BELQ, have less than one-year
779 recording periods, which leads to fewer events. The number of RFs for the temporary
780 stations varies within a range of 13-100 (Figure B.1; Table B.1). We found that 77 stations
781 show strong crustal reverberations (see station locations in Figure B.2 and RF examples in
782 Figure B.3), most of which are located within the Atlantic coastal plain. In contrast, we
783 saw clear P_ms phases for stations located within the Appalachian basin where thick
784 sediments exist (e.g., Laske et al., 2013), even though multiple positive and negative phases
785 are observed prior to the P_ms arrivals (Figure 3.3b and Figure B.14). The different features
786 of RFs observed between stations located within the Appalachian basin and the coastal
787 basin may reflect the different velocity contrasts at the sediment-bedrock interface (Figure
788 B.10). The nature of the crustal reverberations in RFs deserves a careful analysis and will
789 be a subject of a follow-up study. In this study, we excluded the stations that have strong
790 reverberations from further analysis considering that the reverberations can interfere with
791 and mask major phases in RFs. In total, we selected 39,237 RFs for 487 broadband stations
792 (~73% of the initially collected stations) to be used for further analysis.
793

3.2.3. Migration

We converted the normalized radial-component RFs from all the back-azimuthal directions at all the selected stations from the time domain to the depth domain, using the common conversion point (CCP) stacking method (Hansen & Dueker, 2009). Assuming a flat-layer model, the arrival time of the converted Ps phase at a given depth of z is described as

$$T_{Ps}(z) = \int_z^0 [\sqrt{Vs(z)^{-2} - P^2} - \sqrt{Vp(z)^{-2} - P^2}]\, dz \quad (2)$$

In this equation, P is the ray parameter, and Vp and Vs are the P- and S-wave velocities, respectively. Considering the distribution density of seismic stations, we meshed our study area with a horizontal bin size of 20 km and a vertical interval dz of 1 km from the surface down to 150 km depth. We interpolated the three-dimensional shear-wave velocity model of the United States by Shen and Ritzwoller (2016) to obtain the seismic velocities beneath each grid point assuming a constant Vp/Vs ratio of 1.78.

The amplitudes of the individual RFs were then back-projected within each bin. In order to estimate the Moho depth beneath each surface grid point, we take the lateral resolution of the Fresnel zone into consideration, which is depth dependent. Here we used the Fresnel zone formula developed by Pavlis (2011) to estimate the aperture size (that is, the lateral resolution) at each depth interval (Figure B.4). For example, the radii of the aperture of the CCP stacking are about 10 and 16 km at depths of 20 and 40 km, respectively (Figures B.4 and B.5). Correspondingly, the RF amplitude at each bin is defined as the averaged amplitude of back-projected RFs within the depth-dependent aperture radius. We then automatically picked the depth of the maximum amplitude of the averaged RFs within a depth range of 20-70 km as the Moho depth. In addition, the CCP stacking also

817 demonstrates strong negative phases at 5-28 km depths within the central Grenville crust.
818 The depth of the maximum amplitude of these negative phases was also automatically
819 picked for further analysis. See the Supporting Information for the uncertainty estimate of
820 the Moho depth.
821
822 **3.3. Results**
823 We investigated the distribution of average arrival times of primary converted phases from
824 the Moho and within the crust, as well as the corresponding depth variations. We observe
825 distinct variations in P_ms arrival times and Moho depth in eastern North America (Figures
826 3.4 and 3.5b) on multiple scales. The high resolution of the Moho data set benefits from
827 the combination of a large number of broadband stations that were active over the last
828 decade. In general, the Grenville Province and the North American craton are characterized
829 by larger P_ms arrivals and a thicker crust. The Appalachian regions that are interpreted to
830 be underlain by accreted (exotic) terranes show relatively smaller P_ms arrival times (i.e.
831 thinner crust). Local variations in Moho depth are delineated clearly, such as a shallow
832 Moho of ~30-35 km in northeastern Pennsylvania, near the Ottawa River and the St.
833 Lawrence River Plain (a1, a2, and a3 in Figure 3.5). In addition, we also image a distinct
834 intra-crustal feature within the central Grenville Province (Figure 3.6), which we discuss
835 in section 3.4.3. In order to demonstrate these seismic features, we present five CCP
836 stacking profiles that are nearly perpendicular to the orogenic strike (see profile locations
837 in Figures 3.4 and cross sections in Figure 3.7).

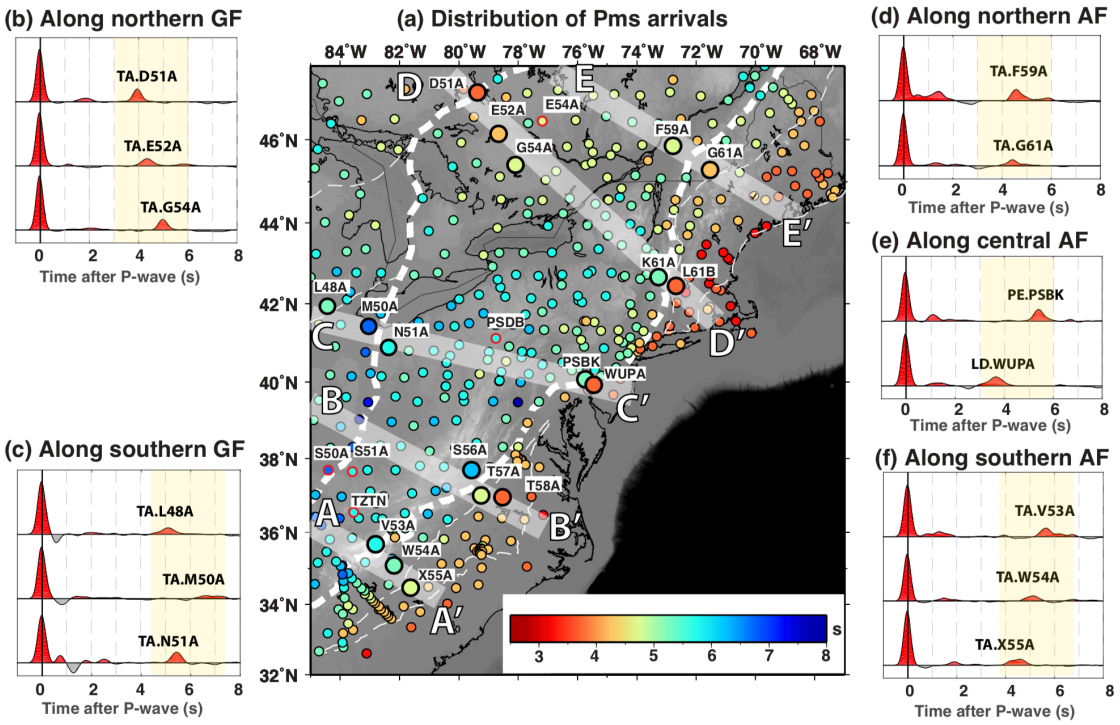

Figure 3.4. (a) Distribution of P_ms arrival time (in seconds), automatically picked from the stacked radial-component receiver functions for each seismic station. Warm colors denote relatively smaller P_ms arrivals, and cold colors for larger P_ms arrivals. The five shaded zones are the profile locations shown in Figure 3.7. The larger dots mark the locations of selected seismic stations in (b)-(f), which are also shown as green dots in Figure 3.7. The dots with red outline are stations shown in Figures 3.3 and B.15. (b)-(f) Representative radial-component RFs to demonstrate variations of P_ms arrival times in eastern North America. For each station, the RFs are stacked from all the back-azimuthal directions. The waveforms are low-pass filtered at 2.4 Hz. The shaded yellow window highlights the difference in the P_ms arrival times.

3.3.1. Crustal thickness variation in the Grenville Province

The Grenville-aged crust in eastern North America is characterized by a large variation in P_ms arrival time (~4.0-7.0 s) and the associated thickness (~32-65 km). A first-order characteristic is the distinct difference in P_ms arrival time (Moho depth) from south to north within the Grenville Province and along the Grenville Front (Figures 3.4 and 3.5). The U.S. Grenville Province is characterized by large P_ms arrival times (~5.2-7.0 s) and a deep Moho (~47-65 km), extending from Tennessee and Georgia to the national border (Figure 3.5b). In contrast, the Canadian Grenville Province has P_ms arrival times of ~4.0-5.4 s (crustal thickness ~32-50 km).

There is also a significant difference in the P_ms arrivals (Moho depth) along and across the Grenville Front. Six seismic stations along the southern Grenville Front show much larger P_ms arrivals than the surrounding stations, resulting in a locally deepened Moho (~55-65 km) within a narrow zone from northern Ohio to eastern Kentucky (Figures 3.4a and 3.5b and cross-sections AA', BB', and CC' in Figure 3.7). For example, a ~7.0 s P_ms arrival time (~63 km Moho depth) is seen at station TA.M50A (Figure 3.4c). In comparison, a relatively smaller P_ms arrival of ~5-5.5 s (~46-50 km Moho depth) is imaged at nearby stations TA.L48A and TA.N51A (Figure 3.4c). Near the northernmost Grenville Front, the small P_ms arrivals of ~4-4.5 s and a corresponding shallow Moho of ~32-35 km are detected (see examples in Figure 3.4b). Note that we do not have resolution in the southernmost and northernmost ends of the Grenville Front near the boundaries of our study area. However, previous studies that investigated the North American craton to west of our study region also show a shallow Moho depth along the northern Grenville Front and support a locally

deepened Moho along the southern Grenville Front (Darbyshire et al., 2017; Levin et al., 2017; Petrescu et al., 2016; Yang et al., 2017).

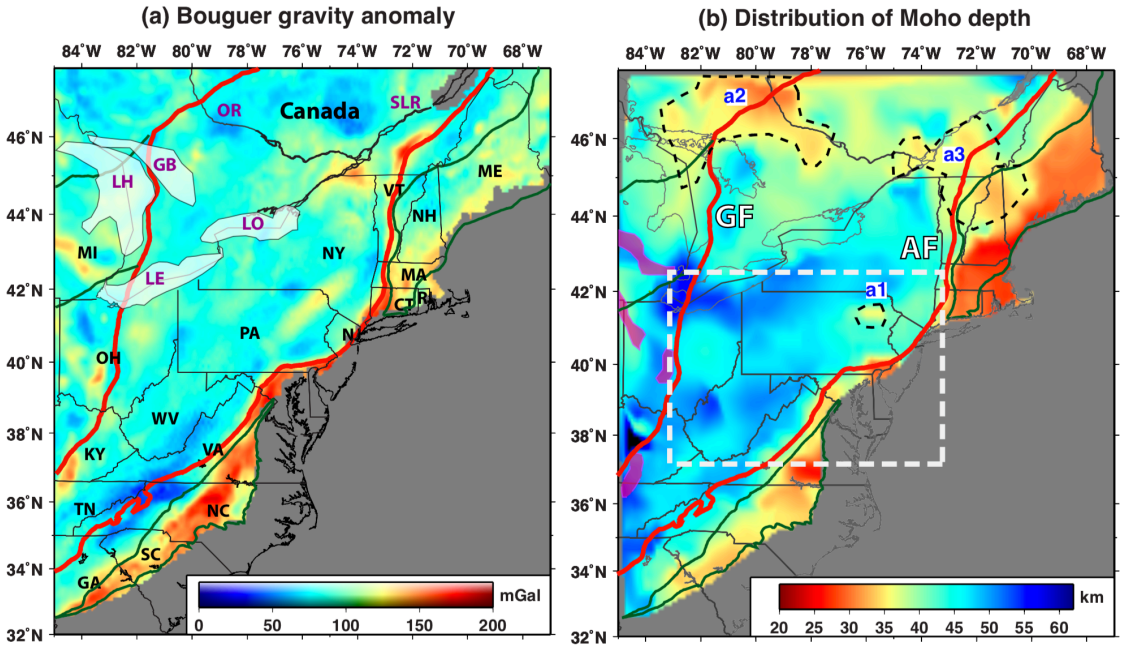

Figure 3.5. (a) Distribution of Bouguer gravity anomalies from Bonvalot et al. (2012). The red and dark green lines mark the tectonic boundaries as in Figure 3.1a. (b) Distribution of the Moho depth (in kilometers) extracted from the common conversion point stacking. GF = the Grenville Front; AF = the Appalachian Front; LO = Lake Ontario; LE = Lake Erie; LH = Lake Huron; GB = Georgian Bay; OR = the Ottawa River; SLR = the St. Lawrence River. The white dashed line marks the map region in Figure 3.6 where we observe an inner-crustal layer. The red solid lines mark the Grenville Front and the Appalachian Front. The black dashed lines mark the small-scale anomalies observed in the Moho depth map.

3.3.2. Moho depth variation in the Appalachian orogen

887 The Moho depth shows a systematic variation within the Appalachian orogen, ranging from
888 25 km to 45 km. Within the southern Appalachian region, the Moho depth decreases
889 southeastward from ~45 km to ~35 km, a 10 km decrease of the Moho depth. Within the
890 northern Appalachian region, the observed Moho depth is ~35-40 km near the Appalachian
891 orogenic Front and decreases southeastward to ~25-30 km toward the coastal plain (Figure
892 3.5b).
893
894 We observe a significant west-to-east decrease in the Moho depth across the Appalachian
895 orogen. The steepness of the gradient in Moho depth, however, varies significantly along
896 strike (Figures 3.4a and 3.5b). A clear and sharp Moho offset of up to 12-15 km is observed
897 within a narrow zone extending from southern New England through New Jersey to
898 Virginia (Figures 3.4a and 3.5b). For example, the P_ms arrival time (Moho depth) decreases
899 from ~5.4 s (~40 km) to ~3.8 s (~27 km) between stations PE.PSBK and LD.WUPA in
900 New Jersey (Figure 3.4e and cross-section CC' in Figure 3.7). Similarly, between stations
901 TA.K61A and TA. L61B in southern New England, the P_ms arrival time decreases from
902 5.2 s to 3.7 s (the corresponding Moho depth changes from ~45 km to ~30 km) (see Cross-
903 section DD' in Figure 3.7 and Figures B.12a and B.13), over a horizontal distance of ~70
904 km. Although the actual magnitude of the Moho offset may differ slightly due to the
905 uncertainty of ~6 km in the Moho depth estimation, the uncertainty is much less than the
906 observed Moho offset in our study (see the detailed uncertainty analysis in the Supporting
907 Information).
908

In contrast, the Moho depth decreases subtly across the Appalachian orogen in northern New England, southernmost Virginia, western North Carolina, and Georgia. Overall, we image a gradual Moho depth variation across and within the widened northern (north of latitude 45.5°N) and southern (south of latitude 37°N) Appalachian regions. We choose RF results from eight stations (Figures 3.4d, B.12b, and 3.4f) along cross-sections AA', BB', and EE' to illustrate the observations. For example, from station TA.V53A to TA.W54A to TA.X55A, we observe a decrease of the P_ms arrival time by ~0.7 s across the Grenville-Appalachian boundary and by ~0.5 s across the Piedmont-Carolina boundary (Figure 3.4f). The corresponding the Moho depth gradually decreases from 50 km to 42 km to 35 km over a horizontal distance of 190 km (Cross-section AA' in Figure 3.7). Similarly, a gradual change of P_ms arrival and Moho depth is seen from TA.F59A to TA.G61A over ~130 km in the northern Appalachian region (Figure 3.4d and cross-section EE' in Figure 3.7).

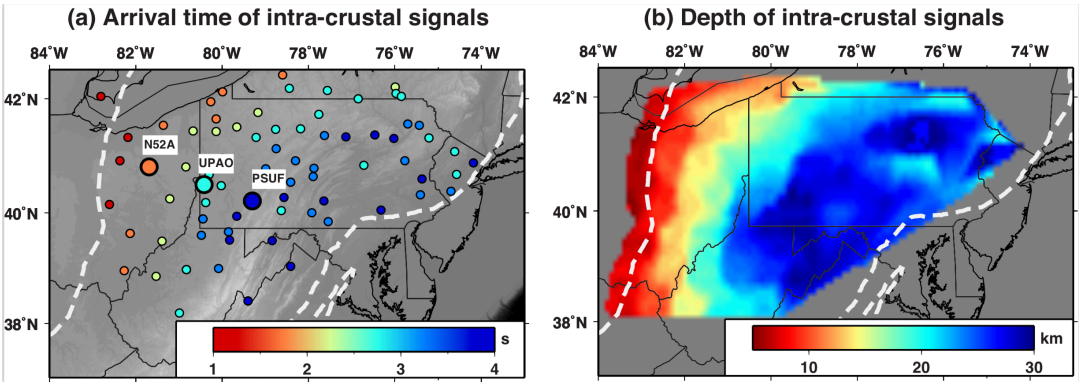

Figure 3.6. (a) Arrival time distribution of the intra-crustal negative phases (in seconds). The three large dots mark the locations of the representative stations in Figure B.14. (b) Distribution of the corresponding depth of the intra-crustal negative phase, extracted from the common conversion point stacking method.

3.3.3. An eastward dipping feature within the U.S. Grenville crust

Seismic stations located in the central (from north to south) Grenville Province exhibit a pronounced negative phase within the crust. The phase arrival time gradually increases from the Grenville Front to the east over a horizontal distance of ~700 km, showing an eastward-dipping intra-crustal feature (Figure 3.6). As demonstrated in Figure B.14, the arrival time of the negative phase gradually increases from station TA.N52A (~1.8 s) to PE.UPAO (~3.0 s) and PE.PSUF (~ 3.8 s), with the corresponding depths of approximately 10 km, 20 km, and 25 km, respectively (Cross-section CC' in Figure 3.7). Most of the stations that show the negative phase are located in southernmost New York, Pennsylvania, eastern Ohio, and West Virginia (Figure 3.6). In Kentucky, Tennessee, and Georgia, we are only able to identify a negative phase signal at a few stations (see examples in Figure B.15), leading to a less consistent intra-crustal layer in our CCP imaging (Cross-sections AA' and BB' in Figure 3.7). In total, 107 stations, extending from latitude 34°N to 42.5°N, recorded the negative phase signals. Additionally, we see multiple positive phases prior to the negative phase at many stations (see profiles BB' and CC' in Figure 3.7), which may represent second-order velocity discontinuities within the crust. More specifically, the near-surface positive phase may result from a sedimentary basement (Figure B.10), and the later positive and negative phases may represent a high velocity layer or a shear zone with strong seismic anisotropy (Figure B.11). However, the nature of these phases, as well as possible interpretations, need to be furthered explored by incorporating data from dense seismic arrays and analyzing the transverse-component receiver functions.

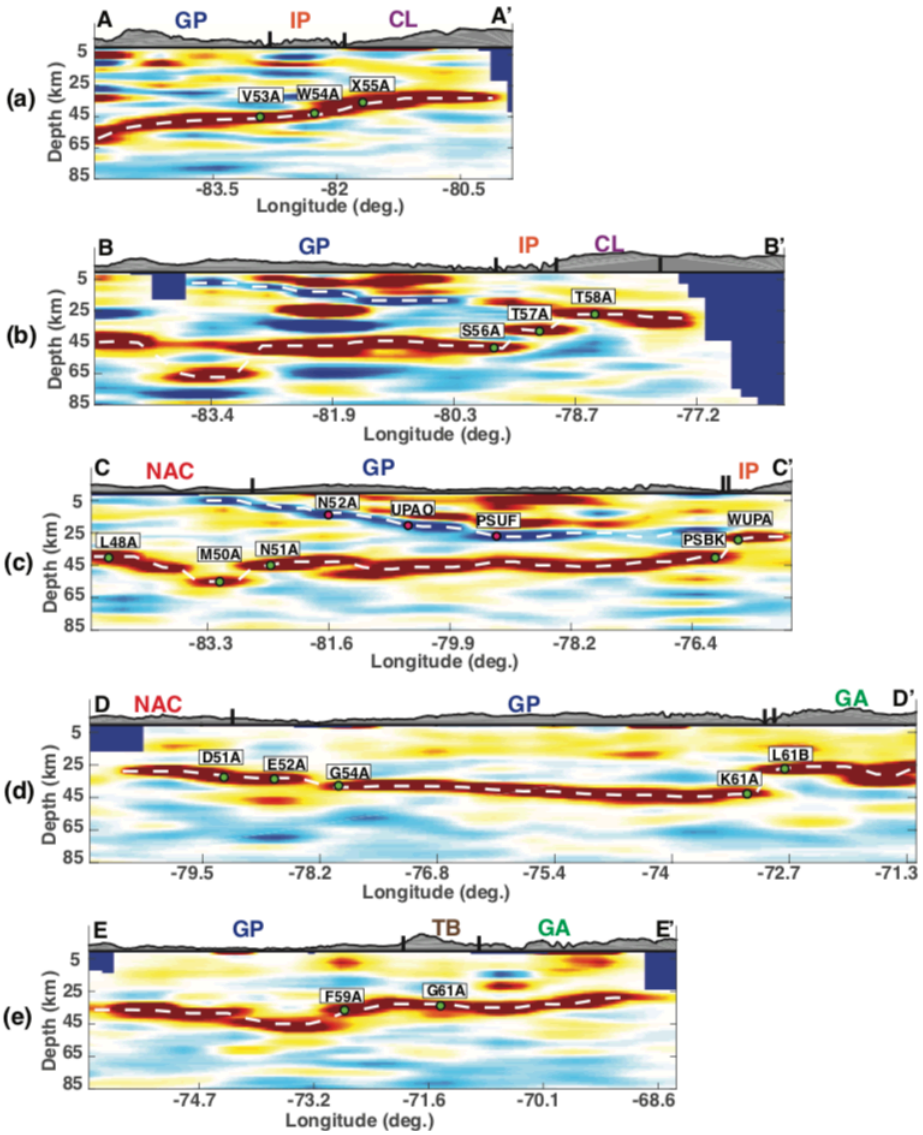

950

951 ***Figure 3.7. NW-SE cross-sections of the common conversion point stacking. See the***
952 ***profile locations in Figures 3.4. The major tectonic boundaries are marked by solid black***
953 ***lines above each profile. The white dashed line represents the interpreted Moho and***
954 ***intra-crustal-layer, which are extracted from the common conversion point stacking.***
955 ***The colored dots in the cross-section mark the preferred Moho and intra-crustal layer***
956 ***beneath seismic stations, as described in the text. IP = Inner Piedmont; CL = Carolina;***
957 ***GA= Gander; GP = Grenville Province; NAC = North American craton.***

958

3.4. Discussion

Our RF results demonstrate a distinct variation in Moho depth both within and across the major tectonic units in eastern North America (Figures 3.5b and B.14). (1) We observe a relatively thick crust (47-65 km) in the United States portion of the Grenville Province and a thinner crust within the Canadian portion (33-50 km). (2) An abrupt Moho deepening (~65 km) can be seen within a narrow zone along the southern part of the geologically-defined Grenville Front (Latitude ~37^{o}N to 42.5^{o}N). In contrast, the Moho depth beneath the northernmost Grenville Front is much shallower than beneath the southern part. (3) A strong intra-crustal layer is imaged beneath the central Grenville Province, with a low-angle dip of approximately 6^{o} from the Grenville Front eastward to the Appalachian orogen (Figure 3.6; Cross-section CC' in Figure 3.7). (4) A sharp west-east Moho step (~12-15 km) is observed over a horizontal distance of ~70 km in the central segment of the Appalachian orogen (from Latitude 37^{o}N to 43.5^{o}N; cross-sections CC' and DD' in Figure 3.7). The Moho step tends to be more gradual across the Appalachian Front in the southern and northern segments of Appalachian orogen, where we observe a second-order Moho variation (cross-sections AA' and EE' in Figure 3.7). Interestingly, the location of the Moho step diverges from the Appalachian (or Acadian) Front in the northern and southern parts of the Appalachian orogeny, roughly correlated with the widening of the overall orogen (Figure 3.5b).

The crustal features beneath eastern North America resolved in this study are broadly consistent with the results of previous studies. We specifically compared the distribution patterns of the crustal thickness extracted from this study, Shen & Ritzwoller (2016), and

Schmandt et al. (2015) (Figure B.17). For example, the general northwestward decrease in crustal thickness from the Grenville Province to the Appalachian region can be seen in several seismological studies (e.g., Gaherty et al., 2011; Li et al., 2002; Li et al., 2018; Schmandt et al., 2015; Shen & Ritzwoller, 2016). The deep Moho beneath the Grenville Province in the United States was also previously recognized even though the horizontal distribution of deep Moho is slightly different between studies (e.g., Schmandt et al., 2015; Shen & Ritzwoller, 2016; Yang et al., 2017). The presence of an intra-crustal layer was noted along a 2-D seismic array in Ohio, West Virginia, Georgia, and South Carolina by both receiver function studies (Hopper et al., 2017; Long et al., 2019; Parker et al., 2015) and active source experiments (Culotta et al., 1990; White et al., 2000). Nevertheless, our results provide a comprehensive constraint on both Moho depth variations and the 3-D spatial distribution of the intra-crustal layer across the entire eastern North American region, benefiting from the data integration of all broadband stations deployed in this region over the last decade.

3.4.1. Comparison of crustal thickness, gravity, and topography

We compared the distribution patterns of crustal thickness, Bouguer gravity, and elevation in eastern North America (Figures 3.1b and 3.5). From isostasy theory, we would expect lower Bouguer gravity in the U.S. Grenville Province, where the crust is thicker than in the Canadian part (Figures 3.1b and 3.5). However, we do not observe any systematic variation in Bouguer gravity within the Grenville interior. The lack of correlation between crustal thickness and gravity may reflect a non-uniform density distribution in the crust and upper mantle. It was suggested that the lower crust of the continental lithosphere can be densified

and strengthened due to metamorphic reactions (e.g., Fischer, 2002; Williams et al., 2014), which might be expected in the thicker crust of the eastern United States (e.g., Schmandt et al. 2015). A denser lower crust could increase the gravity anomaly of the US relative to the Canadian portion of the Grenville Province. In addition, geophysical and petrologic studies (e.g., Mooney & Kaban, 2010; Perry et al.,2003) have suggested that the uppermost mantle is less dense and more buoyant in the northern Grenville than in the southern Grenville, which would also help to explain our observations. Some small-scale variations in the Moho depth show (anti-)correlation with Bouguer gravity. For example, the locally shallowed Moho in northeastern Pennsylvania roughly corresponds to a relatively large gravity anomaly (a1 in Figure 3.5b), suggesting a more local isostatic control of Moho depth.

The relationship among crustal thickness, Bouguer gravity, and elevation is also not straightforward within the Appalachian orogen. In the southern Appalachians, for example, we see the expected negative correlation pattern roughly across the Inner Piedmont-Carolina terrane boundary (Hales et al.,1968; James et al.,1968), where the crustal thickness and the elevation show an west-east decrease and a corresponding Bouguer gravity increase (Figures 3.1b and 3.5). However, we did not image a Moho depth anomaly beneath the highest southern Appalachian Mountains, where a distinct gravity low exists. The crustal thickness is anti-correlated with the Bouguer gravity along the Appalachian orogen from Latitude ~37^{o}N to ~43^{o}N, where the sharp west-east Moho step is observed. Within the northern Appalachians, the relatively thin crust in the coastal plain roughly corresponds with higher gravity, and a local downward deflection of the Moho is roughly

correlated with the low Bouguer gravity anomaly (a3 in Figure 3.5b). Comparing the northern and southern Appalachians, we observe that the interpreted accreted terranes (Gander and Avalon) in the New England region show a thinner crust with a lower gravity while the Carolina Superterrane has a relatively thicker crust with a larger gravity anomaly.

3.4.2. Crustal thickness variation within the Grenville Province

The observed differences in seismic characteristics within the interior of the Grenville Province, especially differences in crustal thickness and the presence of an intra-crustal layer, may indicate important differences in the tectonic history from north to south. The reconstruction study by Li et al. (2008) concluded that the U.S. Grenville Province represents a single continent block, which was accreted onto the North American craton at ~1.0 Ga. This simple collision mode might have thickened the crust along the southern Grenville Front. In this case, the intra-crustal dipping layer in the central Grenville interior could represent the trace of a west-vergent thrust/shear zone that emplaced Grenville-aged crust over the North American craton (Long et al., 2019). In contrast, the Canadian portion of the Grenville Province is interpreted to have formed by a sequence of island-arc and micro-continent accretions (e.g., McLelland et al., 2013; Rivers, 2015). Several active source experiments in Canada (e.g., Culotta et al., 1990; Martignole & Calvert, 1996; Rivers, 2015) demonstrated local-scale thrust belts within the northern Grenville crust, supporting the repeated accretion of smaller fragments model. The accretion may have resulted in a more complex network of crustal structures instead of forming a simple intra-crustal layer (structure) as observed in the south.

Another possible interpretation for the Grenville crustal variation is that the region may have had a similar prograde history, but experienced different degrees of modification during post-collisional collapse and exhumation. Numerical modeling studies by Jamieson et al. (2010) suggested that the northern Grenville experienced strong extensional collapse as the thermally weakened middle and lower crust could no longer support the thick upper crust. In this case, the collapse would eventually result in a thinner crust and might obscure any intra-crustal collisional feature in the Canadian Grenville Province. The large-scale erosion during the breakup of Rodinia at ~750 Ma might have further thinned the crust. In addition, recent tectonic events, such as the magmatism caused by the Great Meteor hotspot during ~140-110 Ma (Eaton & Frederiksen, 2007) and a failed rift near the Ottawa River (Rimando & Benn, 2005), also likely modified the Grenville-aged crust in Canada, contributing to the observed south-north differences.

It was recently suggested that the gravity-defined eastern arm of the 1.1-Ga failed Midcontinent Rift extends into Ohio and Kentucky along the southern Grenville Front (cyan patches in Figure 3.1a; Stein et al. 2018a, 2018b). However, we do not observe any obvious spatial correlation between the eastern arm of the Midcontinent Rift (pink patches in Figure 3.5b) and the locally deepened Moho imaged by our RF study (Figure 3.5b). It is likely that the crust was locally thickened during and shortly after the Midcontinent rifting due to underplating, sedimentation, and compression (Stein et al., 2018a). Compression during the later phases of the Grenville orogeny might have further thickened the crust along the southern Grenville Front, which consequently inverted and overprinted structures associated with the eastern arm of the Midcontinent Rift. After the main collisional pulses,

post-orogenic erosion would have removed the surface thrust belts along the southern Grenville Front, leaving the local Moho depression as a remnant continental root.

3.4.3. Moho depth variation within the Appalachian accretion

The rough correlation of Moho depth with geologically-defined terrane boundaries and with Bouguer gravity variation suggests that the large-scale crustal thickness changes in the Appalachian region are linked with the terrane accretion during the assembly of Pangea. Further, the magnitude and character (dipping or steep) of the Moho offset along the Appalachians may provide additional constraints on tectonic models. We propose that differences in the steepness of the Moho offset along the Appalachians reflect along-strike variations of the steepness of the subsurface boundary between Laurentian lithosphere and Gondwana-derived elements. Specifically, the gradual Moho depth change beneath the northern and southern Appalachian regions is interpreted to reflect a shallowly dipping Grenville basement beneath the Appalachian accreted terranes. This is supported by the presence of a low-angle southeastward-dipping intra-crustal layer beneath the Inner-Piedmont, Carolina, and northern New England, previously interpreted as a continent-arc collisional interface (e.g., Cook & Vasudenvan, 2006; Hopper et al., 2017; Parker et al., 2015; Spencer et al., 1989). In contrast, the sharp Moho step in the central Appalachians may represent a steeply dipping crustal boundary between Laurentian and Gondwana-derived crust (Li et al., 2018).

Our hypothesis that the central segment of the Laurentia-Gondwana boundary dips steeply implies that the central Appalachian crust might have experienced much more significant

modification during and after accretion in comparison with the northern and southern parts. For example, Hatcher (2010) suggested that an intensified transpressional collision of the Gander and/or Carolina terranes with the Grenville Province led to a sharp boundary beneath the central Appalachians. Furthermore, the consistency between the location of sharp Moho step and the Acadian deformation front from New England to northern Virgina implies that collisional and possibly transcurrent events may have steepened the subsurface boundary (Cheney & Brady, 1992; Li et al., 2018). In addition, differential uplift caused by a gravitational collapse of the thickened Acadian hinterland could also contribute to steepness of the central boundary. The lack of major tectonic events in eastern North America during the last 200 Ma helps to explain the preservation of a Paleozoic Moho step beneath the central Appalachians.

A steep Moho offset has also been observed in other orogenic settings. For example, a recent P-wave RF study with a dense seismic array in eastern Tibet found a ~10 km Moho step within a horizontal distance of ~30 km across the boundary between the Songpan-Ganzi block and the Sichuan Basin (Wang et al., 2018). In southernmost New Zealand, a ~12-15 km Moho offset across the boundary between Fiordland and the accreted terranes was suggested by metamorphic mineral analysis (Klepeis et al., 2018). These structural similarities suggest that preserved Moho offsets across tectonic boundaries may be relatively common (or at least not uncommon) across the diversity of collisional environments.

3.4.4. Possible crustal models in eastern North America

The variation in seismic characteristics may suggest alternative modes of tectonic accretion in the North American Grenville Province. Continent-continent collision can result in a deep Moho and low-angle intra-crustal detachments such as in the U.S. Grenville Province (Figure 3.8a), where the intra-crustal interface represents a collisional thrusting of the Grenville-aged crust over the North American craton. In this case, the U.S. Grenville Province probably preserves its original Moho. Similar crustal structures have been observed in other orogens, such as the Alleghenian suture in the southeastern United States due to the Laurentia-Gondwana collision (Hopper et al., 2017) and the Himalayan collisional zone due to the collision between Indian and Eurasian continents (Schulte-Pelkum et al., 2005). In contrast, the collision between the North American craton and a series of small tectonic terranes might be more applicable to the Canadian Grenville Province and the Appalachian orogen (Figures 3.8b and 3.8c). Repeated accretion and exhumation, as well as later rifting and magmatism, have significantly modified the crust, resulting in a relatively shallow, more heterogeneous Moho and complex intra-crustal structure.

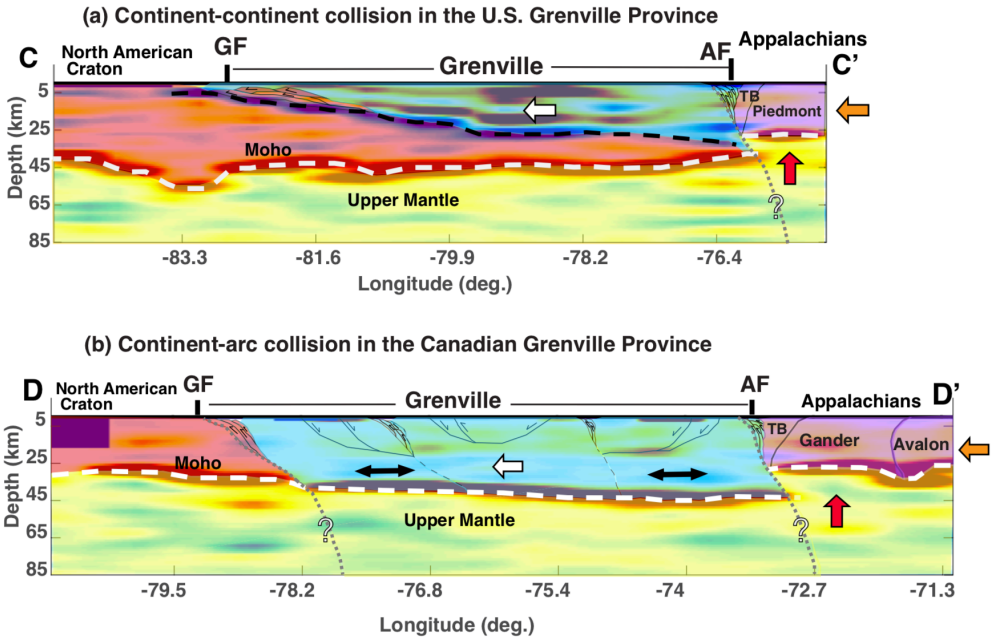

Figure 3.8. Schematic diagrams illustrating variations of the crustal features and our preferred interpretations along cross-sections CC' and DD' in eastern North America, modified after McLelland et al. (2010). (a) Continent-continent collisional model that can be applied to the U.S. Grenville Province. (b) Continent-arc collisional model that can be applied to the Canadian Grenville Province and the Appalachian orogen. The white dashed lines in (a) and (b) represent the interpreted Moho, and the black dashed line in (a) reflects an eastward thrusting of the Grenville-aged crust over the North American craton. The gray dotted lines in (a) and (b) represent our interpreted subsurface extent of the Grenville Front and the Appalachian Front. The thin black lines with arrows denote the thrust faults during accretion and collision and the normal faults during extensional collapse, according to McLelland et al. (2010). The white arrows in (a) and (b) mark the relative direction of the Grenville Province - North American craton collision during the Grenville orogeny. The orange arrows mark the accretion of a series of terranes onto the Grenville Province. The red arrows represent

the uplifting due to the orogenic collapse and rifting. In (b), the black two-headed arrows represent the lateral extensional collapse. The background imaging is the cross-sections CC' and DD' of our receiver functions, respectively, which are shown in Figure 3.7. GF = the Grenville Front; AF = the Appalachian Front.

3.5. Summary

Teleseismic P-wave receiver function analysis was used to image the distribution of crustal thickness within eastern North America. Crustal characteristics and Moho depth both vary significantly across and within the major tectonic units. Specifically, a deepened Moho is detected within a narrow zone along the southern part of the Grenville Front. The U.S. Grenville Province is characterized by a deep Moho and a low-angle eastward-dipping intra-crustal layer. The northern Grenville crust is relatively thin. Crustal thickness in general decreases from the Grenville Province to the Appalachian orogen, although the magnitude and character of the Moho change varies along strike. A sharp12-15 km Moho offset is seen in the central Appalachians, and the Moho depth varies more gradually in the north and south. The observed spatial relation between the geologically-defined tectonic boundaries and the underlying Moho variations provides new constraints on the depth extent of the tectonic units within the crust.

CHAPTER 4

Modification of crust and mantle lithosphere beneath the southern part of the eastern North American passive margin (*Li, C. and Gao, H., (2020). Modification of crust and mantle lithosphere beneath the southern part of the eastern North American passive margin. Geophysical Research Letters, under review*)

4.1. Introduction

The eastern North American margin (ENAM; Figure 4.1a) represents an archetypical passive margin, which experienced a complete episode of the assembly and breakup of supercontinent Pangea over the last 500 Ma (Thomas, 2006). During the assembly of Pangea between ~495 Ma and ~270 Ma, a sequence of tectonic terranes progressively accreted onto Laurentia (the North American craton; Hatcher, 2010; Thomas, 2006). Extensive rifting along the ENAM started at approximately 230 Ma (Withjack et al., 2012), accompanied by short-lived magmatic activities. After rifting, multiple stages of intense magmatic events occurred along the margin, and formed the Central Atlantic Magmatic Province (CAMP), one of the Earth's largest igneous provinces, over a period of less than one million years at approximately 200 Ma (e.g., Marzoli et al., 1999; 2018; Olsen et al., 2003). The breakup of Pangea was completed at ~185 Ma, and the modern passive margin was ultimately established (Withjack et al., 2012).

The southern segment of the ENAM is characterized by a variety of tectonic features associated with syn- and post-rifting tectonic events. Strong gravity and magnetic anomalies align approximately in the SW-NE direction (Figure 4.1b), which have been proposed to mark the location of initial offshore rifting (Austin et al., 1990; Bonvalot et

al., 2012; Kiltgord et al., 1988). Voluminous mafic dikes and sills, as well as volcanoes, are observed in the southern ENAM (Figure 4.1a; McHone, 2000; Whiteside et al., 2007). In addition, the occurrence of a few large earthquakes (magnitude greater than 5.0) in Virginia and South Carolina (Figure 4.1a; Bakun & Hopper, 2004; Horton et al., 2015) suggests that the continental lithosphere beneath this region is not as geologically stable as conventionally thought. The southern ENAM thus provides an ideal setting to investigate the interaction among rifting, magmatism, and pre-existing lithospheric structures, and to ultimately understand the formation and evolution of lithosphere at passive margins.

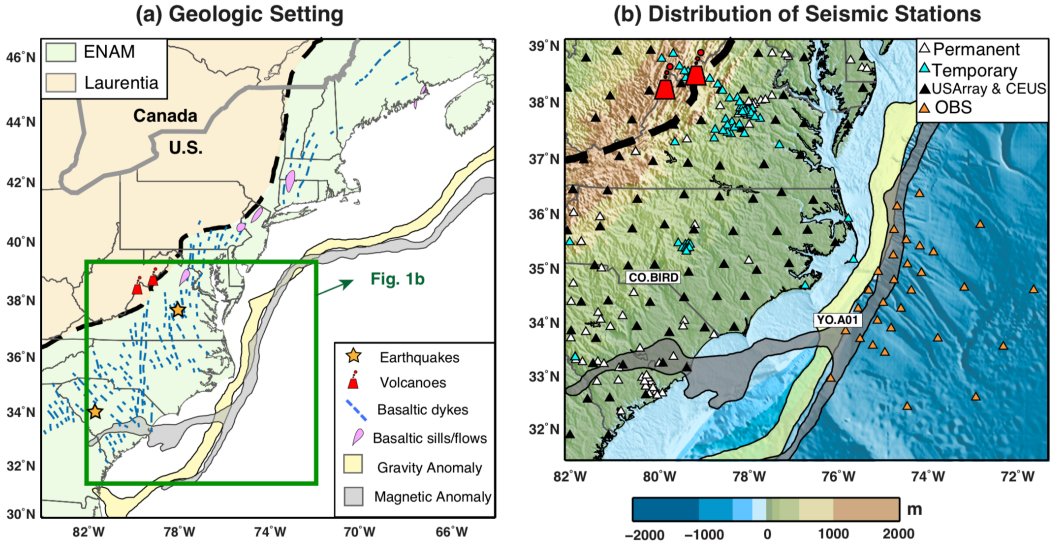

Figure 4.1. (a) Major tectonic features along the eastern North American margin. The thick black dashed line marks the boundary between Laurentia and the eastern North American margin (ENAM). The thick gray line marks the United States-Canada border, and the thin gray lines indicate state boundaries. The thin blue dashed lines mark basaltic dikes, and pink patches represent basaltic sills/lavas, modified after Jourdan et al. (2009). The yellow and gray belts denote the observed positive gravity anomaly and the East Coast magnetic anomaly, respectively. The stars mark the 2011 Virginia

earthquake (magnitude 5.8) and the 1886 South Carolina earthquake (magnitude 6.9), based on the U.S. Geological Survey earthquake catalog. The red cones represent the Eocene volcanoes. (b) Distribution of the broadband seismic stations used in full-wave ambient noise tomography in this study. The white triangles represent the permanent stations, the black triangles for the EarthScope U.S. Transportable Array and the Central and Eastern United States (CEUS) network, the cyan triangles for temporary onshore stations, and the orange triangles for the ocean bottom seismometers (OBS). The background color is the bathemetry/topography (National Geophysical Data Center, 1999).

A fundamental question remains concerning how past tectonic events had modified the lithospheric structures in the southern ENAM. It has been commonly agreed that rifting at ~230 Ma played a first-order role in the modification of crust and mantle lithosphere in this region, based on a variety of geophysical observations. For example, active-source seismic surveys observed the variation of Moho depth from ~17 km on the oceanic side to ~40 km on the continental side (e.g., Guo et al., 2019; Holbrook et al., 1994). A strong seaward-dipping reflector has been detected near the Moho beneath the continental shelf, suggesting modification of the lower crust by rifting and rifting-related magmatism (e.g., Guo et al., 2019; Hales et al., 1968; Holbrook et al., 1994; Klitgord et al., 1988; Marzen et al., 2020). The rifting process may have also resulted in the thickness difference between the oceanic (~120-150 km) and continental lithosphere (~200 km) (Savage et al., 2017; Evans et al., 2019; Murphy & Egbert, 2019), and consequently induced a convection flow of upper mantle (Ramsay & Pysklywec, 2011). The low-velocity anomalies imaged at the base of

the lithosphere along the oceanic-continental margin have been interpreted to represent the rifting-induced mantle upwelling (e.g., Mustelier & Menke, 2020; Savage et al., 2017). In addition, the lithosphere beneath the southern ENAM may have been further modified after rifting. For example, it has been suggested that arrival of the subducted oceanic Farallon slab (Schmandt & Lin, 2014) or the Rheic slab (Wang et al., 2019) beneath the southeastern United States has significantly affected the rheology of continental lithosphere, leading to lithospheric delamination at multiple scales during 50-200 Ma (e.g., Biryol et al., 2016; Evans et al., 2019; Wang et al., 2019; Mazza et al., 2017). Crust and upper mantle structures beneath the southern ENAM include important information on the lithospheric evolution during and after rifting. However, most existing studies for lithospheric structures in the southern ENAM focus on the continental side due to the lack of offshore instrumentations.

The spatial density of broadband seismic data has significantly increased in both the onshore and offshore portions of the southern ENAM (Figure 4.1b), benefiting from the deployment of the EarthScope Transportable Array (IRIS Transportable Array, 2003), the offshore ENAM Community Seismic Experiment (Gaherty et al., 2014), and many other regional seismic networks. This provides a new opportunity to comprehensively investigate the lithospheric structure beneath this region in great detail. In this study, we present a three-dimensional crustal and upper mantle velocity model from the continental interior to the oceanic side, using the advanced full-wave ambient noise propagation simulation and tomographic inversion. Our new model provides seismic evidence for lithospheric modification associated with rifting, magmatism, and mantle convection.

4.2. Data and methodology

We collected the vertical-component seismic recordings for 245 continental stations and 30 ocean bottom seismometers within our study region, with the operating time between 2000 and 2019 (Figure 4.1b). These stations are from 12 long-running networks and 7 temporary dense arrays (See a detailed network description in the Supporting Information and Table C.1). The empirical Green's functions (EGFs) were extracted as the negative time derivatives of the stacked daily cross-correlations of ambient noise data, following the steps described by Gao and Shen (2014) (see the details of extraction of EGFs in the Supporting Information). The EGFs show high-quality Rayleigh wave signals on both positive and negative time lags at periods of 5-150 s between land-land station pairs and at periods of 8-50 s for land-ocean and ocean-ocean station pairs (see examples in Figure 4.2). The lack of clear Rayleigh-wave signals at longer periods from ocean bottom seismometers is mainly due to the interference of infragravity waves (e.g., Guo et al., 2019; Janiszewski et al., 2019). For the EGFs between ocean-land and ocean-ocean station pairs at the periods of 8-20 s, the signal-to-noise ratios differ significantly between the positive and negative time segments (see example in Figure 4.2c; see the definition of signal-to-noise ratio in the Supporting Information). The observed variation of signal-to-noise ratios can be due to the uneven spatial distribution of noise sources for high-frequency signals, which are primarily located within the continental shelf (Guo et al., 2020).

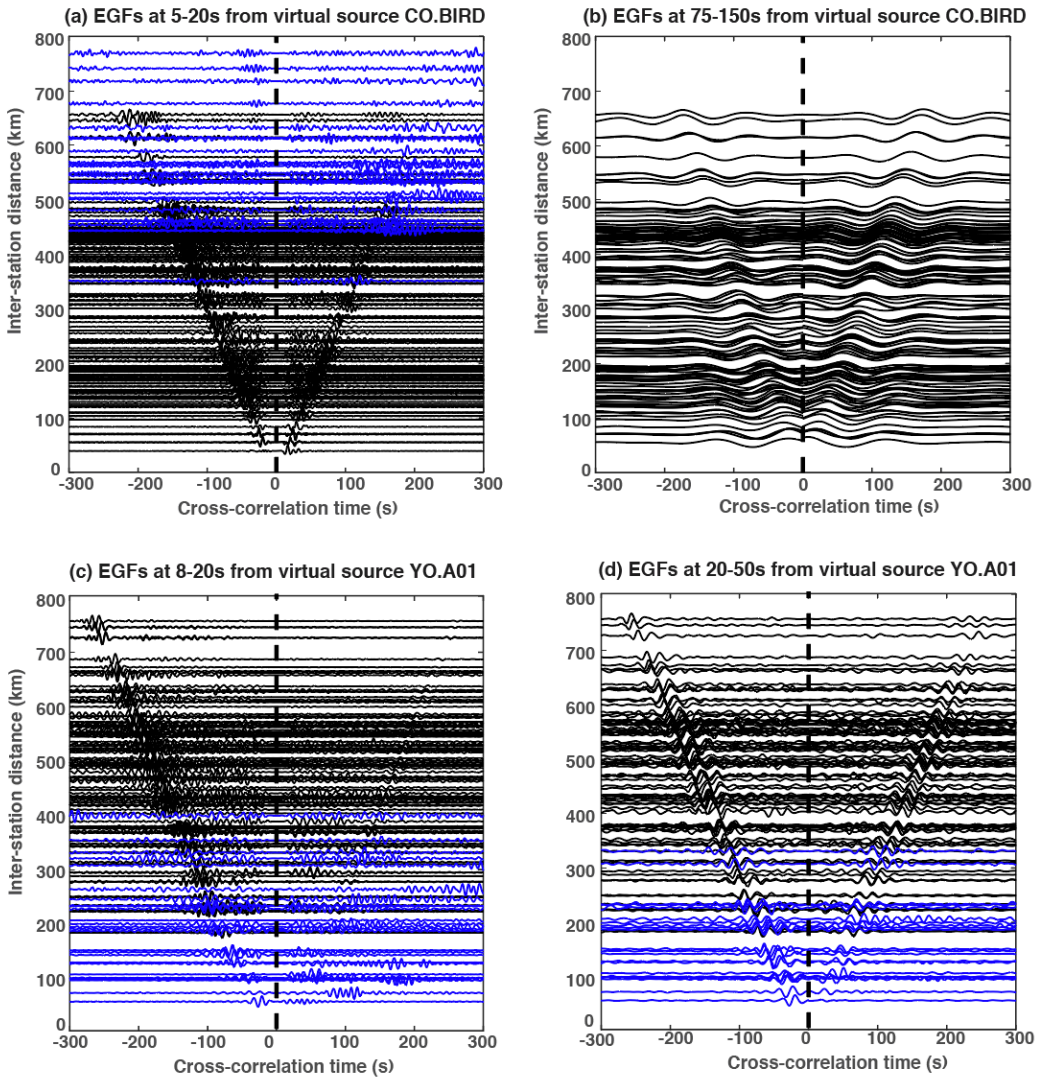

Figure 4.2. Examples of empirical Green's functions (EGFs) from the virtual sources CO.BIRD (upper panel) and YO.A01 (lower panel) to the receivers. The waveforms are filtered at periods of 5-20s (a) and 75-150s (b) for the virtual source CO.BIRD, and filtered at periods of 8-20s (c) and 20-50s (d) for the virtual source YO.A01. Traces are colored in black for onshore receivers and blue for offshore receivers.

We simulated wave propagation in the 3-D spherical earth structure using a nonstaggered-grid, finite difference method (Zhang et al., 2012; Gao & Shen, 2014; Gao, 2018). We

parameterized the model into 0.020°×0.020° in the longitudinal and latitudinal directions. The vertical grid size linearly increases from 2 km at the surface to 35 km at the depth of 700 km. We chose a global shear velocity model of the crust and upper mantle as the initial reference model (Shapiro & Ritzwoller, 2002). The P-wave velocity was converted from the S-wave velocity with a constant Vp/Vs ratio of 1.76 for the crust and a depth-dependent Vp/Vs ratio from the AK135 model (Kennett et al., 1995) in the upper mantle. The density was calculated as an empirical function of Vp (Christensen & Mooney, 1995). In our model configuration, we ignored the elevation above sea level but considered the presence of the water layer in terms of the bathymetry data (Smith & Sandwell, 1997), given a constant Vp of 1.5 km/s and density of 1.0 g/cm^3.

We measured the Rayleigh-wave phase delays between the observed EGFs and the synthetics through cross-correlations at periods of 5-10 s, 8-15 s, 10-20 s, 15-30 s, 25-50 s, 30-60 s, 36-70 s, 50-100 s, and 75-150 s. We required a minimum signal-to-noise ratio of the observed EGFs on both positive and negative time segments to be 6 for land-land pairs and 4 for land-ocean and ocean-ocean station pairs, respectively. For a majority of station pairs, we determined the final phase delays by averaging the delays measured at the positive and negative sides. However, if the signal-to-noise ratio on one side is equal to or greater than two times than the other side, we only use the phase delay measurement from the side with the higher ratio. The raypath coverage of phase delay measurements varies from continent to offshore within our study area (Figure C.3). Most of the continental area is well covered at periods of 5-100 s with raypath numbers larger than 200 per 0.5°×0.5°

grid (Figure C.3), allowing us to resolve the seismic structures down to about 100 km depth. The inclusion of the offshore ENAM Community Seismic Experiment largely increases the total number of phase delay measurements in the oceanic region between latitude 33°N and 37°N at periods of 5-50 s, making it feasible to resolve the seismic features offshore down to about 60 km depth.

We then calculated the 3-D, finite-frequency sensitivity kernels of Rayleigh waves and carried out the inversion for both P- and S-wave velocity perturbations (Gao & Shen, 2014; Zhao et al., 2005; see details in the Supporting Information). As demonstrated by previous studies (e.g., Gao, 2018; Xia et al., 1999; Zhang & Shen, 2008), Rayleigh waves are more sensitive to P-wave velocity at shallow depths and to S-wave velocity at greater depths. The reference model was progressively updated by iteratively reducing the Rayleigh-wave arrival misfits between the observed and synthetic waveforms for a total of five iterations of wave simulation and inversion. Our final model has been significantly improved in comparison with the initial reference model (Figures C.5 and C.6). The synthetic waveforms generated from the initial model result in a large variation range of the phase delays, especially at periods shorter than 30 s (Figures C.5 and C.6). In comparison, the synthetic waveforms generated from our final model can predict the phase arrivals of the observed EGFs much better, with the phase delays varying within a narrow range ($\pm$2.5 s at shorter periods of 5-70 s and $\pm$4.0 s at longer periods of 50-150 s; Figure C.5). The decreasing of the phase delays, especially at shorter periods, indicates an improvement for imaging the crustal and uppermost mantle structure in our model.

4.3. Results

Our tomographic imaging shows a clear lateral variation of the seismic structure from ocean to continent at the shallow depths (0-12 km), where P-wave velocities can be better resolved than S-wave velocities (Figures C.13-C.20; See a detailed description of resolution tests in the Supporting Information). We separate the water layer from the oceanic crust using bathymetry data (Smith & Sandwell, 1997). We observe very low P-wave velocities (<5.0 km/s) for the top 2-8 km depths below the seafloor in the oceanic part (Figure 4.3a; Cross-sections AA' and BB' in Figure 4.4), which likely reflect the presence of thick sedimentary layer underneath (Laske et al., 2013). In comparison, the continental part is marked by low P-wave velocities (<5.0 km/s) for the top ~2 km depth (Cross-sections AA', BB', and CC' in Figure 4.4), which likely indicates a thin sedimentary layer (Guo et al., 2019; Laske et al., 2013). However, the model resolution tests of P-wave velocities (Figures C.13-C.15) show that the seismic structures near the surface cannot be fully resolved. At the depths of 2-12 km, we observe heterogenous P-wave velocities (6.0-6.5 km/s) within the southern ENAM and fast P-wave velocities (>6.5 km/s) within Laurentia (Figure 4.3a; Cross-sections AA', BB' and CC' in Figure 4.4).

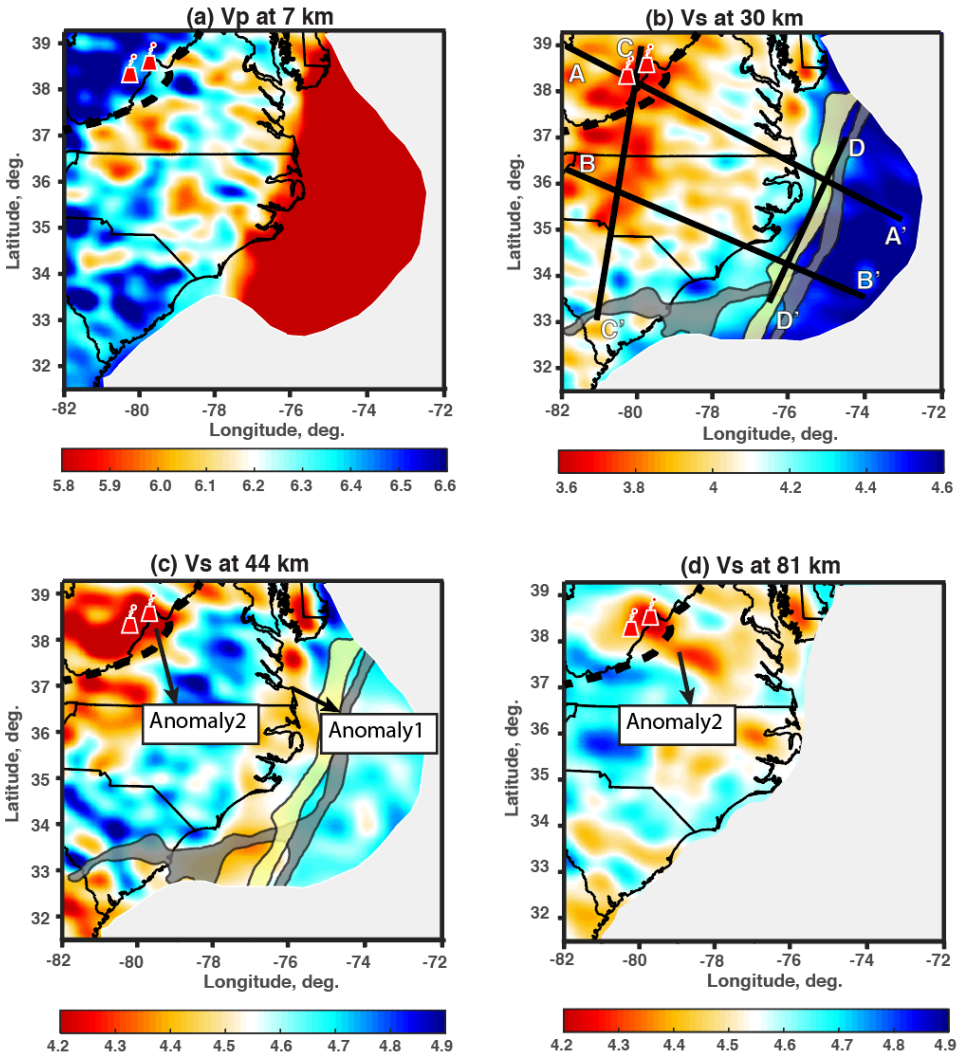

1345

1346 ***Figure 4.3. Seismic velocity structure (in km/s) from the crust down to the upper mantle***

1347 ***in the southern part of the eastern North American margin resolved from full-wave***

1348 ***ambient noise tomography. (a) P-wave velocities at 7 km depth. (b)-(d) S-wave velocities***

1349 ***at the depths of 30 km, 44 km, and 81 km, respectively. The solid black lines in (b) mark***

1350 ***the profile locations in Figure 4.4. Other symbols are the same as in Figure 4.1.***

1351

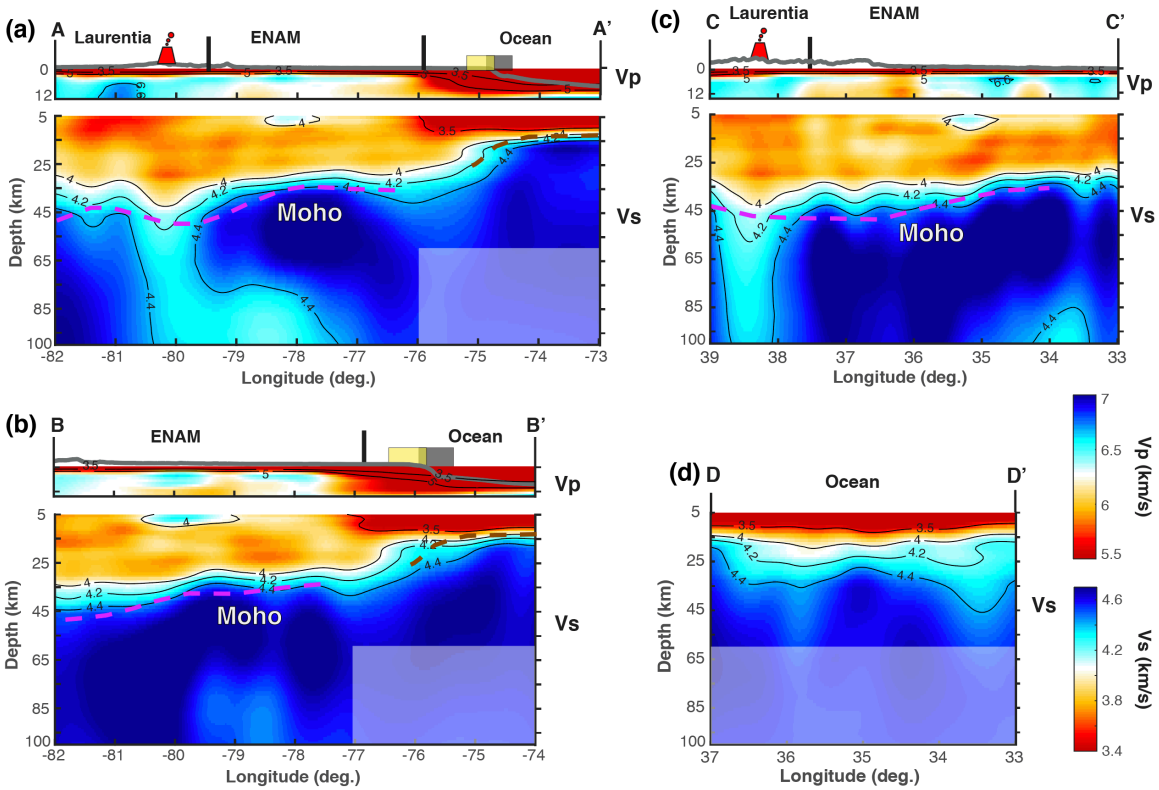

Figure 4.4. Cross-sections of the seismic tomographic model. See profile locations in Figure 4.3e. (a)-(c), P-wave velocities for the top 12 km depths (upper panel) and S-wave velocities at the depths of 5-100 km for the continental part and at the depths of 5-60 km for the oceanic part (lower panel). The pink dashed line denotes the continental Moho inferred from teleseismic receiver functions by Li et al. (2020), and the brown dashed line denotes the oceanic Moho inferred from the 2-D active-source survey by Holbrook et al. (1994). The yellow and gray columns in (a) and (b) represent the gravity and magnetic anomalies, respectively. The thick gray line on the top of each profile corresponds to the topography/bathemetry with the green patch for the water layer. The red cone in (a) and (c) indicates the Virginia volcano. (d) S-wave velocity model at the depths of 5-60 km for the oceanic part. Note that the maximum resolvable depths are

about 100 km for the onshore structure and 60 km for the offshore seismic structure, respectively. The velocity model below the depth of 60 km on the oceanic side is masked with the translucent shade.

Our model demonstrates distinct variations of S-wave velocities within a depth range of 5-100 km for the continental part and 5-60 km for the oceanic part. The crustal thickness within our study region varies from ~30-45 km on the continental side (e.g., Li et al., 2020) to ~12-17 km on the oceanic side (e.g., Guo et al., 2019; Holbrook et al., 1994), which we hereinafter refer to. The oceanic crust is characterized by a nearly uniform low-velocity layer (<3.5 km/s) for the top 5-10 km depths, and reaches a velocity of ~4.2 km/s at the bottom of the crust (Figure 4.4). In contrast, the S-wave velocities in the continental crust vary with a range of ~3.7-4.4 km/s (Figure 4.4). A faster-than-average lower crust beneath the eastern United States has been imaged by recent seismic studies (e.g., Marzen et al., 2020; Yang & Gao, 2018), indicating that the lower crust has been modified and densified. Within a depth range of ~15-40 km, we observe a strong lateral decreasing of S-wave velocity across the ocean-continent margin over a horizontal distance of ~70 km (Figures 4.3b and 4.3c; Cross-sections AA' and BB' in Figure 4.4). This fast-to-slow velocity variation (from >4.6 km/s in the oceanic part to ~3.9-4.3 km/s in the continental part) reflects the transition from the oceanic uppermost mantle to the continental crust, due to the increasing of crustal thickness from ocean to continent. The model recovery test demonstrates that the lateral variation of the shear-wave velocities can be well constrained (Figure C.19).

We observe two low S-wave velocity features within the mantle lithosphere. One velocity anomaly lies below the transitional oceanic-continental crust and extends down into at least 60 km (Figures 4.3d, 4.3e, and 4.4). The S-wave velocity of this anomaly is ~4.3-4.5 km/s, ~6-10% lower than the average surrounding mantle velocity of ~4.8 km/s (Figures 4.3d and 4.3e; Cross-section AA' in Figure 4.4). The other low-velocity anomaly is imaged beneath eastern West Virginia and western Virginia, which extends nearly vertically from the Moho down to at least ~100 km depth (Figures 4.3d-4.3f; Cross-sections AA' and CC' in Figure 4.4). The S-wave velocities of this anomaly are ~4.1-4.4 km/s, which are significantly lower (up to 16% reduction) than the surroundings. The horizontal dimension of this low-velocity anomaly is ~150 km at the uppermost mantle (Figure 4.3d) and decreases downward to ~100 km at the depth of 80 km (Figure 4.3f). At depths greater than ~80 km, this anomaly appears to be slightly tilted towards east (Cross-section AA' in Figure 4.4). The model recovery test further validates that the scale and geometry of our observed low velocity anomalies are robust in our model (Figure C.20).

4.4. Discussion

Our new tomographic model provides a well-constrained seismic structure of the crust and upper mantle beneath the entire southern ENAM, benefiting from the integration of onshore and offshore seismic data sets and the advanced methodology we implemented. Both the lateral and vertical scales of the seismic features have been significantly improved in comparison with previous studies (Figures C.21 and C.22). For example, our model provides a tighter constraint on the distribution of sediments marked by low seismic velocities (Figure 4.4), in comparison with the results from Lynner and Porritt (2017)

(Figure C.21). The clear decreasing of the sediment thickness from offshore to onshore is also consistent with results from active-source seismic surveys (e.g., Guo et al., 2019; Hales et al., 1968; Klitgord et al., 1988). The slow-to-fast velocity transition from offshore to onshore at a depth range of ~15-40 km revealed in our model (Figures 4.4 and C.12) approximately matches the variation of crustal thickness defined by teleseismic receiver function analysis (e.g., Li et al., 2020) and active-source seismic surveys (e.g., Guo et al., 2019; Holbrook et al., 1994). Even though the low-velocity anomaly beneath the Virginia volcanoes has been previously imaged (e.g., Schmandt et al., 2015; Shen & Ritzwoller, 2016; Wagner et al., 2018), our model resolves the eastward-tilting geometry of this anomaly (Figure C.22). Furthermore, our study finds the low-velocity uppermost mantle beneath the transitional oceanic-continental crust, which was not recognized by previous studies (Figures 4.3 and 4.4).

We hypothesize that the oceanic-continental transitional crust revealed in our model was formed as a consequence of rifting. This hypothesis is supported by a few evidences. First, the eastern boundary of the transitional crust roughly aligns with the gravity and magnetic anomalies (Cross-sections AA' and BB' in Figure 3), which have been proposed to represent the location of initial rifting (e.g., Austin et al., 1990; Bonvalot et al., 2012; Kiltgord et al., 1988). Second, dynamic modeling studies demonstrate that rifting could cause extension of continental crust beneath the margin, and lead to a ~20 km thinning of the crust across a horizonal distance of ~80 km over a period of ~2.5 Ma (Huismans & Beaumont, 2008; Van Avendonk et al., 2009), consistent with our observations. Third, the crustal thinning due to rifting could result in a surface subsidence, thus facilitating the

formation of a thick sedimentary layer (Huismans & Beaumont, 2008). This is supported by our observation of a thick layer of low seismic velocities above the transitional crust (Cross-sections AA' and BB' in Figure 3). As rifting developed further eastward into the spreading center, a new oceanic crust was formed and the thinning of the transitional crust was terminated (Lynner & Porritt, 2017; Van Avendonk et al., 2009).

The lower-than-average (~6-10% velocity reduction) seismic velocities underlying the transitional crust suggest that the mantle lithosphere, at least to some degree, had been chemically and thermally modified during the rifting process. It has been demonstrated that the depletion of continental lithosphere due to rifting can decrease the magnesium and aluminum contents, and this composition variation would contribute to ~1-2% reduction of seismic velocity (Connolly, 2009; Dalton & Faul, 2010). Moreover, rifting can lead to the thinning of continental lithosphere and thus trigger asthenospheric upwelling along the southern ENAM (e.g., Lynner & Bodmer, 2017; Savage et al., 2017). This hot asthenospheric upwelling could accelerate heat conduction into the shallow mantle and further reduce the seismic velocities (Accardo et al., 2020; Hopper et al., 2020). Goes et al. (2000) suggested that a temperature increase of ~120^{o}C in the mantle lithosphere would lead to a ~2.5% decreasing of shear velocities. We thus estimate the temperature in the transitional lithosphere is ~240-380^{o}C higher than the surroundings, contributing to a ~5%-8% reduction of shear velocities. This temperature range is roughly consistent with the estimation by Savage et al. (2017). Together, composition variation and temperature increase would explain the observed velocity reduction of the mantle lithosphere within the transitional zone.

Even though our preferred interpretation for the low-velocities beneath the transitional crust is related to the chemical and thermal modifications, we cannot rule out the contribution of a small portion of partial melting. Based on Hammond and Humphreys (2000), ~1% partial melting would be enough to account for the velocity reduction we observed in the mantle lithosphere within the transitional zone. Active-source surveys (e.g., Holbrook et al., 1994; Marzen et al., 2020) suggested the underplating of igneous materials beneath the transitional crust, supporting the presence of partial melting as well. It is likely that the rifting-induced asthenospheric upwelling brought up partial melts into the mantle lithosphere via percolation or diking. Similar process has also been proposed in other rifting settings, such as the Malawi rift zone in eastern Africa (Accardo et al., 2020; Hopper et al., 2020).

Either of two interpretations for the low-velocity anomaly beneath the oceanic-continental transitional crust needs a continuous supply of heat. Two models can be used to explain the possible mechanisms of heat. First, the heat might come from the upwelling asthenosphere triggered by the rifting process. This idea has been supported by the observation of a low velocity anomaly at the bottom of lithosphere beneath the oceanic-continental margin (Savage et al., 2017). If so, it might suggest that the rifting-induced upwelling asthenosphere has been preserved for ~200 Ma. Second, the heat might be caused by the edge-driven convection beneath the oceanic-continental margin. Previous studies in our study region have demonstrated the continental lithospheric thickness of ~200 km (e.g., Evans et al., 2019; Murphy & Egbert, 2019) and have estimated the oceanic

thickness of ~120-150 km (Savage et al., 2017). This large variation of lithospheric thickness between oceanic and continental part provides a good condition for edge-driven convection. In this case, the return flow of edge-driven convection might cause the thermal perturbation and therefore provide the heat (Ramsay&Pysklywec, 2011).

The uppermost mantle low-velocity column imaged at the easternmost edge of Laurentia provides a probable magmatism for the Virginia volcanoes, considering their tight spatial correlation (Figures 2c-2f and 3). The thermobarometric modeling by Mazza et al. (2014) indicates that the basanites in the Virginia volcanoes originated from the upper mantle, which supports our interpretation. In addition, previous studies have also identified low resistivities, low seismic velocities and high seismic attenuation at depths of ~100-200 km in this region (e.g., Biryol et al., 2016; Byrnes et al., 2019; Evans et al., 2019; Murphy & Egbert, 2019), consistent with our observation. We therefore propose the observed low-velocity column beneath the Virginia volcanoes represents an asthenospheric upwelling. Furthermore, the eastward titling of this low-velocity column in our model implies that the upwelling is likely related to the rifting-induced mantle convection beneath the oceanic-continent margin. In this scenario, the asthenospheric upwelling must find a way to penetrate through the base of lithosphere into the uppermost mantle of the continental interior (Figures 2d-2f). One possible mechanism is a localized delamination at ~50 Ma beneath the Virginia volcanoes (e.g., Mazza et al., 2014, 2017; Wagner et al., 2018), triggered by the arrival of Farallon or Rheic slab (Schmandt & Lin, 2014; Whalen et al., 2015). The localized delamination would result in a void or weak zone at the base of lithosphere, providing a path for the upward and landward migration of the rifting-induced

asthenospheric upwelling. The asthenospheric upwelling must undergo decompression during its upward migration, leading to the Virginia volcanisms during the Eocene period.

4.5. Summary

We constructed a high-resolution lithospheric velocity model beneath the southern ENAM using the advanced wave propagation simulation and inversion method by integrating both onshore and offshore ambient noise seismic waveforms. Our model recognizes a continent-ocean transitional crust over a lateral distance of ~70 km and a low-velocity uppermost mantle underneath. Our tomographic model reveals a distinct low-velocity column in the mantle lithosphere beneath eastern West Virginia and western Virginia, which slightly tilts eastward at greater depths. We propose that crustal extension during the initial rifting at ~230 Ma formed the transitional continental-oceanic crust. Rifting could trigger an asthenospheric convection flow, and have consequently modified the mantle lithosphere beneath the transitional crust. Furthermore, a localized lithospheric delamination beneath western Virginia at ~50 Ma could promote the landward migration of the rifting-induced convection flow, providing a possible magmatism for the Virginia volcanoes. Our findings provide insights on lithospheric modification associated with rifting and mantle convection at passive margins.

CHAPTER 5

General conclusions and perspectives

5.1.Conclusions

In this thesis, I aim to understand the formation and evolution of continental lithosphere beneath eastern North America by exploring seismic characteristics in the crust and upper mantle. In order to do so, we collected and analyzed large seismic data sets in eastern North America. We first investigated the variation of crustal thickness beneath the northern Appalachian mountains using P-wave receiver function analysis (Chapter 2) and then extended this investigation into the entire eastern North American region (Chapter 3). We also explored the possible relationship between the geologically-defined tectonic boundaries and variations of seismically-identified subsurface discontinuities (including the Moho and intra-crustal layer). Moreover, we constructed a high-resolution velocity model beneath the southern part of eastern North American margin using full-wave ambient noise tomography (Chapter 4), in order to understand the modification of lithosphere structure due to past tectonic events.

Our P-wave receiver function studies in Chapters 2 and 3 found that the depths of both Moho and intra-crustal layers vary significantly across and within the major tectonic units. Specifically, there are distinct differences in crustal thickness between the northern and southern Grenville Province. A dipping intra-crustal feature can be seen within the central Grenville Province. The Moho depth decreases southeastward across the Grenville-Appalachian boundary, with a sharp Moho offset in the central segment and a more gradual variation to the north and south. The observed depth variations of Moho and intra-crustal

layers show a rough spatial correlation with geologically defined tectonic boundaries in eastern North America. The thickness difference between the southern and northern Grenville-aged crusts suggests different tectonic and/or exhumation histories during and after the Grenville Orogeny. Differences in the steepness of the Moho offset along the strike of Appalachians probably reflect variation of the steepness of the subsurface boundary between Laurentia and accreted terranes with different intensities of syn- and/or post-orogenic modification.

Our tomography studies in Chapter 4 identify a clear change in the crustal thickness over a transitional zone from ocean to continent. Beneath the transitional crust, the upper mantle has relatively lower seismic speeds in comparison with its surroundings. We also discover a low-velocity column within the upper mantle beneath West Virginia where two volcanos are located. We propose that the transitional oceanic-continental crust was formed due to crustal extension during rifting. The mantle lithosphere underlying the transitional crust could have been thermally and chemically altered, with possible presence of partial melting, during and after the rifting process. The rising flow of asthenosphere induced by rifting might result in partial melting of the upper mantle beneath the continental interior, which can explain the presence of volcanoes in West Virginia.

Studies in this thesis identified the distribution of crustal thickness and velocity structures in great detail. These seismic characteristics, together with other geological and geodynamic evidences, provide an important constraint on the lithospheric modification associated with continental collision, rifting, and other tectonic events.

5.2.Future work

This section briefly presents some possible future research directions building on this thesis:

- **Detailed crustal structures geometries and crustal anisotropy beneath eastern North American**

Our receiver function studies in Chapters 2 and 3 show first-order variations in the crustal thickness and intra-crustal layer depth beneath eastern North America. However, detailed 3-D geometries of observed crustal structures are unable to be reliably imaged with the approach (CCP stacking) we applied in this thesis. For example, the strike angle and sharpness of the observed Moho step in the central Appalachians are unknown, as is the nature of observed intra-crustal layer beneath the U.S. Grenville Province.

On the other hand, P-wave receiver function data also include information of crustal anisotropy, which provides important constraints on the lithospheric deformation during past tectonic events. Combination crustal anisotropy with our observed crustal thickness variation and velocity distribution in eastern North America would be crucial for our comprehensive understanding of lithospheric formation and evolution. How we use P-wave receiver function analysis to identify complex crustal structures as well as crustal anisotropy would be a subject of a follow-up study.

- **Velocity structures of the crust and mantle lithosphere beneath eastern North American**

Our tomography study in Chapter 4 majorly focuses on the lithospheric velocity structures beneath the southern part of eastern North American margin. However, the lithospheric structures beneath the rest of eastern North American region remain unclear and need to be investigated in the near future. With the constraints of crustal thickness variation from Chapters 2 and 3, the velocity model would identify seismic features within crust and upper mantle in great detail. Specific scientific questions for the future tomographic study include, but are not limited to: 1) How do the lithospheric velocity structures change across the different tectonic units? 2) Were lithospheric structures inherited from the pre-existing architecture of continental lithosphere or newly developed after continental formation? 3) Which specific tectonic events contributed to the variations of lithospheric structures. Answering those questions will be great helpful for our understanding of formation and evolution of lithosphere beneath eastern North America.

APPENDIX A

Supporting information for Chapter 2

A.1 Data

In this study, we chose a total of 87 permanent stations and 109 temporary stations (see the station distribution in Figure A.1). These include stations from the Canadian National Seismograph Network (CN; Geological Survey of Canada, 1989), the Global Seismograph Network (IU; Albuquerque Seismological Laboratory (ASL)/USGS, 1988), the Lamont-Doherty Cooperative Seismographic Network (LD; Lamont Doherty Earth Observatory (LDEO), Columbia University, 1970), the New England Seismic Network (NE; Albuquerque Seismological Laboratory (ASL)/USGS, 1994), the Portable Observatories for Lithospheric Analysis and Research Investigating Seismicity (PO; Geological Survey of Canada, 2000), the EarthScope USArray Transportable Array (TA; IRIS Transportable Array, 2003), the United States National Seismic Network (US; Albuquerque Seismological Laboratory (ASL)/USGS, 1990), the Southern Ontario Seismic Network (WU; University of Western Ontario (UWO Canada), 1991), the Deep Structure of Three Continental Sutures in Eastern North America (X8; Menke et al., 2012), the Central and Eastern US Network (N4; UC San Diego, 2013), and the Penn State Network (PE, XY; Penn State University, 2004; 2013). The well-distributed coverage of broadband seismic stations makes it possible to obtain a detailed map of the crustal thickness using teleseismic receiver functions.

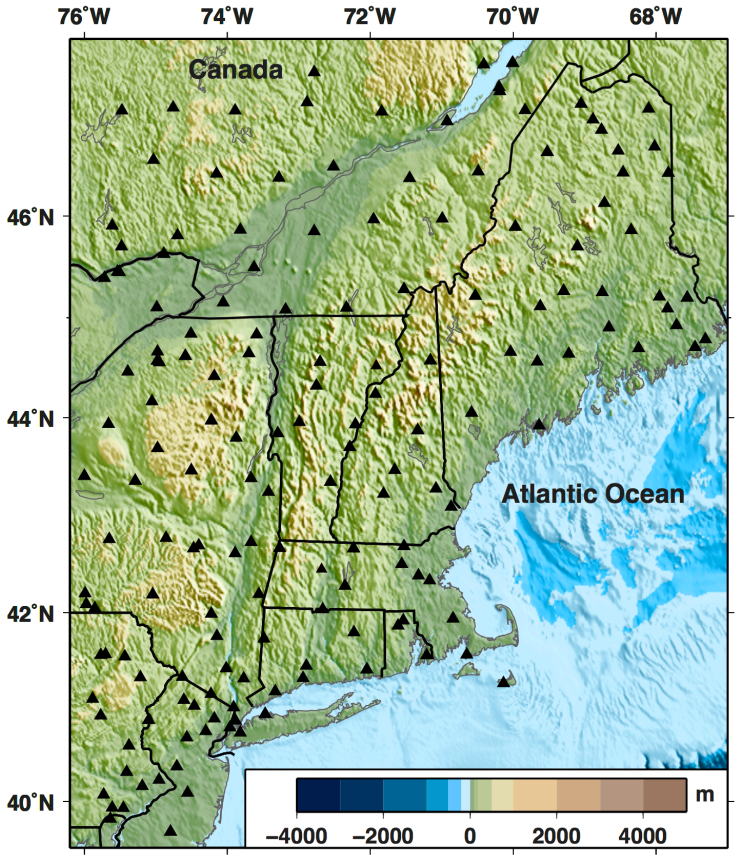

Figure A.1. Distribution of broadband seismic stations (black triangles) used for the analysis of teleseismic receiver functions in this study. The background color is the bathemetry/topography.

A.2 P-wave receiver function analysis

The RF analysis has been successfully applied to study the distribution of sharp velocity discontinuities at crustal, lithospheric, and upper mantle scales. The basic idea of the RF analysis is to deconvolve the vertical component from the radial component (Langston, 1979; Ammon, 1991), which removes the effects of source time function and the instrument response, and resolves the structure beneath the station. Prior to the calculation of teleseismic RFs, we cut the raw seismograms 30 s before and 60 s after the predicted P

wave arrivals based on the one dimensional IASP91 velocity model (Kennett & Engdahl, 1991). We then removed the mean and the first-order linear trend from the waveforms. The seismograms were band-pass filtered at 0.05-1.2 Hz, and the horizontal components were rotated along the free surface to obtain radial and transverse components of motion.

For this study, we chose the water-level frequency-domain deconvolution method (Langston, 1979; Ammon, 1991), which is described by

$$H(\omega) = \frac{R(\omega) \times Z^*(\omega)}{\emptyset(\omega)} \times G(\omega), \quad (1)$$

$$\emptyset(\omega) = \max\{Z(\omega) \times Z^*(\omega), c \times max\{Z(\omega) \times Z^*(\omega)\} \quad (2)$$

where $H(\omega)$, $R(\omega)$ and $\mathrm{Z}(\omega)$ denote radial receiver function, radial and vertical components of the seismic recordings, respectively. * indicates complex conjugation and $\mathrm{G}(\omega)$ is a Gaussian filter (Langston, 1979; Ammon, 1991). To stabilize the calculation of receiver functions, the original water-level deconvolution method implements a constant spectral parameter c for all the stations (Langston, 1979). In this study, we modified the method to estimate the water-level parameter based on the noise level prior to P arrivals on the vertical components for each station. We then applied a low-pass Gaussian filter with a 1.0 s Gaussian pulse width to remove the high-frequency noise in the calculated receiver functions.

The selected radial receiver functions were converted to depth using the common conversion point (CCP) stacking method (Dueker & Sheehan, 1998; Hansen & Dueker,

2009). For horizontal layers, the P_{ms} arrival time after the direct P wave is described as

$$T_{Pms}(p) = \int_{D}^{0} [\sqrt{Vs(z)^{-2} - p^2} - \sqrt{Vp(z)^{-2} - p^2}]\, dz$$

where p is the ray parameter and D is the maximum depth. Vp and Vs are the P- and S-wave velocities, respectively. We interpolated the three-dimensional velocity model by Shen and Ritzwoller (2016) to obtain the seismic velocities beneath each seismic station. The receiver functions were then binned by back-azimuth and ray parameter. Considering the distribution of seismic stations within our study area, we divided the study region into the northern and southern zones. The horizontal bin size is 20 km in the southern part and 40 km in the northern part, and the radii of the bins are 1.5 times of the bin sizes. The bin size is 1 km vertically down to 150 km depth. The Moho depth is defined as the depth of the maximum positive amplitude in binned RFs within a depth range of 20-70 km.

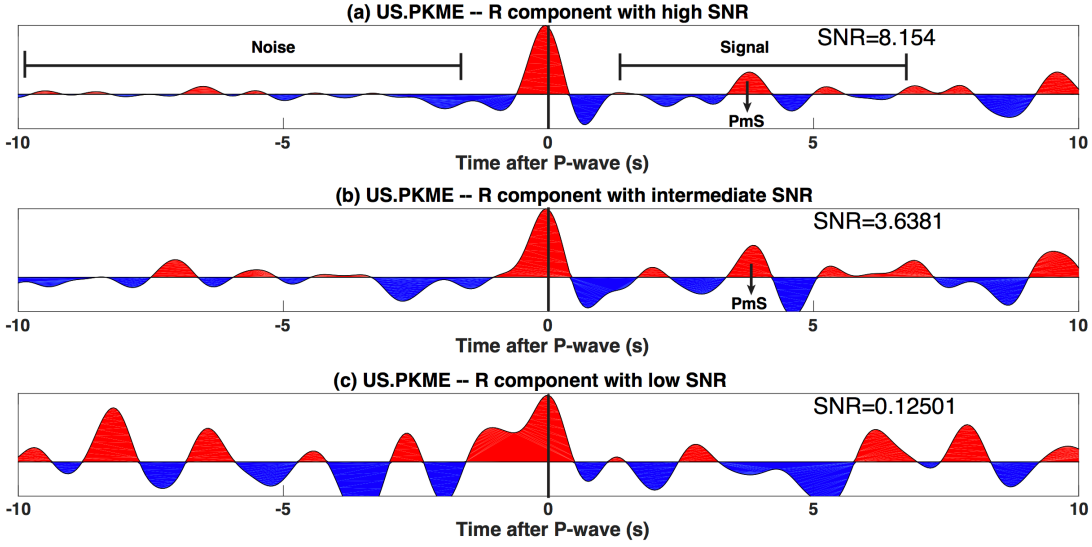

Figure A.2. Definition of the signal-to-noise ratio of the observed radial-component receiver functions. The phase at zero time is the direct P-wave arrival. Here we use station US.PKME as an example. See station location in Figure 2. 4a.

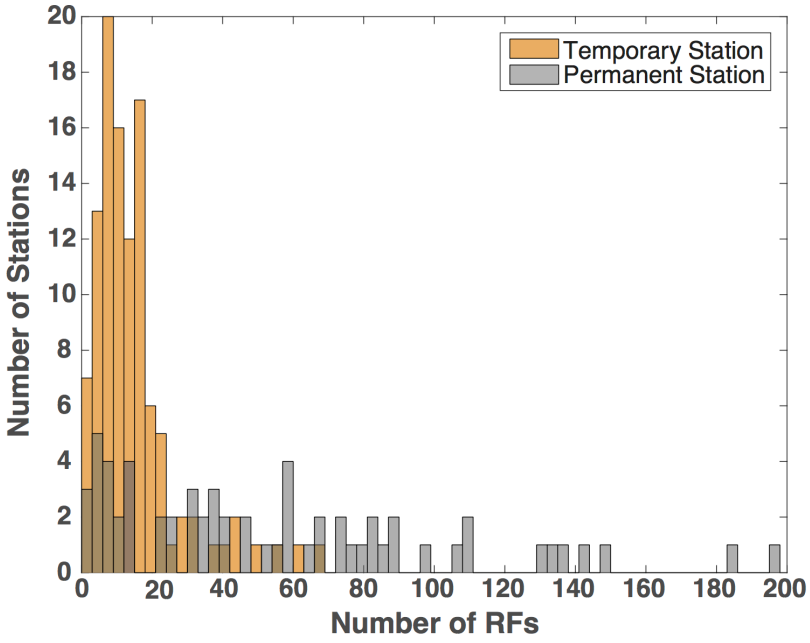

Figure A.3. Distribution of the number of selected receiver functions for permanent (gray colors) and temporary stations (orange color). The horizontal axis and vertical axis are the numbers of the receiver functions and stations, respectively. See Table A.1 for a detailed description.

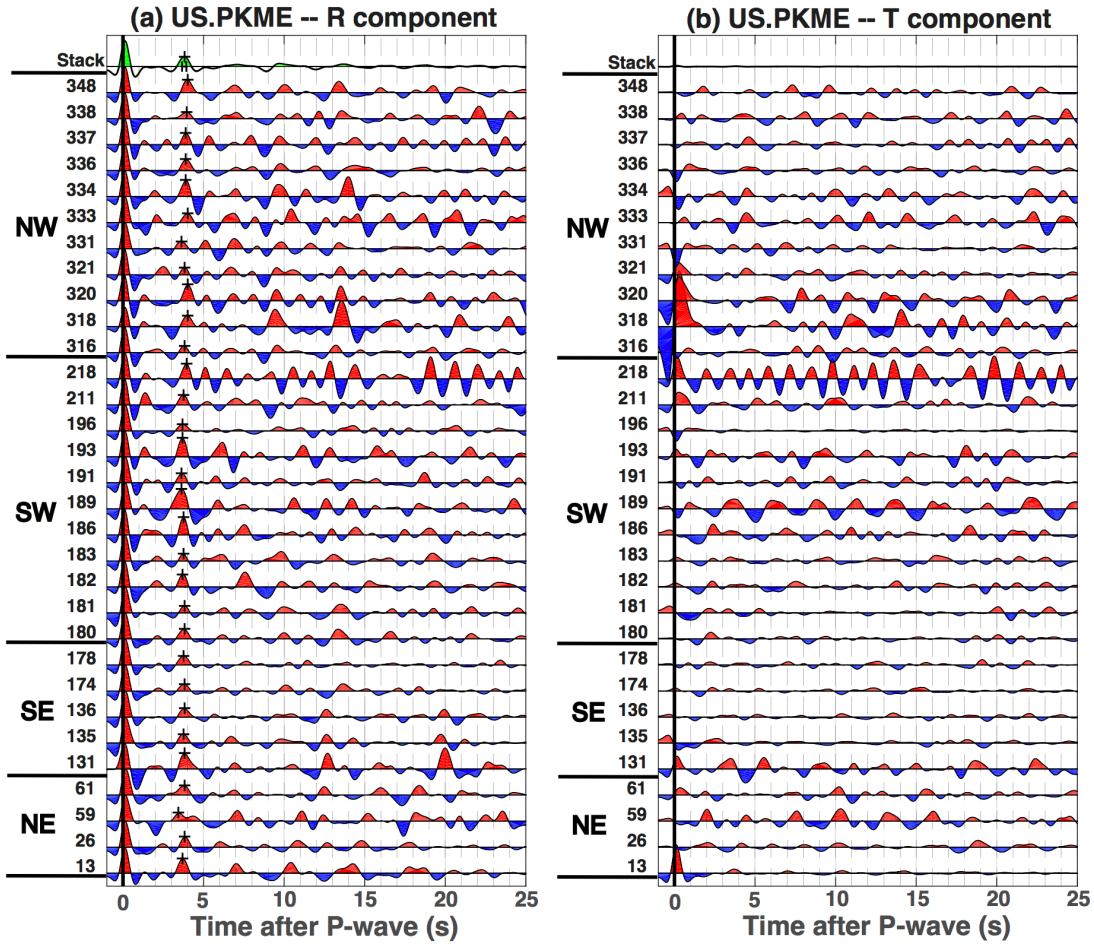

Figure A.4. Examples of normalized radial- and transverse-component receiver functions for station US.PKME, sorted by back-azimuth. The back-azimuths are divided into four quadrants, ranging within 0º-90º (NE), 90º-180º (SE), 180º-270º (SW), and 270º-360º (NW). The top one is the stacked receiver function. The waveforms are filtered at 0.1-1.2 Hz. The phases at zero time are direct P wave arrivals.

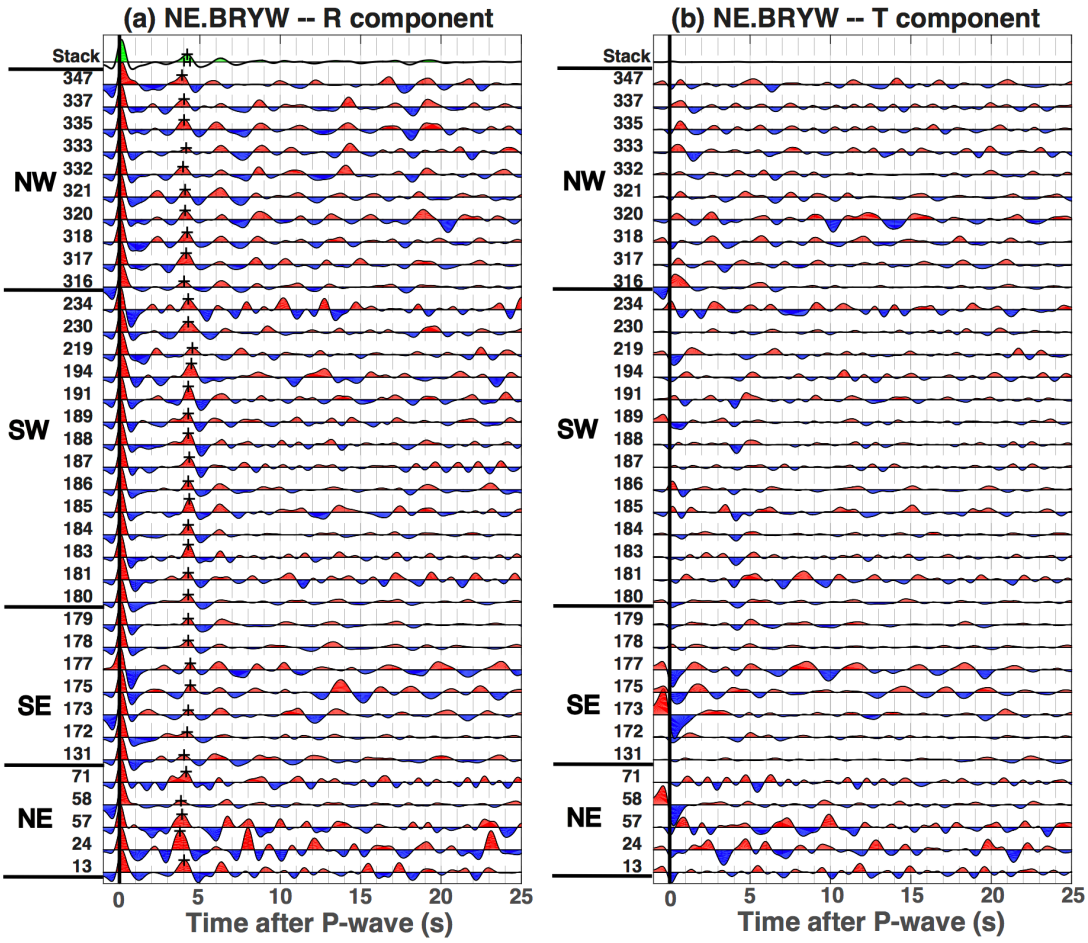

Figure A.5. Examples of normalized radial- and transverse-component receiver functions for station NE.BRYW, sorted by back-azimuth. The waveforms are filtered at 0.1-1.2 Hz.

	Model 1	Model 2
Layer 1	H = 39.5 km Density = 2.84 g/cm^3 Vs = 3.67 km/s Vp/Vs = 1.7	H = 35 km Density = 2.84 g/cm^3 Vs = 3.67 km/s Vp/Vs = 1.9
Layer 2	H = --- --- Density = 3.44 g/cm^3 Vs = 4.67 km/s Vp/Vs = 1.7	H = --- --- Density = 3.44 g/cm^3 Vs = 4.67 km/s Vp/Vs = 1.9

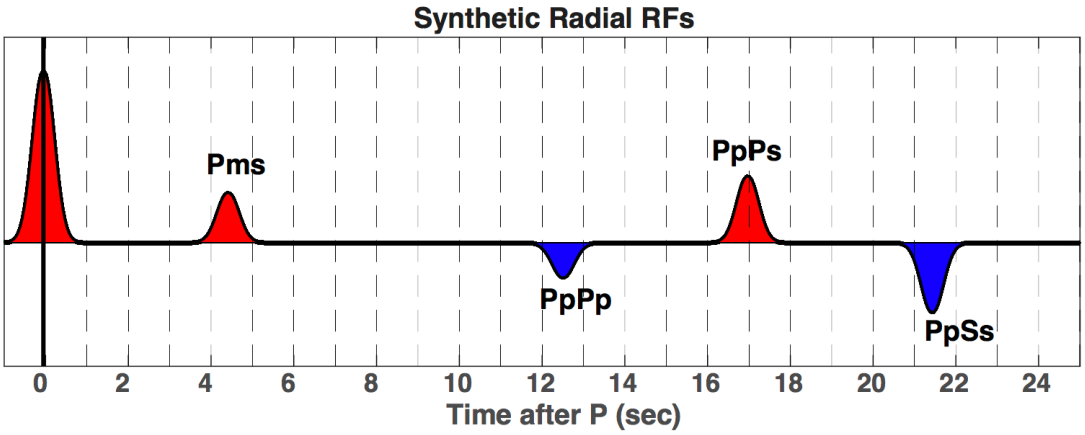

Figure A.6. Forward modeling of receiver functions using the method by Frederiksen and Bostock (2000) to examine the effect of Vp/Vs ratio on the Moho depth estimation. Both Model 1 and Model 2 above produced same receiver functions below.

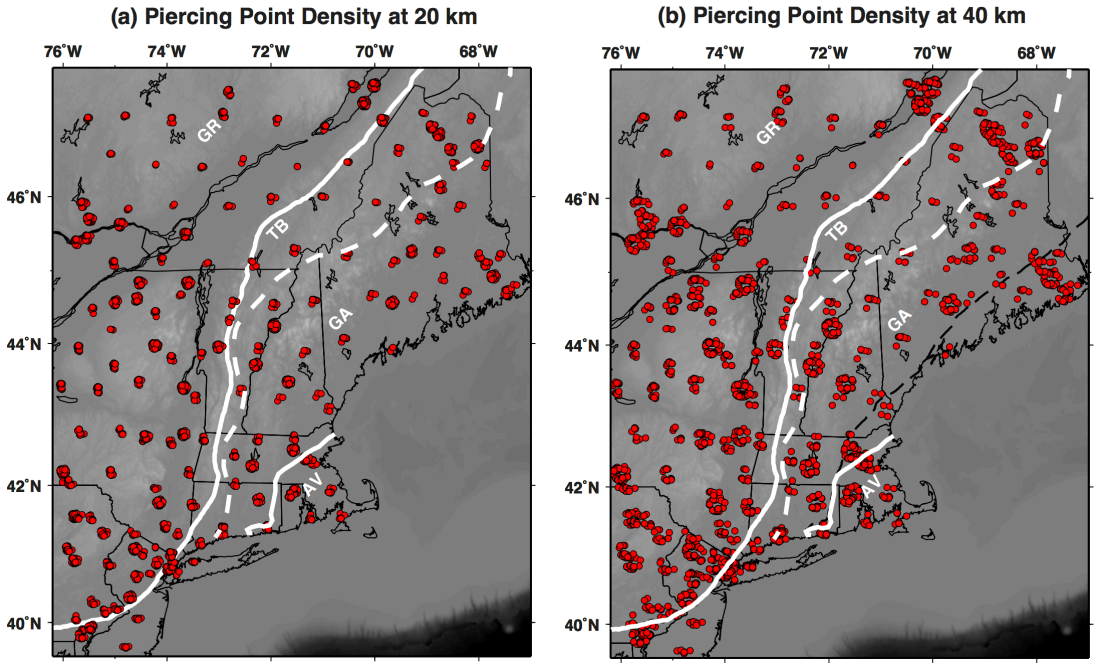

Figure A.7. Piercing point density of radial-component RFs (red dots) at depths of 20 km and 40 km, respectively, in our study region. The black solid lines mark the state boundaries and the white lines mark the interpreted tectonic units, as in Figure 2.1a.

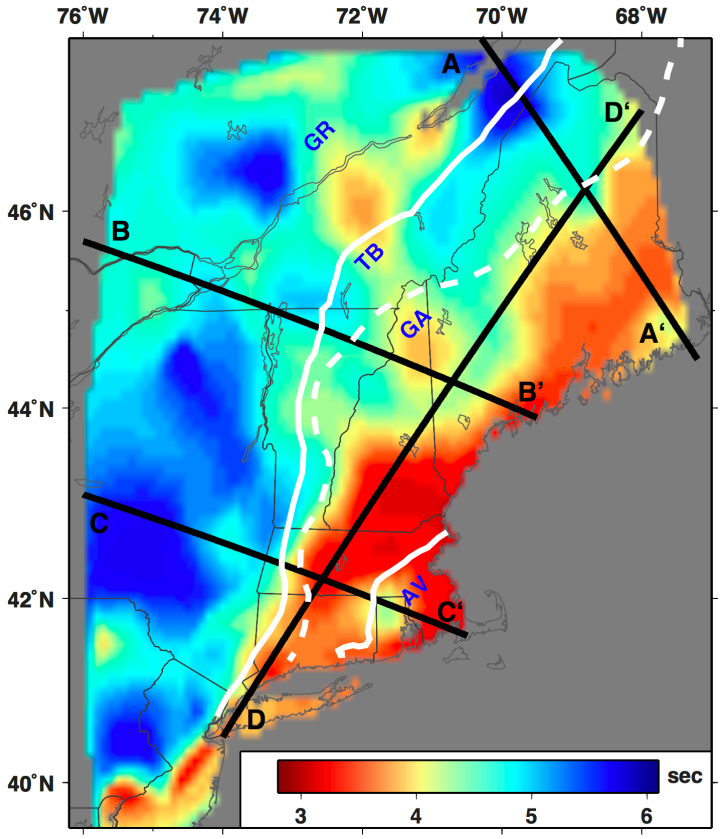

1708

1709 ***Figure A.8. Distribution of the P_ms arrival time (in seconds) interpolated in this study.***

1710 ***The thick black lines mark the profile locations in Figures 2.4 and A.9.***

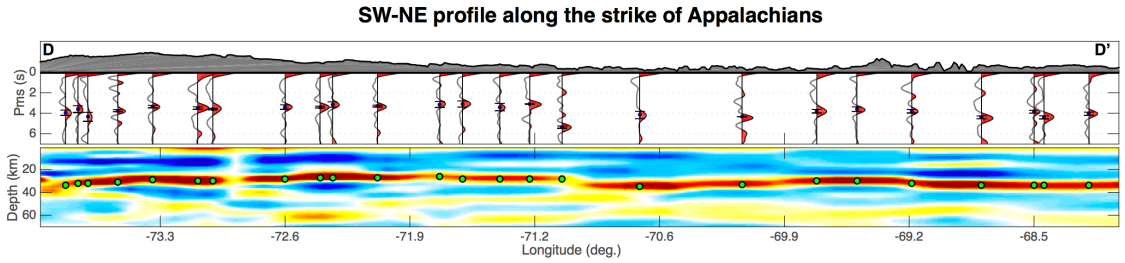

1711

1712 ***Figure A.9. The cross-section of the stacked radial-component receiver functions in the***

1713 ***time domain (upper panel) and the corresponding depth profile from the common***

1714 ***conversion point stacking (bottom panel) along the strike of the Appalachian terranes.***

1715 ***See profile location in Figure A.8.***

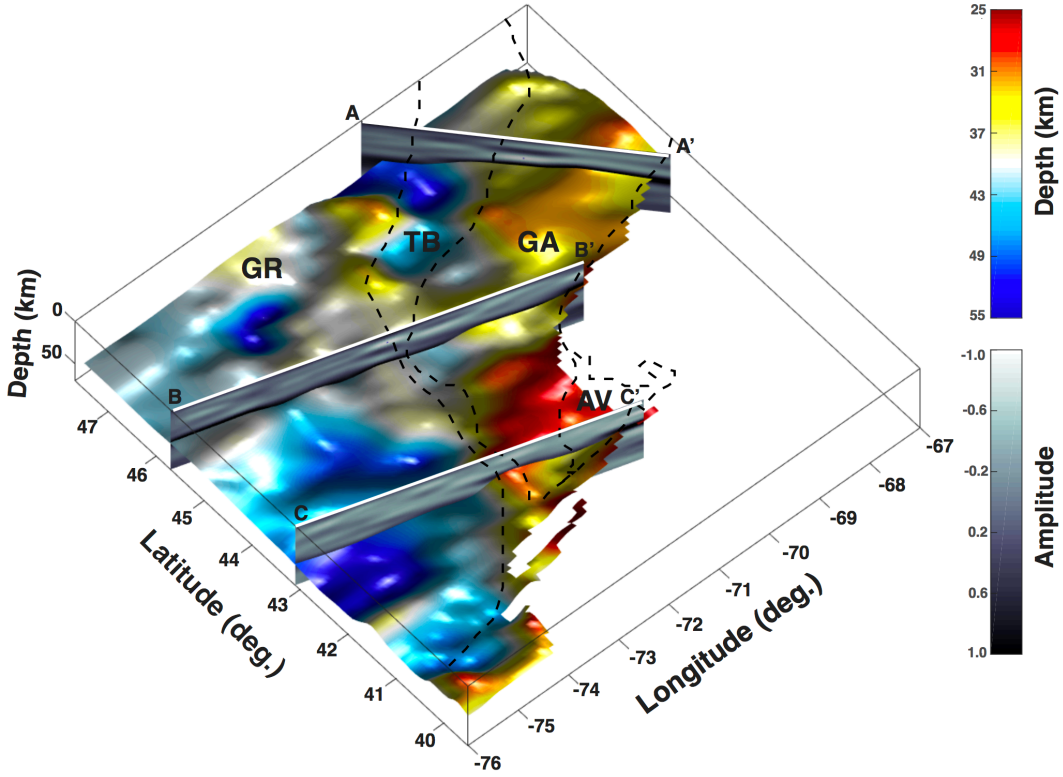

Figure A.10. Distribution of three-dimensional Moho depth variations. AA', BB', and CC' correspond to the three profiles in Figure 2.4.

Table A.1. *Auto-picked P_mS arrival time and the number of selected receiver function beneath each station for this study*

APPENDIX B

Supporting information for Chapter 3

B.1 Data

In this study, a total of 659 broadband seismic stations contributed to the dataset, including 167 permanent stations from 12 long-running seismic networks, 380 stations from the EarthScope USArray Transportable Array (TA; IRIS Transportable Array, 2003), and 112 temporary stations from 7 dense arrays. The permanent networks include the Canadian National Seismograph Network (CN; Geological Survey of Canada, 1989), the South Carolina Seismic Network (CO; Colorado Geological Survey, 2016), the CERI Southern Appalachian Seismic Network (ET; University of Memphis, CERI, 1982), the International Miscellaneous Stations (IM), the Global Seismograph Network (IU; Albuquerque Seismological Laboratory /USGS, 1988), the Kentucky Seismic and Strong Motion Network (KY; Kentucky Geological Survey/University of Kentucky, 1982), the Lamont-Doherty Cooperative Seismographic Network (LD; Lamont Doherty Earth Observatory, Columbia University, 1970), the Central and Eastern United States Network (N4; UC San Diego, 2013), the New England Seismic Network (NE; Albuquerque Seismological Laboratory /USGS, 1994), the Pennsylvania State Seismic Network (PE; Penn State University,2004), the Portable Observatories for Lithospheric Analysis and Research Investigating Seismicity (PO; Geological Survey of Canada, 2000), and the Southern Ontario Seismic Network (WU; University of Western Ontario, 1991). The temporary arrays contain stations from the Deep Structure of Three Continental Sutures in Eastern North America Network (X8; Menke et al., 2012), the Pre-Hydrofracking Regional Assessment of Central Carolina Seismicity Network (XQ; Wagner, 2012), the PASEIS

Network (XY; Penn State University, 2013), the RAMP Virginia Network (YC; Meltzer, 2011), the Eastern North American Margin Community Seismic Experiment (YO; Gaherty et al., 2014), the Appalachian Seismic Transect (Z4; Wagner, 2009), and the Southeastern Suture of the Appalachian Margin Experiment (Z9; Fischer et al., 2010).

Several networks retained some seismic sites from previously operated networks. For example, EarthScope Transportable Array seismic stations (TA) were deployed during 2013-2015. After standard deployment of two years, some stations were preserved as permanent stations for the Central and Eastern United States Network (N4). We thus merged the data of these retained stations. We migrated the data from a total of 95 stations, including 66 retained stations to the TA network from the N4 network, 22 retained stations to the PO network from the WU network, 5 retained stations to the PE network from the XY network, 1 retained station to the PO network from the CN network, and 1 retained station to the US network from the LD network.

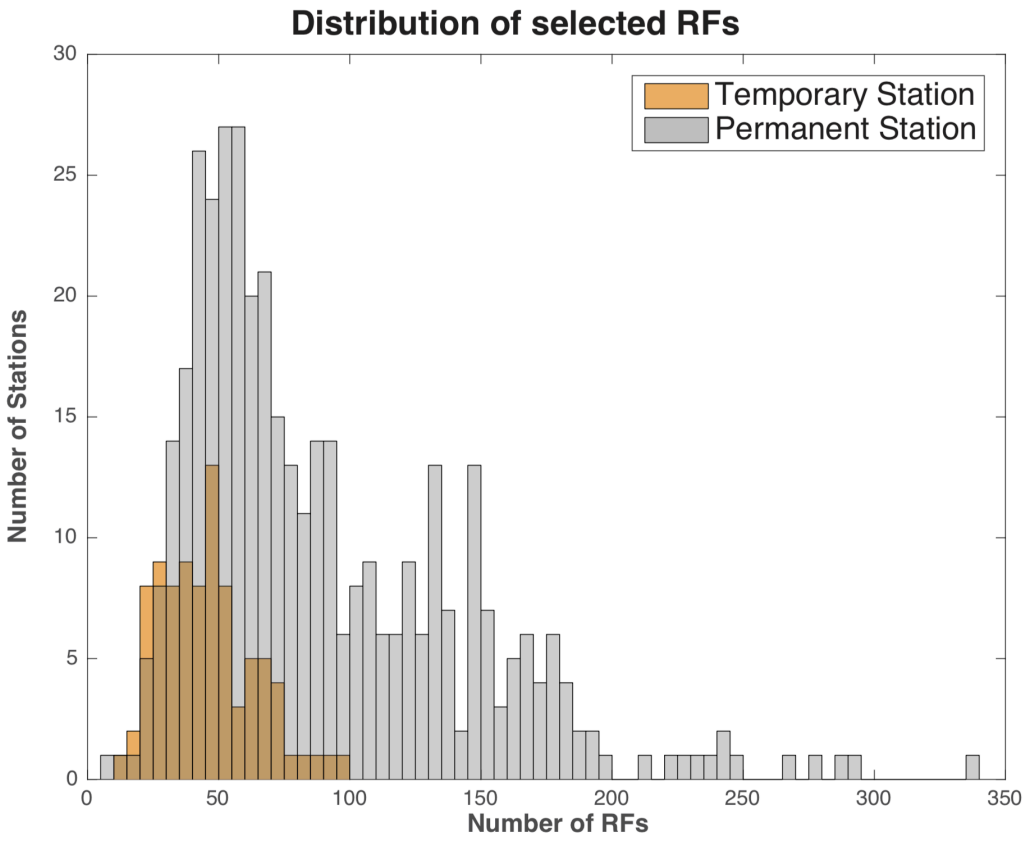

Figure B.1. Distribution of the number of selected receiver functions for permanent (gray color) and temporary stations (orange color). The bin size is 5. The horizontal axis and vertical axis are the numbers of the receiver functions and stations, respectively. See Table B.1 for a detailed description.

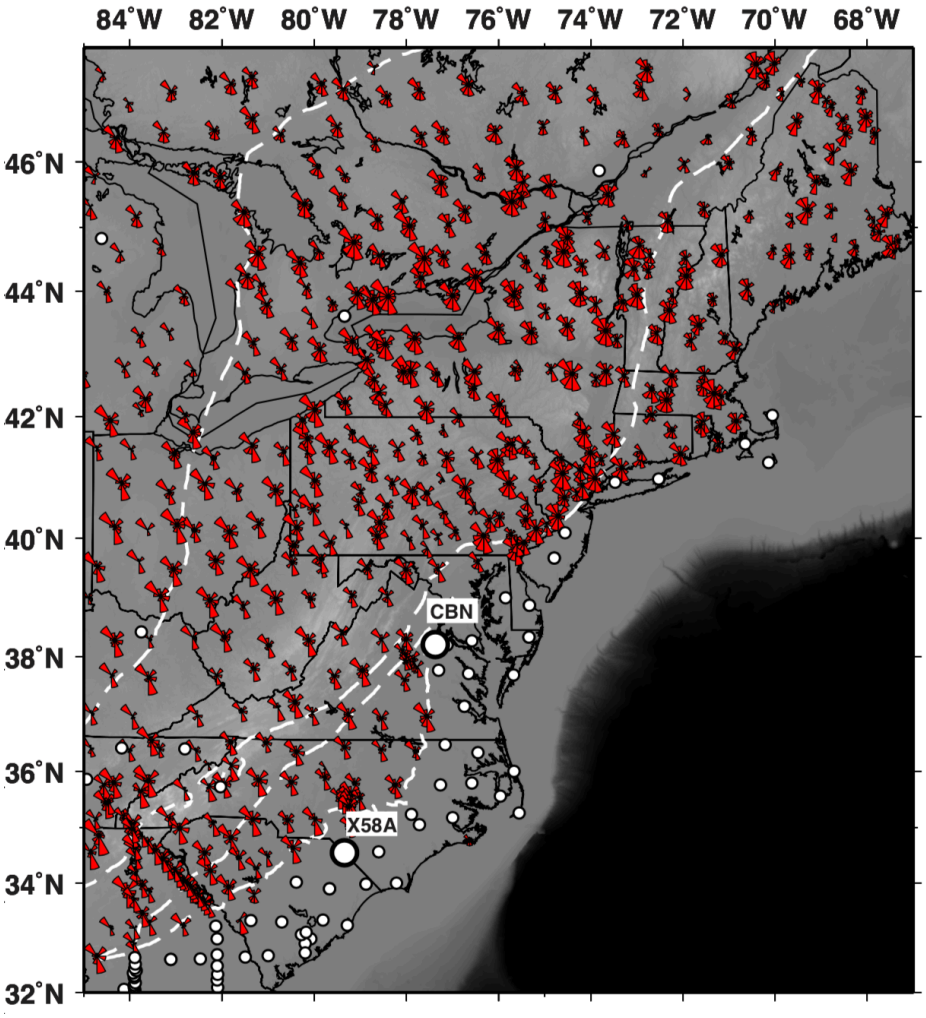

Figure B.2. The back-azimuthal coverage for collected waveforms. Wind rose diagrams mark station locations and their lengths in each bin denote the number of RFs within 30^o back azimuths.

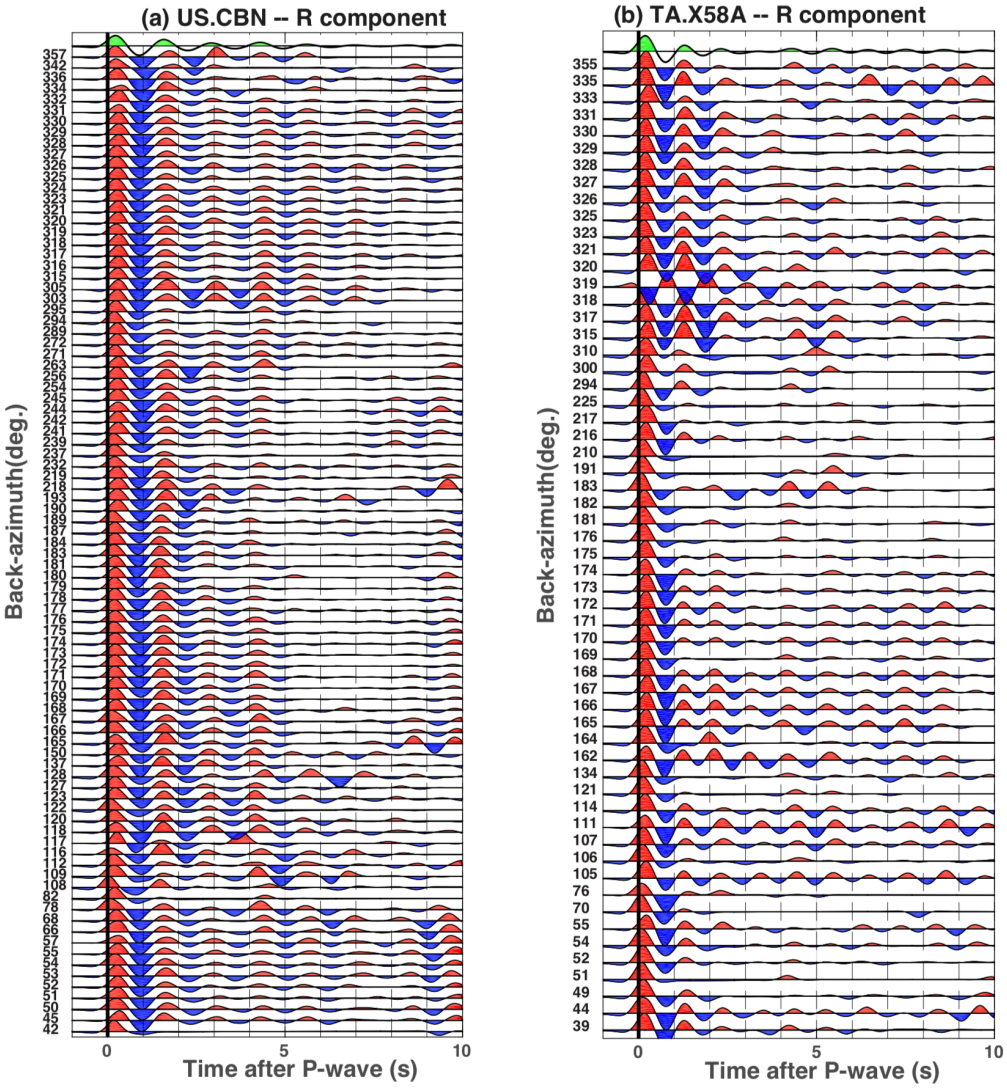

Figure B.3. Examples of strong reverberations in normalized radial-component receiver functions for stations US.CBN and TA.X58A, sorted by back azimuths. A positive phase was filled with red color while a negative was filled with blue color. The waveforms are filtered at 0.1-1.2 Hz. See station locations in Figure B.2.

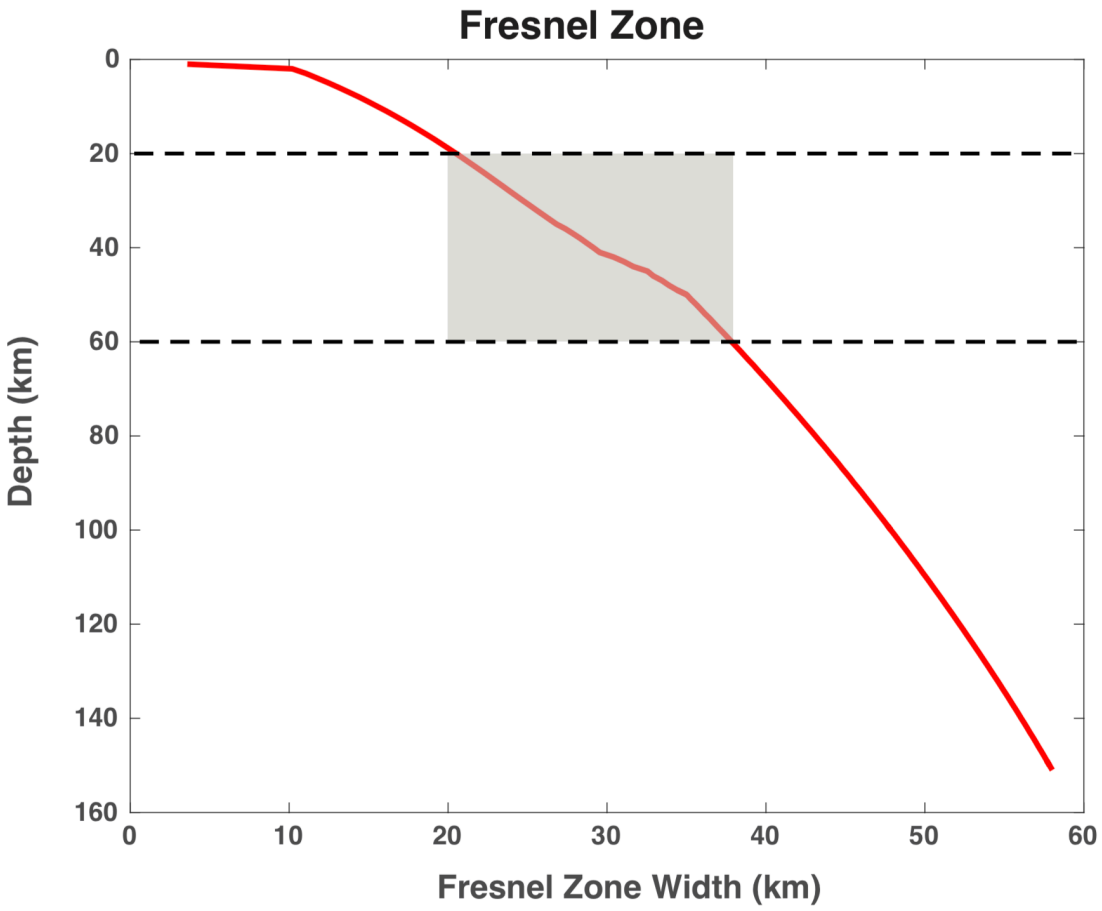

Figure B.4. Calculated Fresnel zone width versus depth. The width is about 20 km at the depth of 20 km and is about 38 km at the depth of 60 km (black dashed lines).

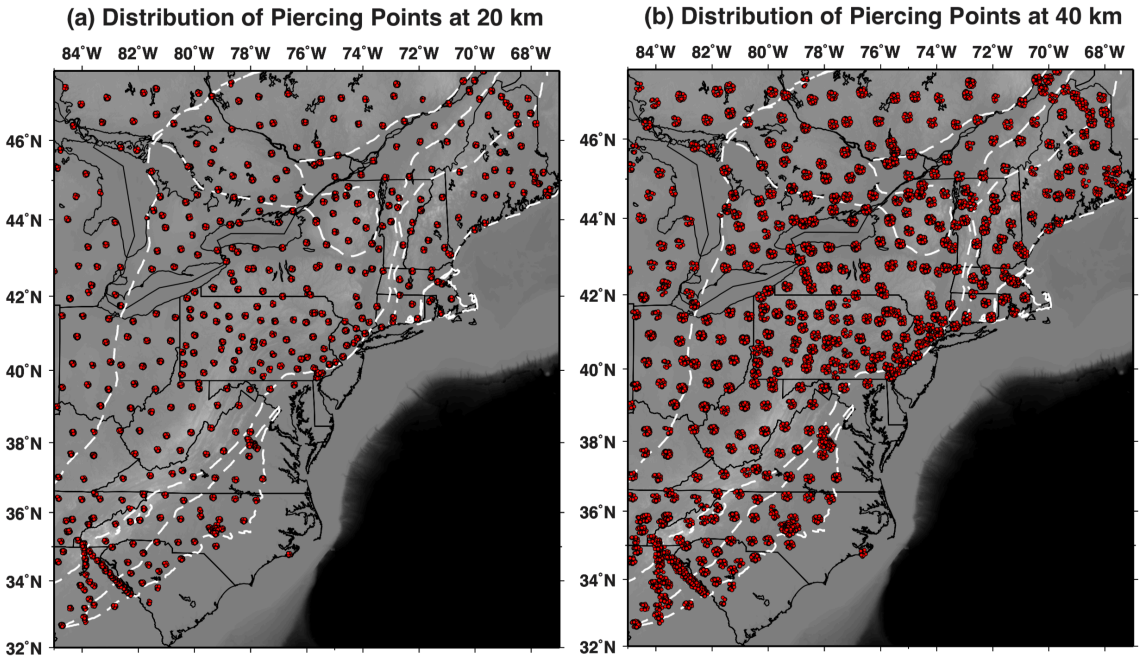

Figure B.5. Piercing point density of radial-component RFs (red dots) at depths of 20 km and 40 km, respectively, in our study region. The black solid lines mark the state boundaries and the white dashed lines mark the interpreted tectonic units, as in Figure 3.1a.

B.2 Moho depth uncertainties

The uncertainties of our extracted Moho depth mainly result from the resolution of the shear-wave velocity model used in the CCP stacking, the assumption of a constant Vp/Vs ratio, as well as possible presence of sedimentary layers. Here we examined the impact of these three factors on the Moho depth uncertainty using the ray-based RAYSUM method (Frederiken & Bostock, 2000). Other factors, such as presence of dipping interfaces and seismic anisotropies, can also contribute to the uncertainties of the Moho depth, which require a more comprehensive analysis in the future. We first defined three simple two-layer models for the uncertainty assessment. The first model was obtained by averaging

the 3-D shear-wave velocity model from Shen & Ritzwoller (2016) within our study area both horizontally and vertically. The crust was assigned values for S wave velocity, density, and Vp/Vs ratio of Vs=3.63 km/s, ρ=2.8 g/cm^3, and Vp/Vs=1.78, respectively. The mantle was assigned values of Vs=4.5 km/s, ρ=3.38 g/cm^3, and Vp/Vs=1.78, respectively (Figure B.7). We defined the second and third models by changing the crustal velocities of the first model into 3.83 km/s and 3.43 km/s, considering that the error of crustal shear velocity in reference model is ~0.2 km/s (Shen & Ritzwoller, 2016). First, given a constant Vp/Vs ratio of 1.78, our tests show that a 4.25 s P_ms arrival time corresponds to a Moho depth of 35 km, 36.9 km and 33.1 km, respectively, from these three models (Figure B.7).

Second, we note an uncertainty for our Moho depth estimation from the delay time because our estimated depths do not have same values as those revealed by the prior velocity model. For example, we overestimate the Moho depth using mantle velocity for calculation when the Moho depth is deeper than the one in the prior velocity model. In order to estimate the uncertainty, we chose two stations TA.K61A and TA.L61B (see station locations in Figure 3.4), where the sharp offset of Moho depth (45.2 km and 30 km, respectively) was observed in this study. The estimated Moho depth beneath these two stations is 43 km and 35 km, respectively, by Shen & Ritzwoller (2016). We retrieved the 1-D velocity profiles from the model by Shen & Ritzwoller (2016) at these two stations (Figure B.6), and then adjusted the velocity profiles in terms of the Moho depth. The modified velocity profiles lead to a 44.7 km Moho depth at TA.K61A and a 29.8 km Moho depth at TA.L61B (Figure B.6).

Third, previous studies demonstrated that the typical Vp/Vs ratios in the Grenville Province and the eastern margin of the old North American craton vary within a range of 1.73-1.86 (e.g., Darbyshire et al., 2017; Levin et al., 2017; Ma & Lowry, 2017; Petrescu et al., 2016), and the Vp/Vs ratios in the Appalachian region fall between 1.70 and 1.76 (e.g., Ma & Lowry, 2017; Viegas et al., 2010). Our tests with the first model revealed that for a given P_ms arrival time of 4.25 s, the crustal thickness is 37.3 km, 35.0 km, and 33.2 km, respectively, in correspondence with a Vp/Vs ratio of 1.70, 1.78, and 1.86 (Figure B.8). These three simple tests suggested that the uncertainty of the estimated Moho depth mainly results from the Vp/Vs ratio instead of the absolute shear-wave velocity.

Lastly, the presence of thick sediments delays the phase arrival time, leading to a possible overestimate of the crustal thickness (Yeck et al., 2013). We added a 2 km sedimentary layer on the first model to test the effect of sediments on the Moho depth estimate. Based on the crustal velocity model by Laske et al. (2013), the shear-wave velocity in the sedimentary layer is set as 1.94 km/s and the Vp/Vs ratio is 2.0. Our test showed a 2-km sedimentary layer can lead to a 2.2 km error in the Moho depth (Figure B.9). Additionally, a strong velocity discontinuity at the sediment-bedrock interface leads to strong reverberations, which can overlap with the P_ms phase (Figure B.10). This may be the case for 77 stations that have strong reverberations in the Atlantic coastal plain and in the Tennessee basin. We thus excluded these stations from further analysis. In contrast, we did not see strong reverberations at stations in Appalachian basin where thick sediments (~5-8 km) were suggested by previous studies (e.g., Laske et al., 2013). If the sedimentary rock is consolidated or has a relatively higher velocity, the corresponding multiples can be

separated from the P_ms phase (Figure B.10), which may be the case beneath the Appalachian basin.

Our simple tests demonstrate that we may expect a total of ~±6 km uncertainty for the estimated Moho depth in our study region, which should not change the general distribution pattern of the crustal thickness as well as possible interpretations.

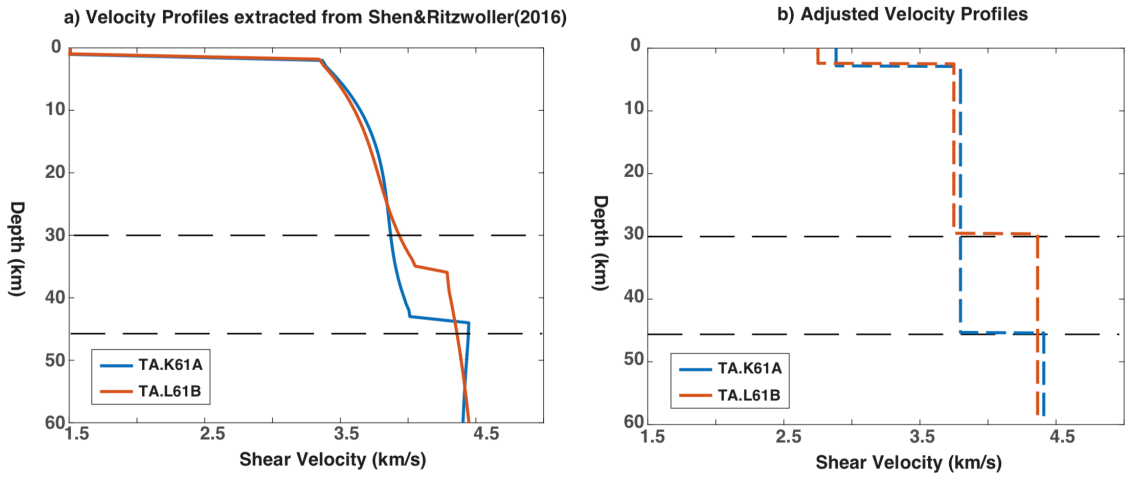

Figure B.6. (a) The velocity profiles at stations TA.K61A and TA.L61B extracted from the model by Shen & Ritzwoller (2016). The black dashed lines mark the Moho depths estimated in this study. (b) We simplified the velocity profiles in (a), and adjusted the velocity values near the estimated Moho in order to investigate the uncertainty on Moho depth due to the velocity variation near the true Moho.

H= 35 km; Vs= 3.63 km/s Vp/Vs=1.78; Rho=2.80 g/cm^3
H= ~ km; Vs= 4.5 km/s Vp/Vs=1.78; Rho= 3.38 g/cm^3

H= 36.9 km; Vs= 3.83 km/s Vp/Vs=1.78; Rho=2.80 g/cm^3
H= ~ km; Vs= 4.5 km/s Vp/Vs=1.78; Rho= 3.38 g/cm^3

H= 33.1 km; Vs= 3.43 km/s Vp/Vs=1.78; Rho=2.80 g/cm^3
H= ~ km; Vs= 4.5 km/s Vp/Vs=1.78; Rho= 3.38 g/cm^3

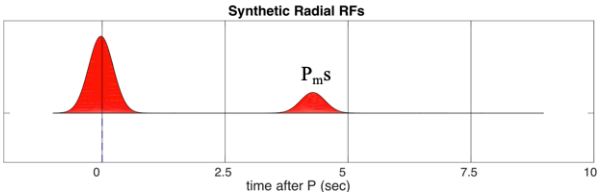

P_mS= 4.25 s

Figure B.7. Forward modeling of receiver functions using the method by Frederiksen and Bostock (2000) to examine the effect of different velocity models.

H= 35 km; Vs= 3.63 km/s Vp/Vs=1.78; Rho=2.80 g/cm^3
H= ~ km; Vp= 4.50 km/s Vp/Vs=1.78; Rho= 3.38 g/cm^3

H= 37.3 km; Vs= 3.63 km/s Vp/Vs=1.70; Rho=2.80 g/cm^3
H= ~ km; Vs= 4.50 km/s Vp/Vs=1.70; Rho= 3.38 g/cm^3

H= 33.2 km; Vs= 3.63 km/s Vp/Vs=1.86; Rho=2.80 g/cm^3
H= ~ km; Vs= 4.50 km/s Vp/Vs=1.86; Rho= 3.38 g/cm^3

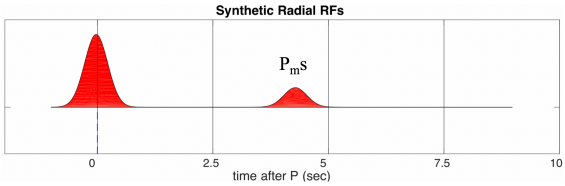

P_mS= 4.25 s

Figure B.8. Forward modeling of receiver functions to examine the impact of the Vp/Vs on the Moho depth estimation.

H= 35 km; Vs= 3.63 km/s Vp/Vs=1.78; Rho=2.80 g/cm^3
H= ~ km; Vs= 4.5 km/s Vp/Vs=1.78; Rho= 3.38 g/cm^3

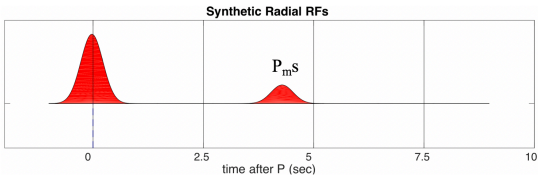

P_mS= 4.25 s

Moho =35 km

H= 2 km; Vs= 1.94 km/s Vp/Vs=2.0; Rho=2.35 g/cm^3
H= 30.8 km; Vs= 3.63 km/s Vp/Vs=1.78; Rho=2.80 g/cm^3
H= ~ km; Vs= 4.5 km/s Vp/Vs=1.78; Rho= 3.38 g/cm^3

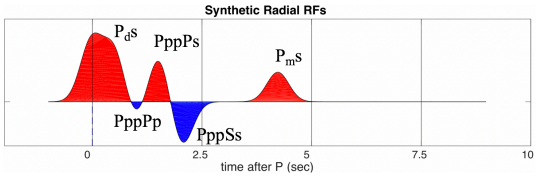

P_mS= 4.25 s

Moho=32.8 km

1864

1865 ***Figure B.9. Forward modeling of receiver functions to examine the effect of the***

1866 ***sedimentary layers on the Moho depth estimation.***

1867

H=5 km; Vs=1.94 km/s Vp/Vs =1.85; Rho=2.35 g/cm^3
H=30 km; Vs=3.63 km/s Vp/Vs =1.78; Rho=2.80 g/cm^3
H=~ km; Vs=4.5 km/s Vp/Vs =1.78; Rho=3.38 g/cm^3

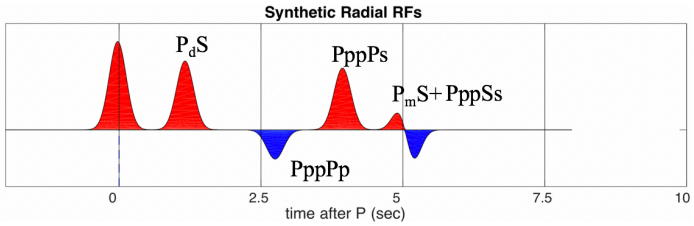

H=5 km; Vs=2.80 km/s Vp/Vs =1.85; Rho=2.35 g/cm^3
H=30 km; Vs=3.63 km/s Vp/Vs =1.78; Rho=2.80 g/cm^3
H=~ km; Vs=4.5 km/s Vp/Vs =1.78; Rho=3.38 g/cm^3

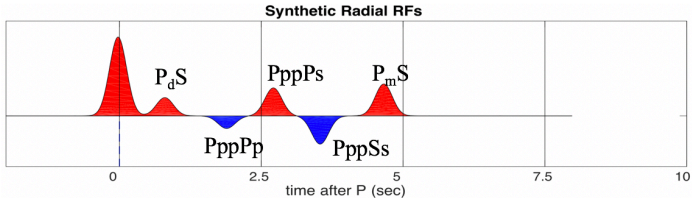

1868

1869 ***Figure B.10. Forward modeling of receiver functions to examine the reverberations***

1870 ***generated by the sediment-bedrock interfaces.***

Anisotropic Model

H= 17.5 km; Vs=3.6 km/s; Vp/Vs=1.78; Rho=2.80 g/cm^3
H= 9 km; Vs=3.8 km/s; Vp/Vs=1.78; Rho=2.80 g/cm^3; Ani_P(S)=10%; PlungeAngle=20°
H= 21 km; Vs=3.8 km/s Vp/Vs=1.78; Rho=2.80 g/cm^3
H= ~ km; Vs=4.5 km/s Vp/Vs=1.78; Rho=3.38 g/cm^3

Isotropic Model

H= 17.5 km; Vs=3.6 km/s; Vp/Vs=1.78; Rho=2.80 g/cm^3
H= 7 km; Vs=4.2 km/s; Vp/Vs=1.78; Rho=2.80 g/cm^3
H= 23 km; Vs=3.8 km/s; Vp/Vs=1.78; Rho=2.80 g/cm^3
H= ~ km; Vs=4.5 km/s; Vp/Vs=1.78; Rho=3.38 g/cm^3

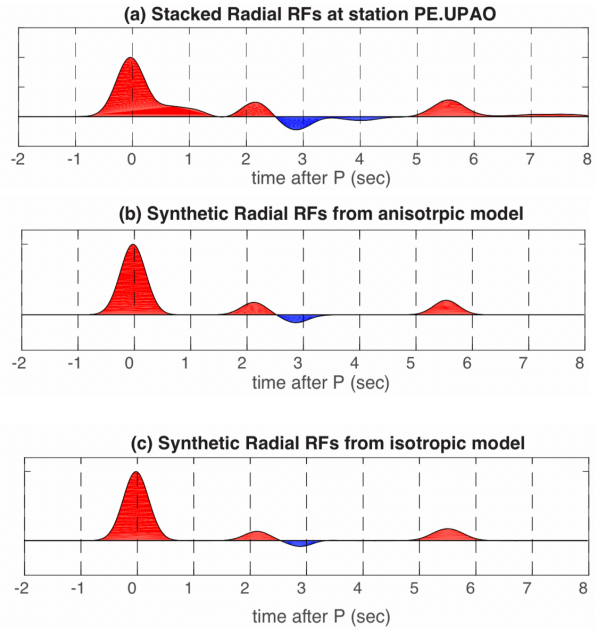

Figure B.11. Synthetic receiver functions at station PE.UPAO in order to explore the possibilities of the observed positive and negative phases within 2-3 seconds. (a) Stacked radial receiver function at station PE.UPAO. (b) Synthetic radial receiver function from anisotropic model (c) Synthetic radial receiver function from isotropic model. See the station location in Figure 3.6.

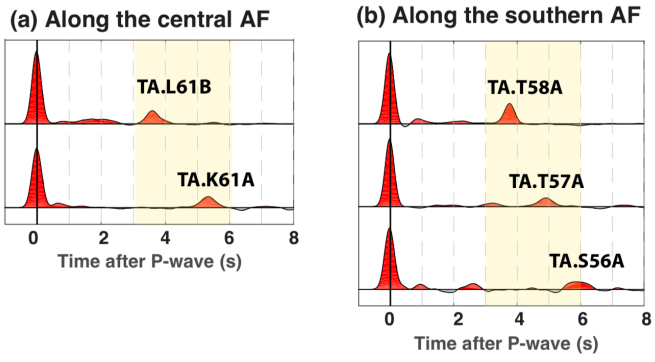

Figure B.12. Representative radial-component RFs to demonstrate variations of P_ms arrival times in eastern North America. For each station, the RFs are stacked from all the back-azimuthal directions. The waveforms are low-pass filtered at 2.4 Hz. The

1882 ***shaded yellow window highlights the difference in the P_ms arrival times. The locations***

1883 ***of stations are marked in Figure 3.4a.***

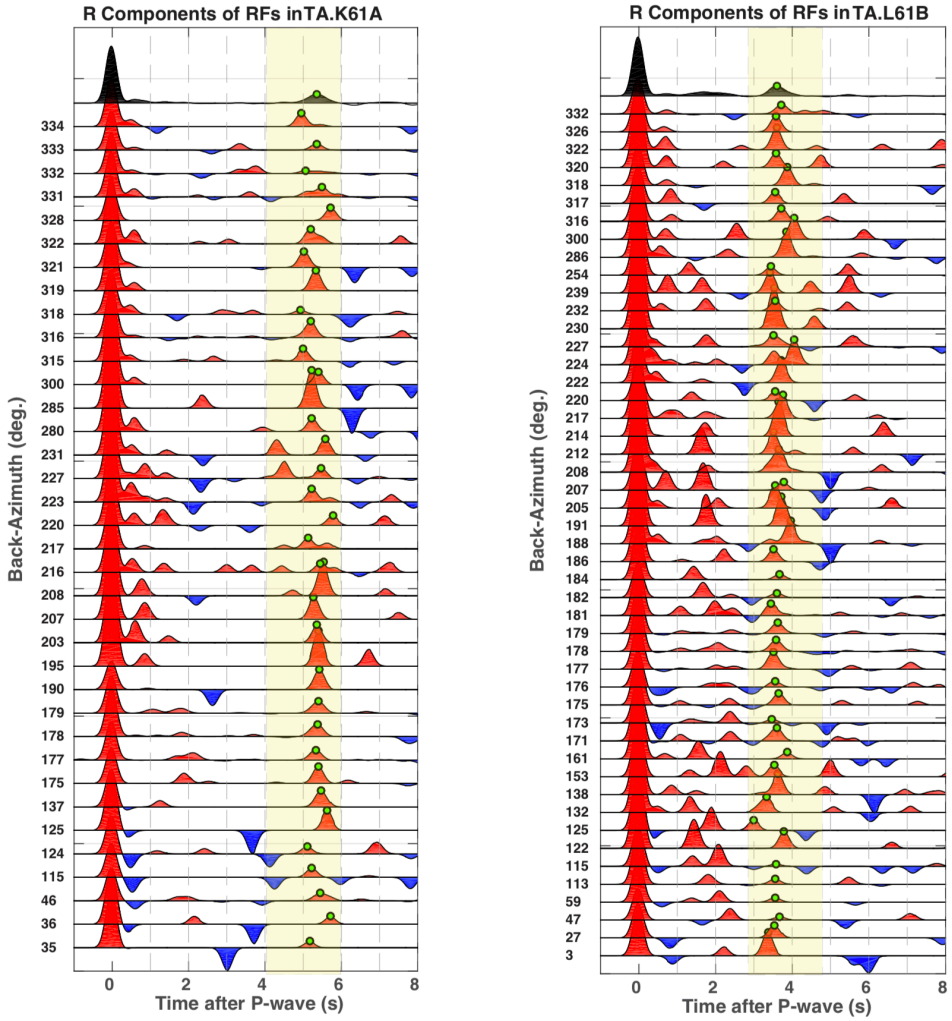

1884

1885 ***Figure B.13. Examples of the significant increase of P_ms arrivals in normalized radial-***

1886 ***component receiver functions for stations TA.K61A and TA.L61B, sorted by back***

1887 ***azimuths. The waveforms are filtered by a Gaussian filter with the parameter of 5 (~0-***

1888 ***2.4 Hz). See station locations in Figure 3.4.***

1889

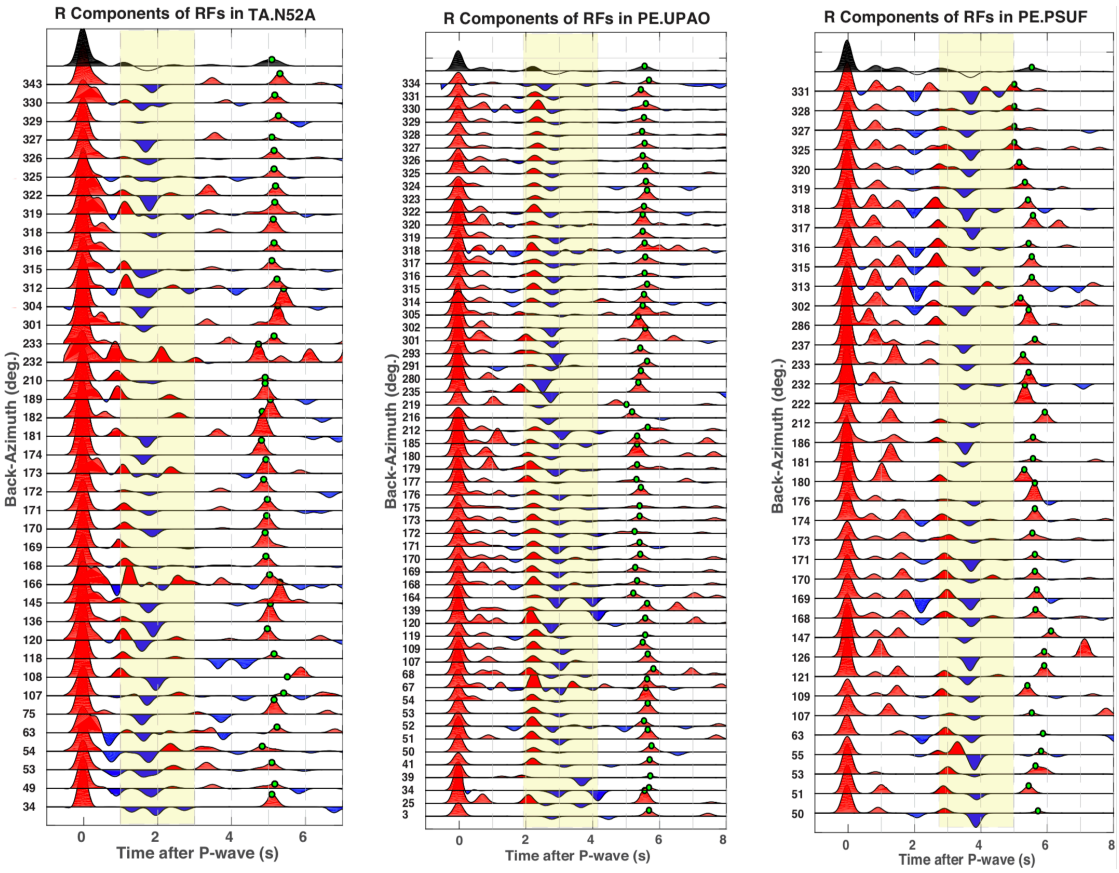

Figure B.14. Examples of strong intra-crustal negative signals in normalized radial-component receiver functions for stations TA.N52A, PE.UPAO and PE.PSUF, sorted by back azimuths. A positive phase was filled with red color while a negative was filled with blue color. The waveforms are filtered by a Gaussian filter with the parameter of 5 (~0-2.4 Hz). See station locations in Figure 3.7.

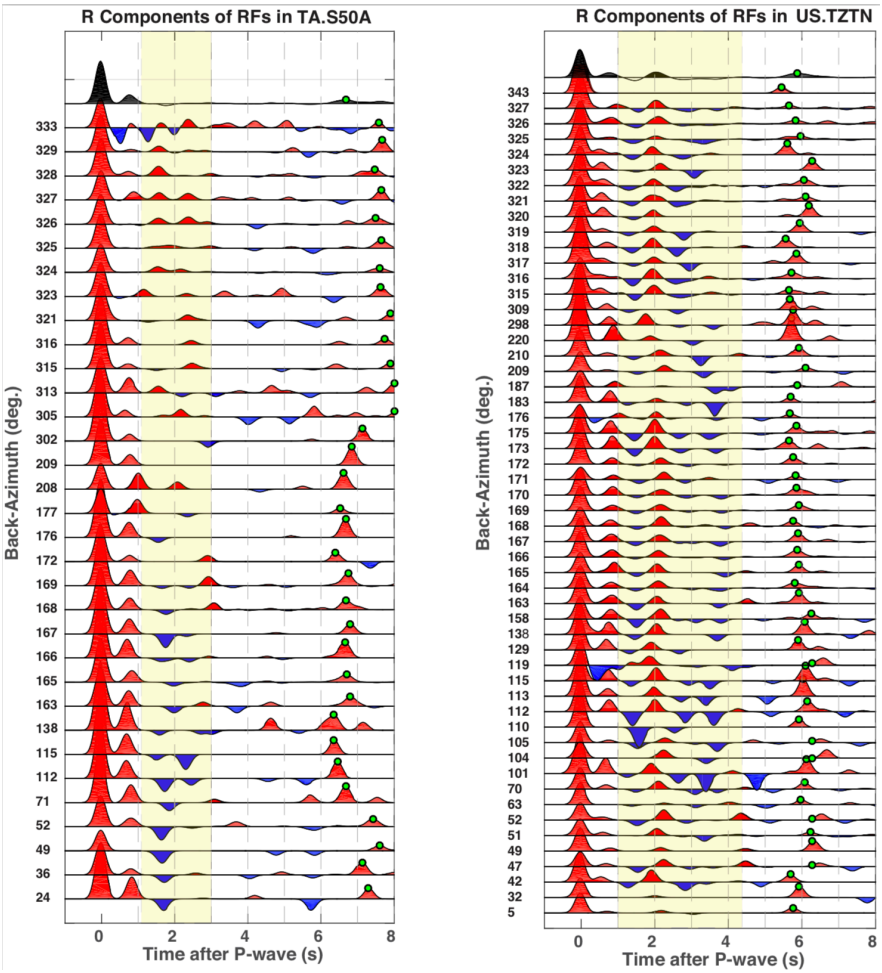

Figure B.15. Examples of complex intra-crustal negative signals in normalized radial-component receiver functions for stations TA.S50A and US.TZTN, sorted by back azimuths. See station locations in Figure 3.4.

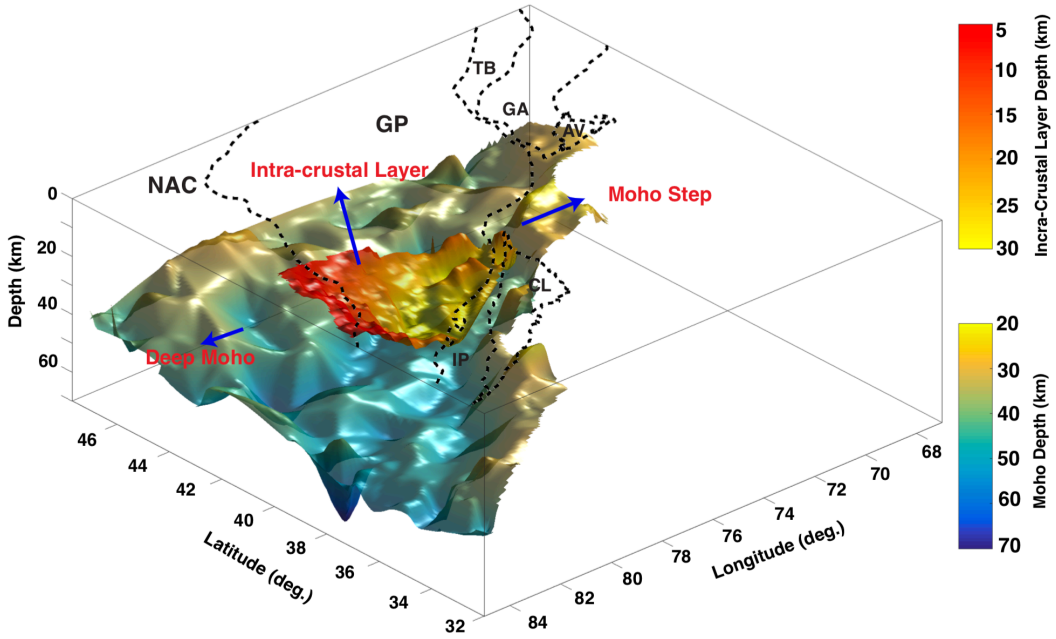

1902

1903 ***Figure B.16. Three-dimensional distribution of the Moho depth beneath eastern North***

1904 ***America and the intra-crustal layer beneath the central Grenville Province. The dashed***

1905 ***lines are the geologically-defined surface boundaries between two tectonic units. The***

1906 ***abbreviations of the tectonic units are the same as in Figure 3.7.***

1907

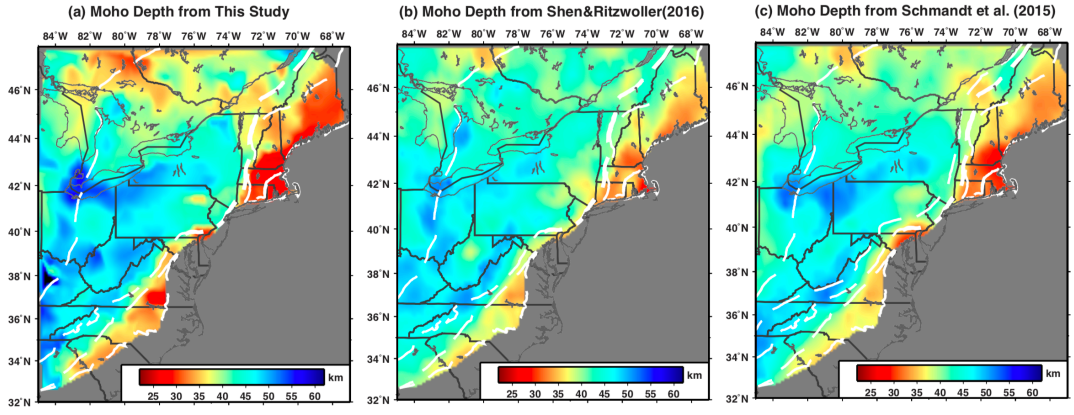

1908

1909 ***Figure B.17. The comparison of Moho depth distribution from (a) this study, (b) Shen***

1910 ***& Ritzwoller (2016), and (c) Schmandt et al. (2015).***

1911

Appendix B

Table B.1. *The number of selected Receiver functions in each station, the mean P_ms arrival times automatically picked from the stacked radial-component receiver functions for each seismic station, and the uncertainty of the P_ms arrival times of all individual events at each station. See the description about the mean values and the uncertainties of P_ms arrival time in Methodology part.*

APPENDIX C

Supporting information for Chapter 4

C.1 Data

In this study, a total of 275 broadband seismic stations contributed to the dataset, including 172 permanent stations from 12 long-running seismic networks and 103 temporary stations from 7 dense arrays. The long-running seismic networks include the South Carolina Seismic Network (CO; University of South Carolina, 1987), the CERI Southern Appalachian Seismic Network (ET; University of Memphis, CERI, 1982), the U.S. Geological Survey Network (GS; Albuquerque Seismological Laboratory/USGS, 1980), the Lamont-Doherty Cooperative Seismographic Network (LD; Lamont Doherty Earth Observatory, Columbia University, 1970), the Central and Eastern U.S. Network (N4; University of California San Diego, 2013), the Cooperative New Madrid Seismic Network (NM; Saint Louis University, 1980), the NetQuakes Network (NQ; U.S. Geological Survey, 1989), the Southeastern Appalachian Cooperative Seismic Network (SE), the South Carolina Earth Physics Project (SP; University of South Carolina, 2000), the Single Station Network (SS), the EarthScope U.S. Transportable Array (TA; IRIS Transportable Array, 2003), and the United States National Seismic Network (US; Albuquerque Seismological Laboratory/USGS, 1990). The temporary arrays contain stations from the Central Virginia and South Carolina Seismic Monitoring Experiment (5H; Martin Chapman, 2017), the Mid-Atlantic Geophysical Integrative Collaboration Network (7A; Long & Wiita, 2013), the Pre-Hydrofracking Regional Assessment of Central Carolina Seismicity Network (XQ; Wagner, 2012), the RAMP Virginia Network (YC; Meltzer,

2011), the Eastern North American Community Seismic Experiment (YO; Gaherty et al., 2014), and the Appalachian Seismic Transect (Z4; Wagner, 2009).

C.2 Methodology

C.2.1 The Empirical Green's Functions

The empirical Green's functions (EGFs) were retrieved from the cross-correlation of processed waveforms between each station pairs. We first removed the instrument response of from the raw data, cut the continuous waveforms into one-day length and normalized the daily waveforms. In order to minimize the impacts of uneven-distributed large earthquakes on the EGFs reconstruction (Yao et al., 2009), we zeroed the amplitude of the time segments that recorded large earthquakes (Mw > 5.5). We then calculated the cross-correlation of processed daily waveforms between each station pairs in our study region. Finally, the daily cross-correlated data were stacked, and the negative time derivatives of stacked cross-correlation were taken as the EGFs. In addition, we obtained the monthly stacks of cross-correlations, whose variation provides the estimation of uncertainty of EGFs reconstruction.

The EGFs show clear Rayleigh wave signals on both positive and negative time lags at periods of 5-150 s between land-land station pairs and at periods of 8-50 s for land-ocean and ocean-ocean station pairs (see examples in Figure 4.2). The signals of positive portion represent for Rayleigh waves generated by the virtual sources and recorded by other receivers, while the signals of negative portion show for Rayleigh waves propagated in an opposite direction. In order to illustrate the data quality, we calculated signal-to-noise ratios

(SNR) for the EGFs on both positive and negative time segments between each station pairs (see examples in Figure C.1). We defined the SNR as the ratio of maximum amplitude of EGFs to the standard deviation of monthly stacks of cross-correlations. The SNR of EGFs varies in a range of 5-40 dB for land-land station pairs and in a range of 2-10 dB for land-ocean and ocean-ocean station pairs (see examples in Figure C.1). In order to better measure Rayleigh-wave phase delays between the observed EGFs and the synthetics, we required a minimum signal-to-noise ratio of the observed EGFs on both positive and negative time segments to be 6 for land-land pairs and 4 for land-ocean and ocean-ocean station pairs, respectively.

C.2.2 Inversion of velocity perturbations

The perturbations of P wave and S wave velocity were inferred from the following equation:

$$dt_{ij} = \int_V [K_\alpha(s_i, r_i; T_j; x)\, \delta\alpha + K_\beta(s_i, r_i; T_j; x)\delta\beta]dx^3$$

where dt_{ij} is the measured phase delay, K_α and K_β are the Rayleigh wave sensitivity kernels for Vp and Vs, and $\delta\alpha$ and $\delta\beta$ represent the perturbations of Vp and Vs, respectively. We carried out the inversion using the conjugate gradient method with a variety of smoothing and damping factors. The preferred model was chosen by minimizing model norm and data misfit. The data misfit (or Chai square) is defined as

$$\text{Misfit} = \left(\sum dt\right)^2 /\text{N}$$

Where dt is the phase delay time between the observed and synthetic waveforms, and N is the number of measurements. The reference model was then updated iteratively by adding the velocity perturbations during each iteration. After 5 iterations of inversion, both model norm and data misfit decrease significantly (Figure C.2). We notice that the Chai square deceases into 1.35 at the 5th iteration (Figure C.2a), suggesting the misfit is independent and Gaussian distributed. We also see a small variance reduction after 5 iterations (Figure C.2b). Those observations suggest our model is nearly stable after 5 iterations of inversion.

C.3. The impact of reference model on the tomographic results

Our final model shows a variety of interesting features within the crust and upper mantle. A key question is that to what extent those observed features in our final model depend on the reference model. In order to answer this question, we make a comparison between our final model and the reference model with different lateral slices and vertical profiles (see Figures 4.3, C.7-C.9).

Several similar features can be seen in both the reference model and our final model. For example, both models show high P-wave velocity beneath West Virginia and southeastern Georgia and low P-wave velocity in the oceanic part at 7 km depth (Figures C.7a and C.8a). We also see a lateral variation of S-wave velocity from the oceanic to the continental part at shallow depths in both models (Figures C.7b, C.7c, C.8b and C.8c). However, our final model highlights these observed features in comparison with the reference model. For example, the final model has a tighter constraint on the distribution of low S-wave velocity (<=3.5 km/s) in the oceanic part, and has larger velocity in the continental part comparing

with the reference model (Figure C.9). As a result, the lateral variation of S-wave velocity across the ocean-continent margin can be seen more clearly in our final model. In addition, the slow-to-fast S-velocity change from offshore to onshore in our final model matches the Moho depth variation better comparing with the reference model, emphasizing geometry of oceanic-continental transitional crust (Figure C.9). More importantly, our final model shows two low velocity anomalies within the upper mantle beneath the transitional crust and West Virginia volcanoes that have not been observed in the reference model (Figure C.8d-C.8f, C.9). These observations suggest that our final tomographic imaging does not strongly depend on the selection of the reference model and that our final model can provide better constraints on the crustal and upper mantle structure beneath the southern ENAM.

C.4. Uncertainty of velocity model

The uncertainties of our final model mainly result from the estimation of P-wave velocity reference model using a constant Vp/Vs ratio as well as the ignorance of topography above the sea level. Here we discuss the impact of these two factors on the uncertainty of our tomographic imaging.

First, the crustal P-wave velocity in the reference model is converted from the S-wave velocity by assuming a constant Vp/Vs ratio of 1.76. Previous studies have demonstrated that the typical Vp/Vs ratios within crust in our study region vary within a range of 1.73-1.78 (e.g., Ma & Lowry, 2017). Our assumption of constant Vp/Vs ratio therefore would cause uncertainties in the P-wave tomographic results, especially within the upper crust

where the P-wave velocity is most sensitive. In order to estimate the effect of this uncertainty on our result, we compare the average P-wave velocity of upper crust between the P-wave reference model, our final model and the velocity model from Tesauro et al.,2014 (Figure C.11). We observe that the average P-wave velocity values from the model of Tesauro et al.,2014 are clearly larger than the velocities from the reference model and our final result. For example, the P-wave velocity value beneath southern West Virginia is ~6.2 km/s in the model of Tesauro et al.,2014. In contrast, the velocities are ~6.0 km/s in the reference model and ~5.8 km/s in our final model, respectively. We also see the velocity along the margin in the model of Tesauro et al.,2014 is ~0.5 km/s larger comparing with the reference model and our final result. However, we see a similar west-east variation of P-wave velocity within the upper crust in general, although local-scale features are different between those three models. For example, we observe a general decrease of P-wave velocity from the continental interior, through the margin, to the oceanic part. This simple comparison suggests that the uncertainty of P-wave velocity estimation due to the assumption of constant Vp/Vs ratio will not strongly impact on the pattern of velocity variation as well as the geometry of observed features in our main text.

Second, we have ignored the elevation of reference model above sea level when we simulated wave propagation. This ignorance of topography variation would cause uncertainty of our tomographic imaging. Previous studies have demonstrated that the topography variation will mainly change the sensitively kernels of Rayleigh waves in short periods of ~3-5s, and the shallow subsurface structure at ~2-3 km depth will be impacted for ignoring every 1 km elevation (e.g., Wang et al., 2017). The elevation in our study

region varies within ~1-2 km and the influenced depth of subsurface structure due to topography is thus estimated as ~2-6 km. Considering that we mainly focus on the structures within the lower crust and upper mantle in this project, the ignorance of topography above sea level will not impact on our major observations and interpretation.

C.5. Resolution Tests

The full-wave ambient noise tomographic imaging demonstrates distinct variation patterns of seismic velocities from the uppermost crust down to the mantle lithosphere within our study area (Figures 4.3 and 4.4). We conduct a series of resolution tests in order to assess the lateral and vertical resolutions of the seismic observations (Figures C.13-C.20).

We first ran a variety of checkerboard resolution tests for P-wave velocity (Figures C.13-C.15) and S-wave velocity (Figures C.16-C.18), respectively, with horizontal dimensions of 50 km, 75 km, and 100 km. Our tests show that P-wave velocities can be better resolved than S-wave velocities at depths shallower than 17 km (Figures C.13- C.15). The minimum lateral scale of resolvable structures in P-wave model is ~50 km for the continental part and ~75 km for the oceanic part (Figures C.13 and C.14). At depths greater than 17 km, the S-wave velocity model has better resolutions. For the continental part, the lateral scales of resolvable structures are on the order of ~50 km at shallower depths (<=30 km) (Figure C.16) and increase to ~100 km at greater depths (Figure C.18). For the oceanic part, the S-wave velocity model can resolve structures with a lateral scale of ~75 km within a depth range of 17-60 km (Figure C.17). The oceanic mantle lithosphere at depths deeper than 60

km cannot be well resolved, which reflects the insufficient data coverage on the oceanic part at longer periods (Figures C.3h, C.3i, C.4h and C.4i).

We then conducted two model recovery tests to further validate the scale and geometry of observed key features in our model. The first model is to check our ability to resolve the lateral variation of crustal thickness (Figure C.19). Based on our tomographic results (Figures 4.3 and 4.4), we set the crustal thickness of 13 km for the oceanic part and 35 km for the continental part, with a linear thickening over a horizontal distance of 70 km from ocean to continent (Figures C.19a and C.19b). The velocity perturbation is set as -10% within the crust and +10% for the mantle lithosphere. The recovery tests demonstrate that our full-wave tomography is capable of resolving a crustal thickness variation from ocean to continent (Figures C.19c). However, the amplitude of the input velocity perturbation cannot be fully recovered at the shallow depths (<5 km for the continental part and <15 km for the oceanic part) (Figures C.19c).

We also validate the geometries of observed low-velocity column beneath the continental interior and the low-velocity mantle lithosphere beneath ocean-continent transitional crust (Figures C.20a-C.20c). We set the velocity perturbations and geometry for these two anomalies based on our tomographic results (Figures 4.3 and 4.4). The key geometry and scale for both low-velocity anomalies can be clearly recovered (Figures C.20d-C.20f), though we cannot fully recover the amplitude of the input velocity perturbations. Note that the recovered model is obtained by a single iteration of inversion. A non-linear inversion with multiple iterations will therefore improve the reconstruction of velocity model.

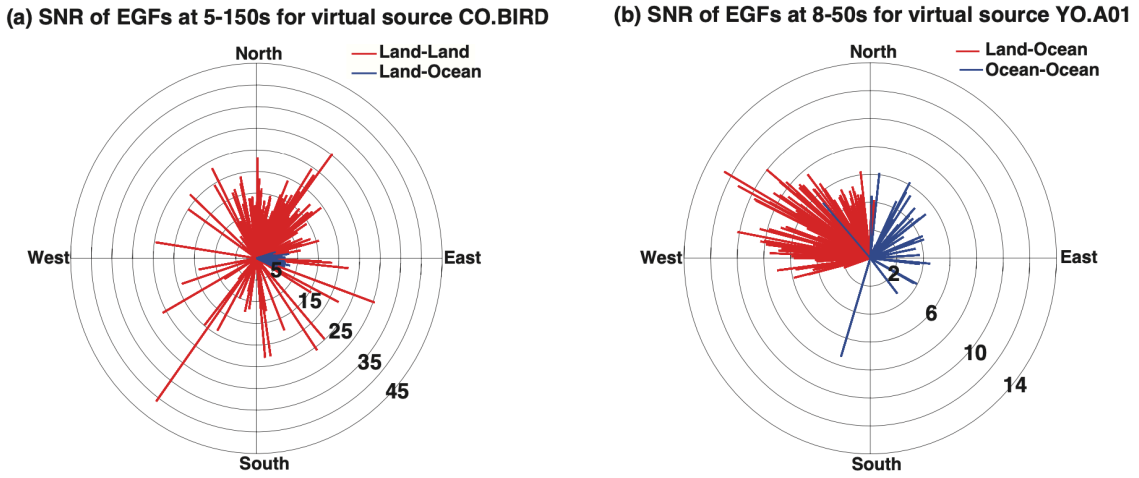

Figure C.1. Examples of average signal-to-noise ratios for empirical Green's functions (EGFs) on both positive and negative time segments from the virtual sources CO.BIRD (a) and YO.A01 (b) to the receivers. The red lines mark the signal-to-noise ratios of EGFs between land-land station pairs and the blue lines mark the signal-to-noise ratios of EGFs between land-ocean or ocean-ocean station pairs. The length of lines shows the magnitude of signal-to-noise ratio and the direction of lines marks the azimuthal angle.

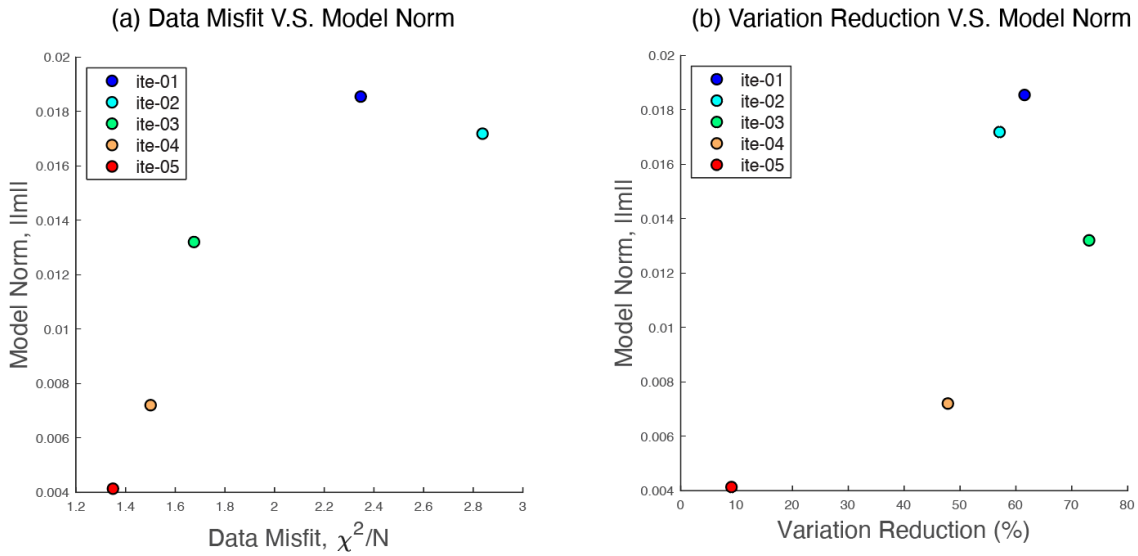

Figure C. 2. (a) Distribution of data misfit versus the model norm after each inversion for a damping factor of 8 and a smoothing factor of 8. (b) Distribution of data variance reduction versus the model norm after each inversion for a damping factor of 8 and a smoothing factor of 8.

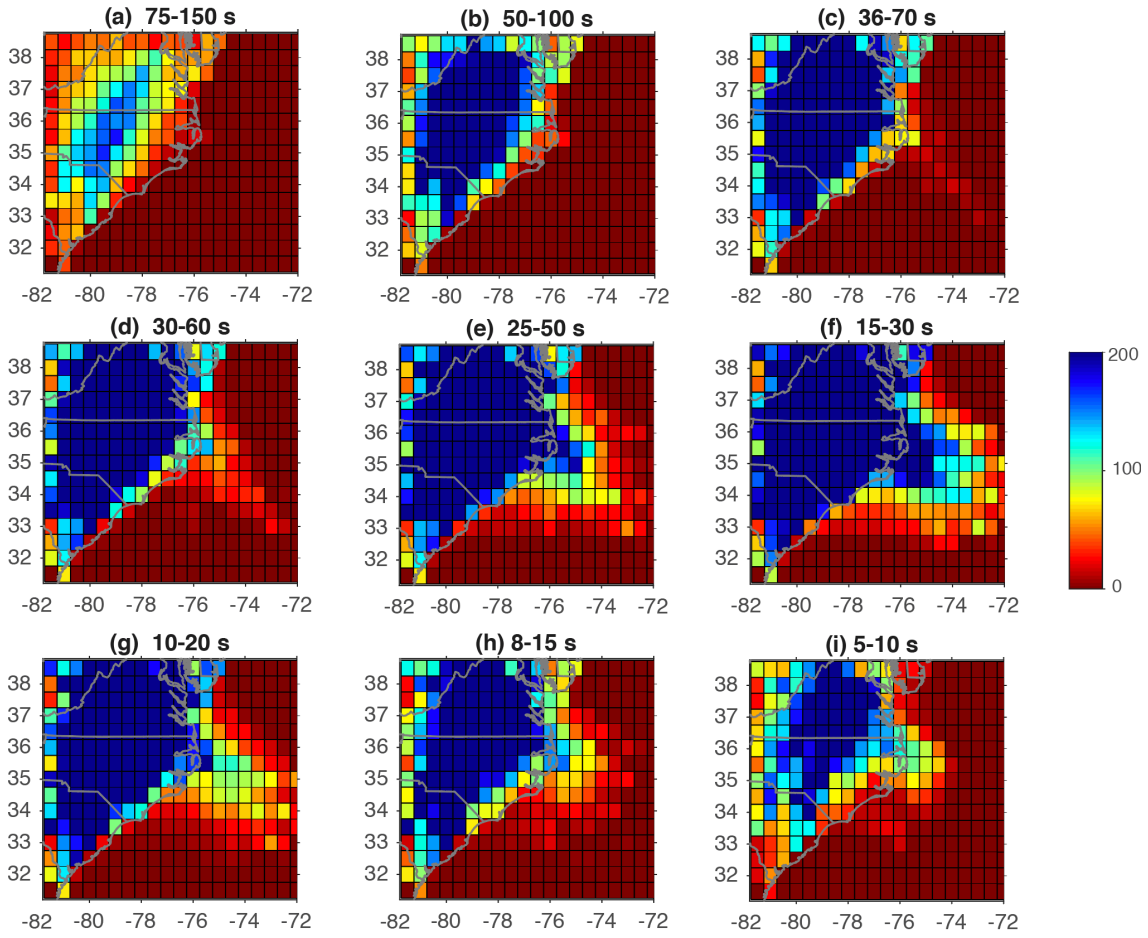

Figure C. 3. Seismic raypath density of the phase delay measurements that were used to invert for the final tomographic velocity model. The coverage is colored by the number of seismic rays within each 0.5°×0.5° cell. The phase delays are measured through cross-correlations between the observed EGFs and synthetic waveforms at multiple overlapped period ranges.

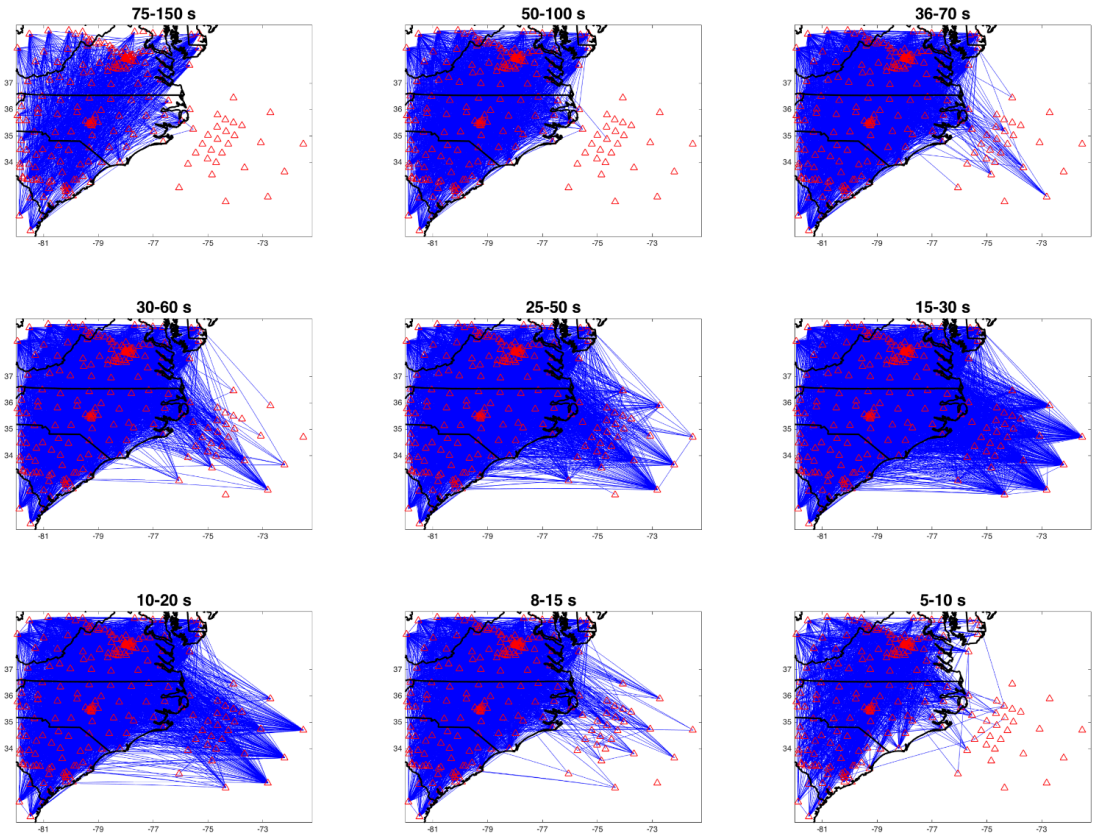

Figure C. 4. Directional distribution of seismic raypaths that were in our tomography. The red triangle marks the station and the blue line indicate the raypath between two stations.

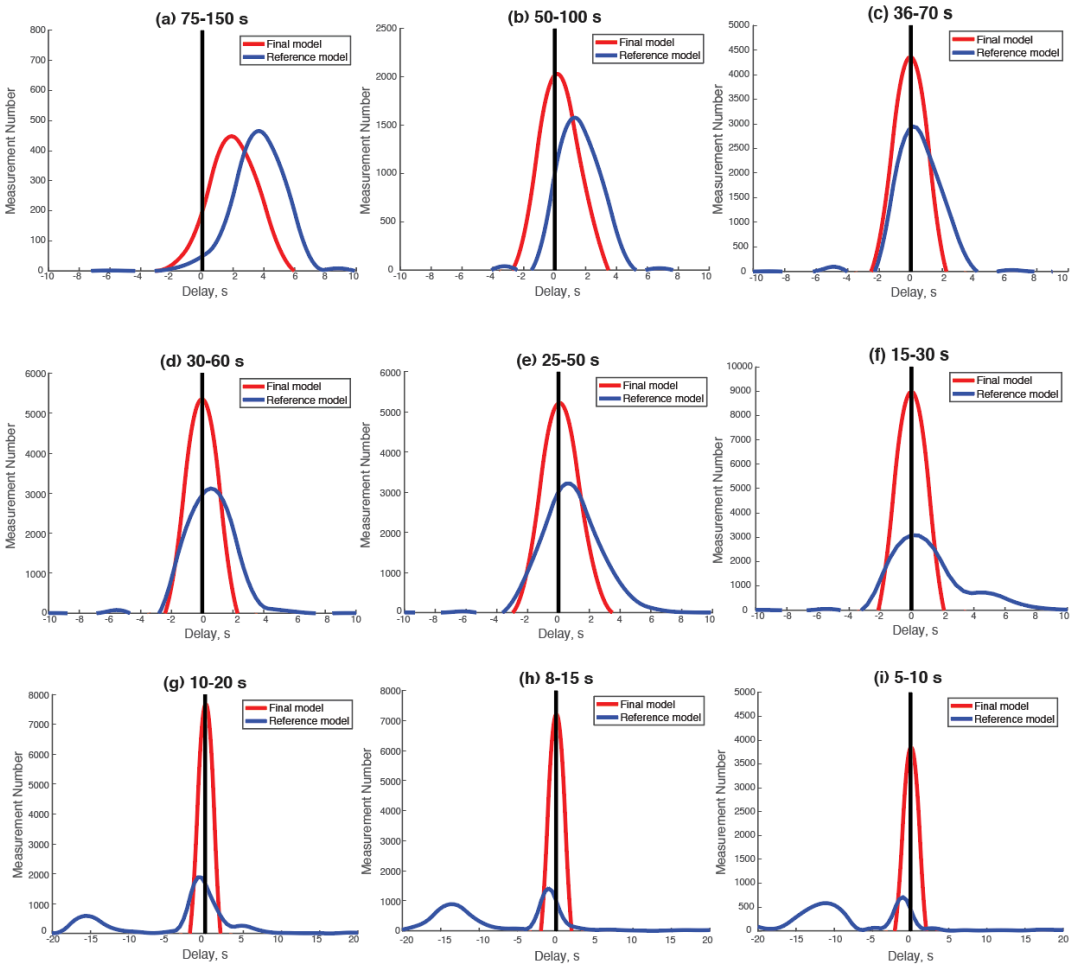

Figure C.5. Comparison of phase delay time between the observed and synthetic waveforms from the initial reference model (blue) and our full-wave ambient noise tomography (red) at multiple periods.

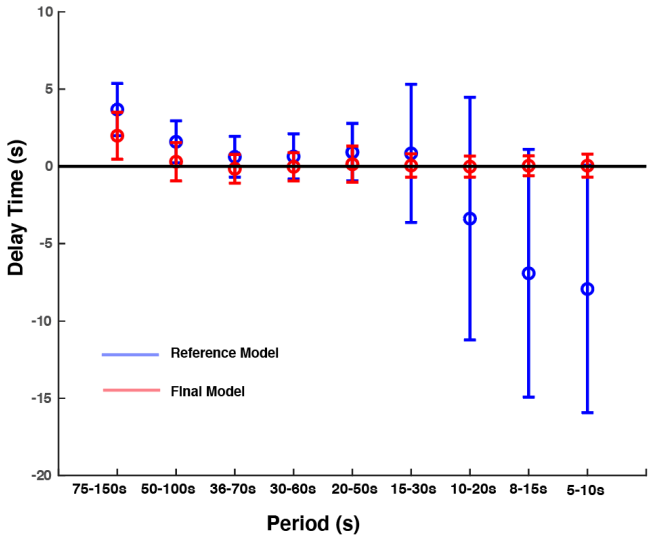

Figure C. 6. The average of the phase delays at each period from the reference and the final preferred model after 5 iterations. The error bar shows the standard deviation for each period corresponding to panels (a) to (i) in Figure C.5. The blue bars are measurements from the reference model and the red bars are from the final preferred model.

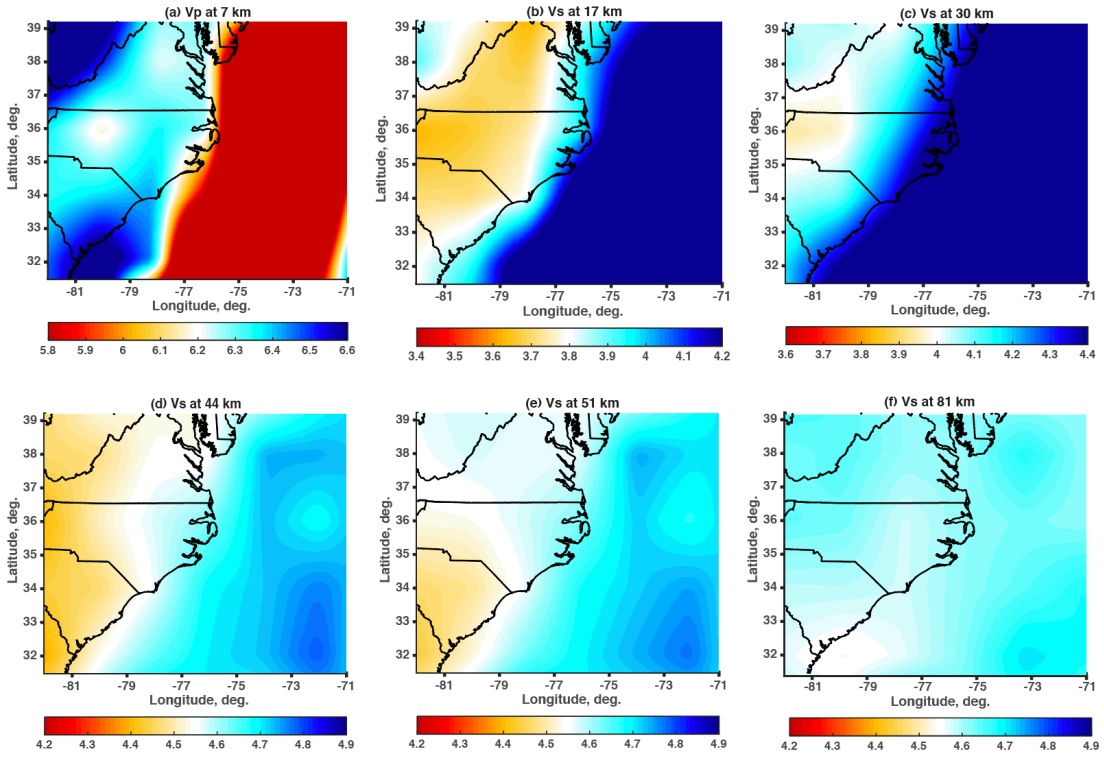

Figure C.7. Seismic velocity structures (in km/s) from the initial reference velocity model provided by Shapiro & Ritzwoller (2002). (a) P-wave velocities at the depth of 7 km; (b)-(f) S-wave velocities at the depths of 17 km, 30 km, 44 km, 51 km, and 81 km, respectively.

Appendix C

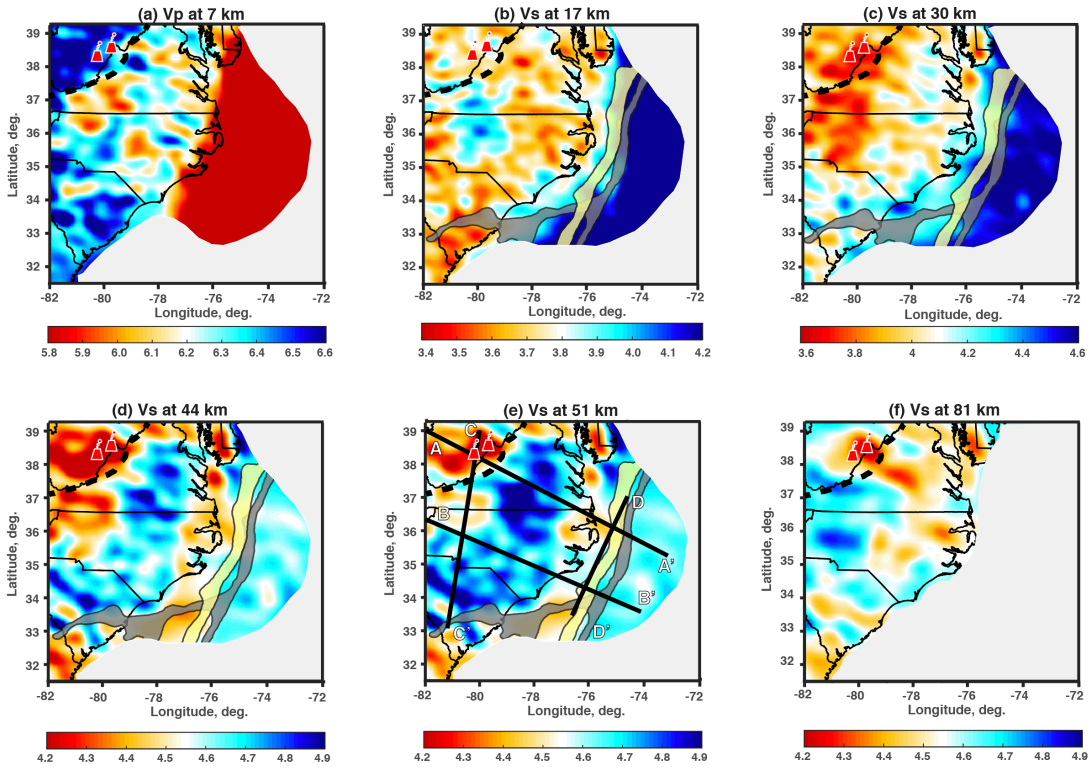

Figure C. 8. Seismic velocity structures (in km/s) from our preferred model. (a) P-wave velocities at the depth of 7 km; (b)-(f) S-wave velocities at the depths of 17 km, 30 km, 44 km, 51 km, and 81 km, respectively.

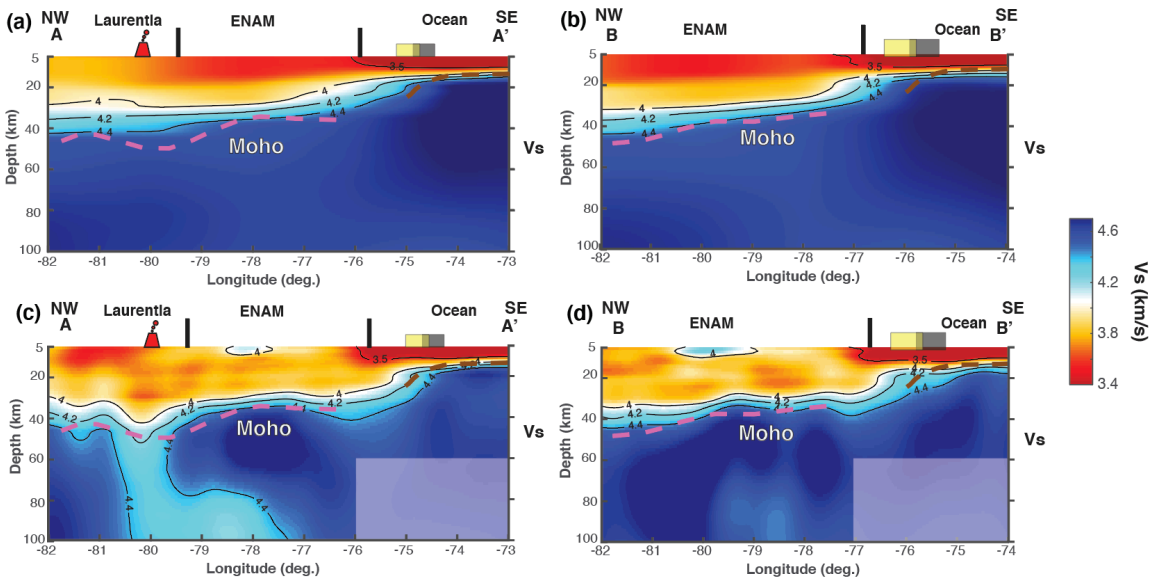

2150

2151 ***Figure C. 9. Comparison of the initial reference velocity model provided by Shapiro &***

2152 ***Ritzwoller (2002) (a-b) and the S-wave velocity models from this study (c-d)***

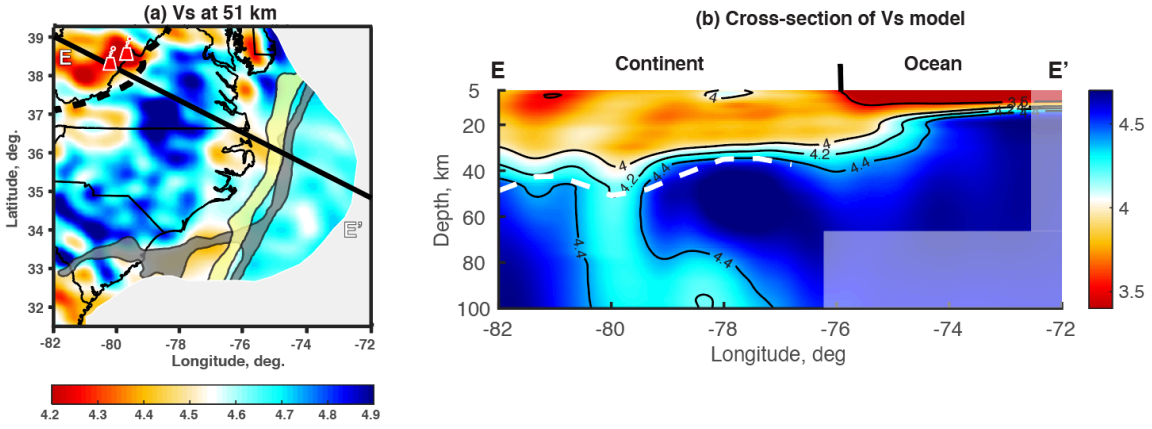

2153

2154 ***Figure C. 10. (a) Variation of S-wave velocity at depth of 51 km (b) Cross-sections of the***

2155 ***seismic tomographic model. The location of Cross-section marks in (a)***

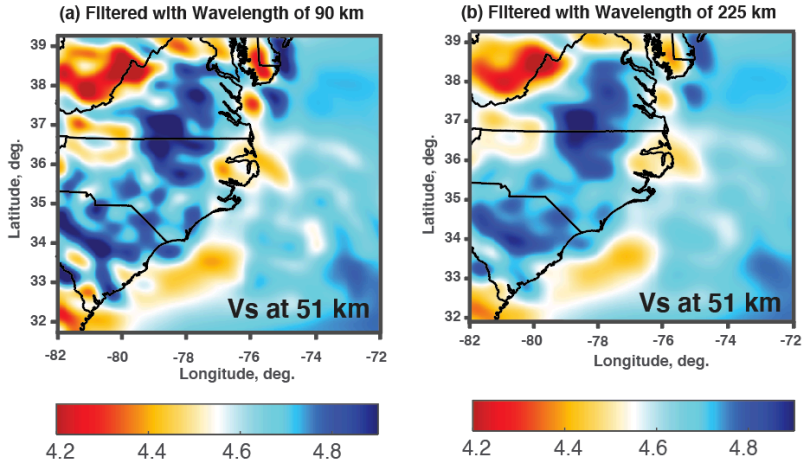

Figure C. 11. S-wave velocity at 51 km filtered with wavelengths (a) 90 km and (b)225 km.

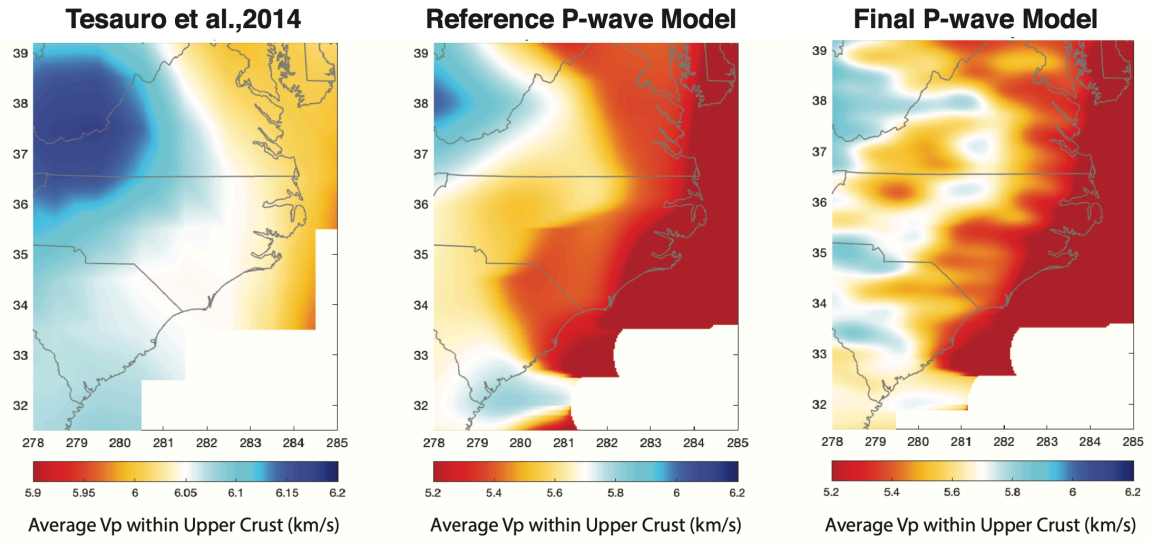

Figure C. 12. The comparison of average P-wave velocity (in km/s) within the upper crust from (a) Tesauro et al., (2014), (b) Shapiro & Ritzwoller, (2002), and (c) This study

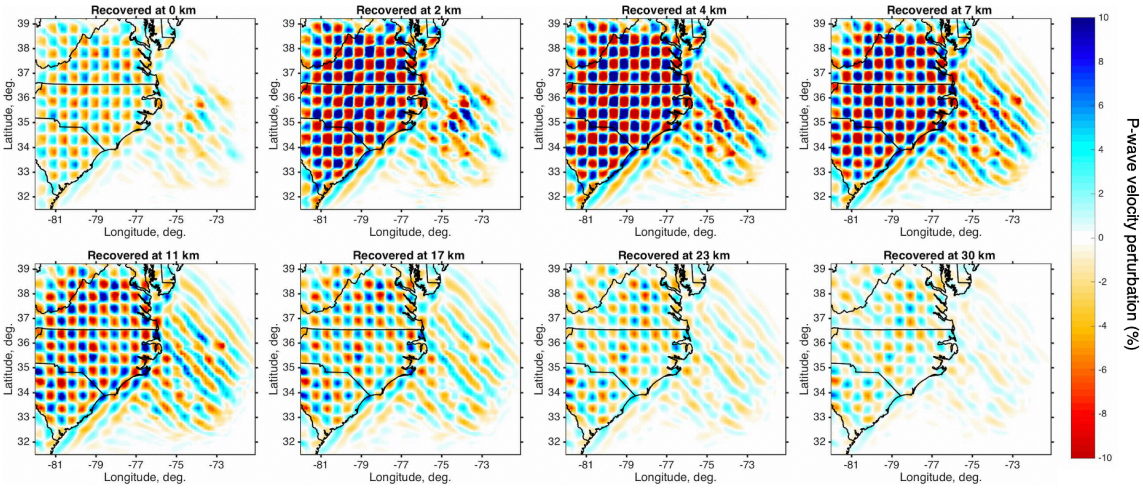

Figure C.13. 3D checkerboard resolution tests for the P-wave velocity model. The velocity perturbation varies within ±10% in the input models. The horizontal scale (cell size) is 50 km.

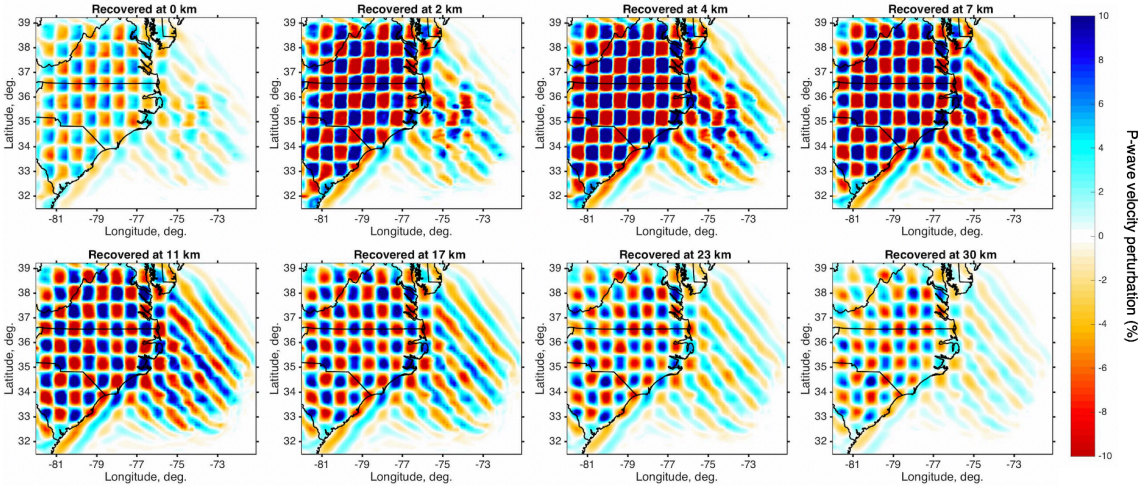

Figure C.14. 3D checkerboard resolution tests for the P-wave velocity model. The velocity perturbation varies within ±10% in the input models. The horizontal scale (cell size) is 75 km.

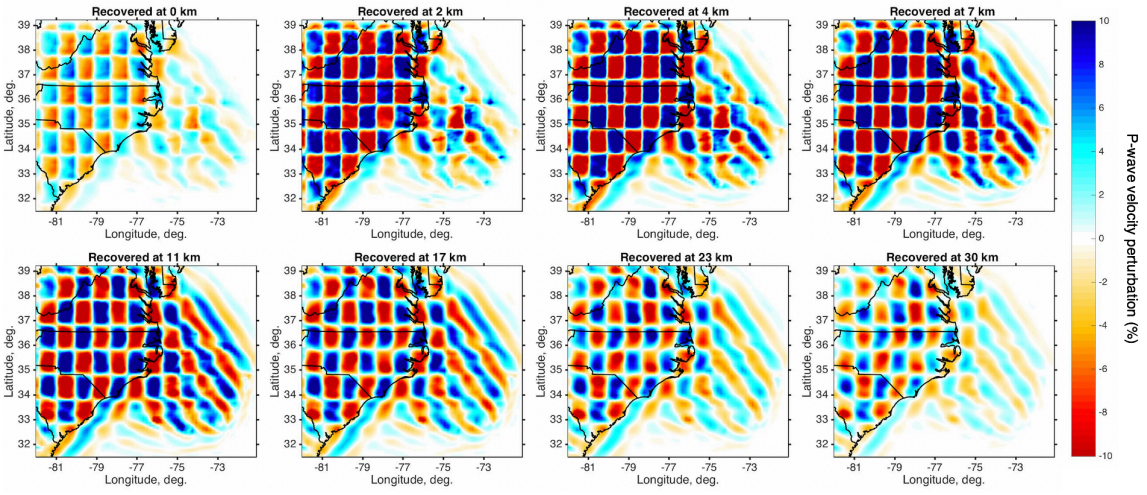

2171

2172 ***Figure C.15. 3D checkerboard resolution tests for the P-wave velocity model. The***

2173 ***velocity perturbation varies within ±10% in the input models. The horizontal scale (cell***

2174 ***size) is 100 km.***

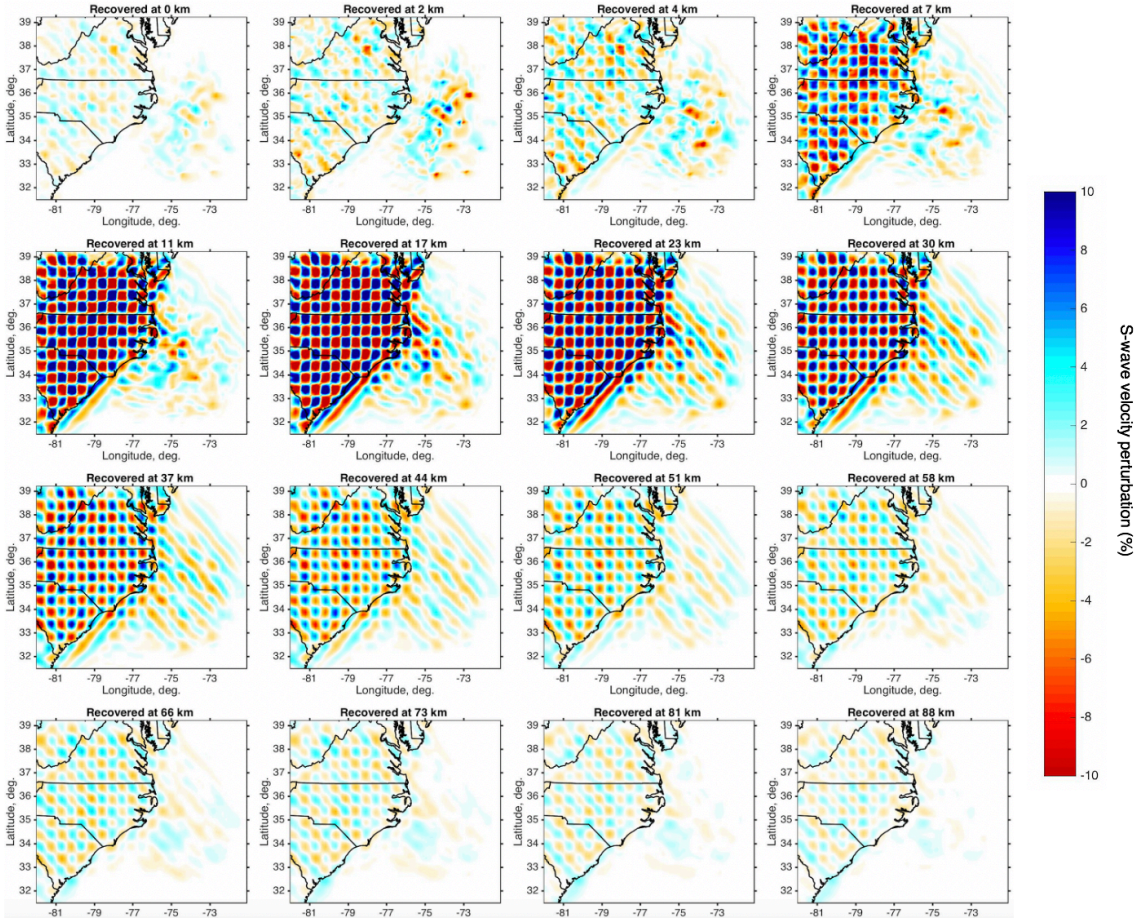

2175

Figure C.16. 3D checkerboard resolution tests for the S-wave velocity model. The velocity perturbation varies within ±10% in the input models. The horizontal scale (cell size) is 50 km.

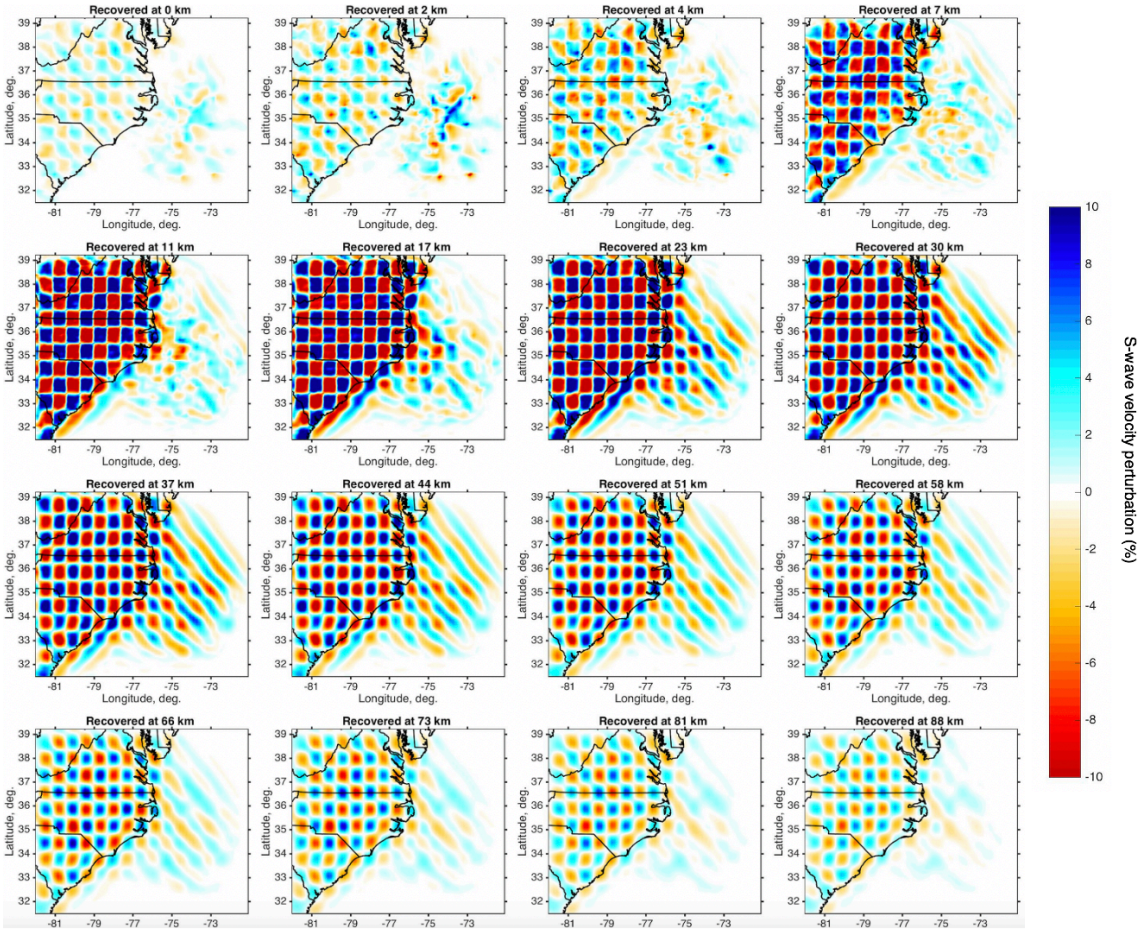

Figure C.17. 3D checkerboard resolution tests for the S-wave velocity model. The velocity perturbation varies within ±10% in the input models. The horizontal scale (cell size) is 75 km.

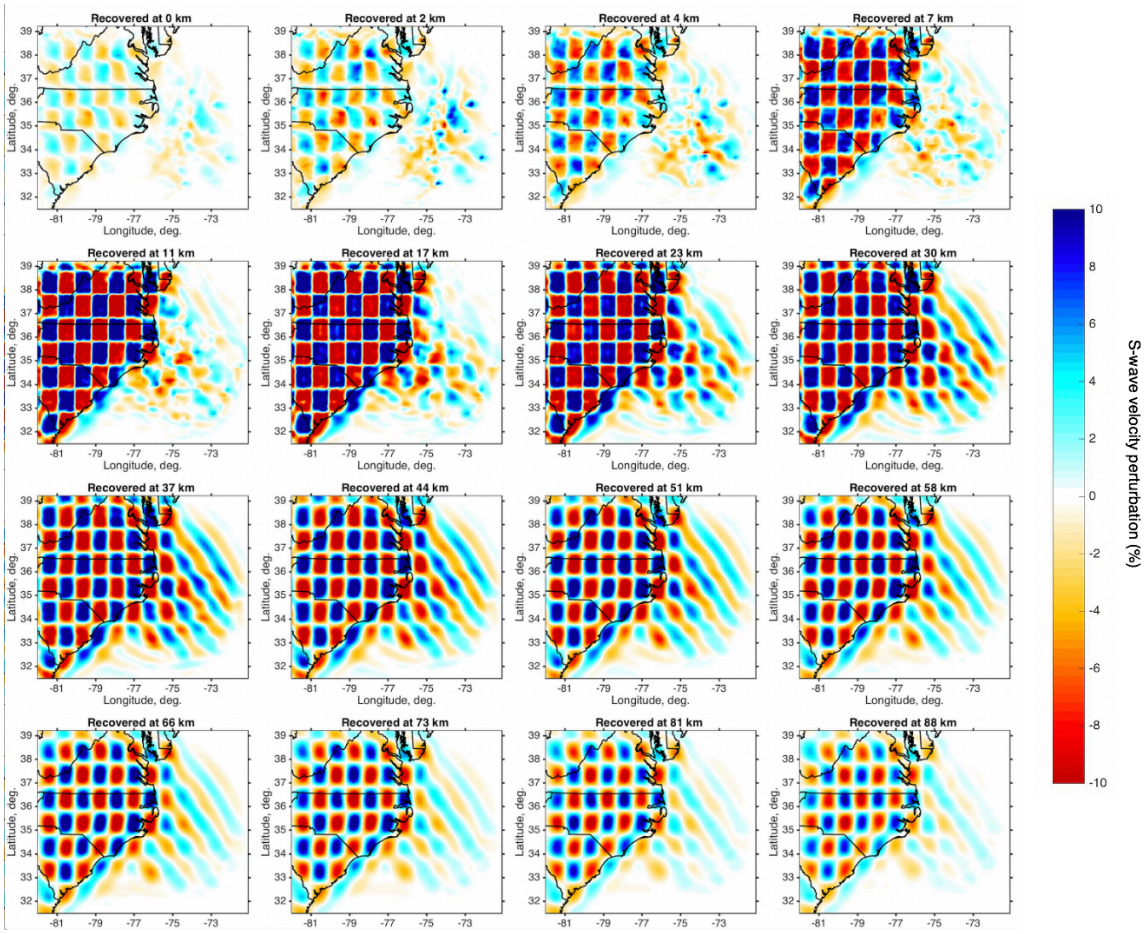

Figure C.18. 3D checkerboard resolution tests for the S-wave velocity model. The velocity perturbation varies within ±10% in the input models. The horizontal scale (cell size) is 100 km.

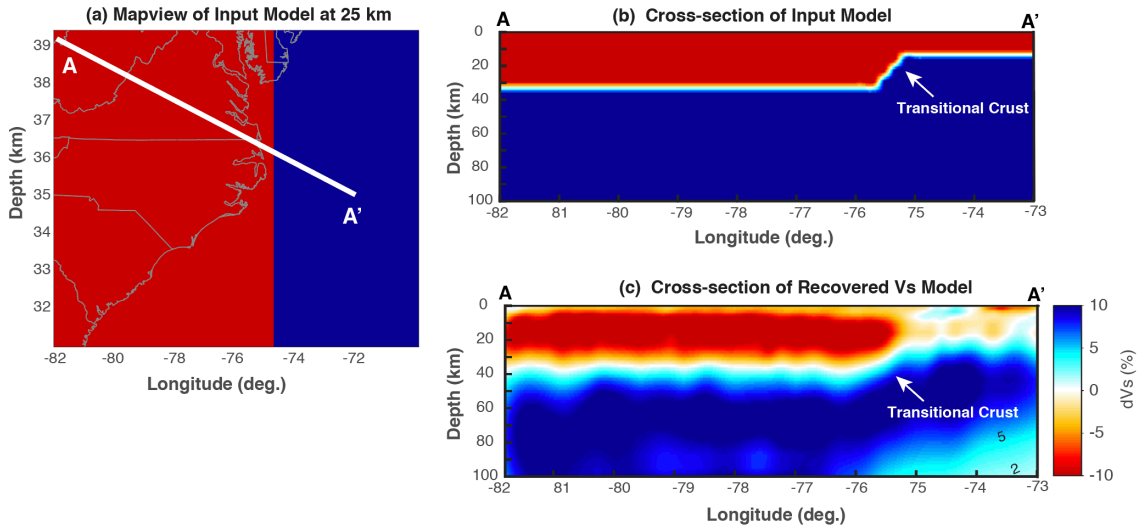

2187

2188 ***Figure C.19. The model recovery test for the observed crustal thickness variation across***

2189 ***the oceanic-continental transitional zone. (a-b) The input model based on our***

2190 ***tomographic imaging. We assume a 10% velocity perturbation for the upper mantle and***

2191 ***a -10% perturbation for the crust. The white solid line in (a) marks the location of***

2192 ***velocity profile in (b) and (c). (c) The cross-section of recovered models for Vs***

2193 ***perturbation within a depth range of 0-100 km. The solid lines mark the velocity***

2194 ***perturbation contours of -3%, 0%, 2% and 5%, respectively.***

2195

2196

2197

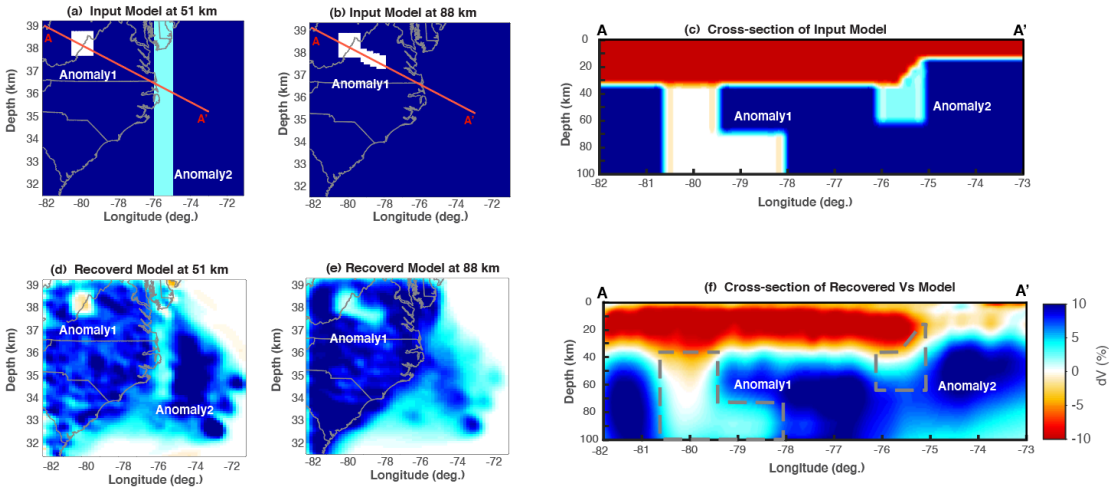

2198

2199 ***Figure C.20. Model recovery tests for low-velocity anomalies in the mantle lithosphere***
2200 ***beneath the Virginia volcanoes and the transitional crust. (a-c) The input model based***
2201 ***on our tomographic imaging. In comparison with the surrounding upper mantle***
2202 ***velocities, we set 10% velocity reduction for the anomaly beneath the Virginia volcanos***
2203 ***and a 8% velocity reduction for the anomaly beneath ocean-continent transitional crust.***
2204 ***The red solid lines in (a) and (b) mark the location of velocity profile in (c) and (d). (d-f)***
2205 ***The recovered models for Vs perturbation.***

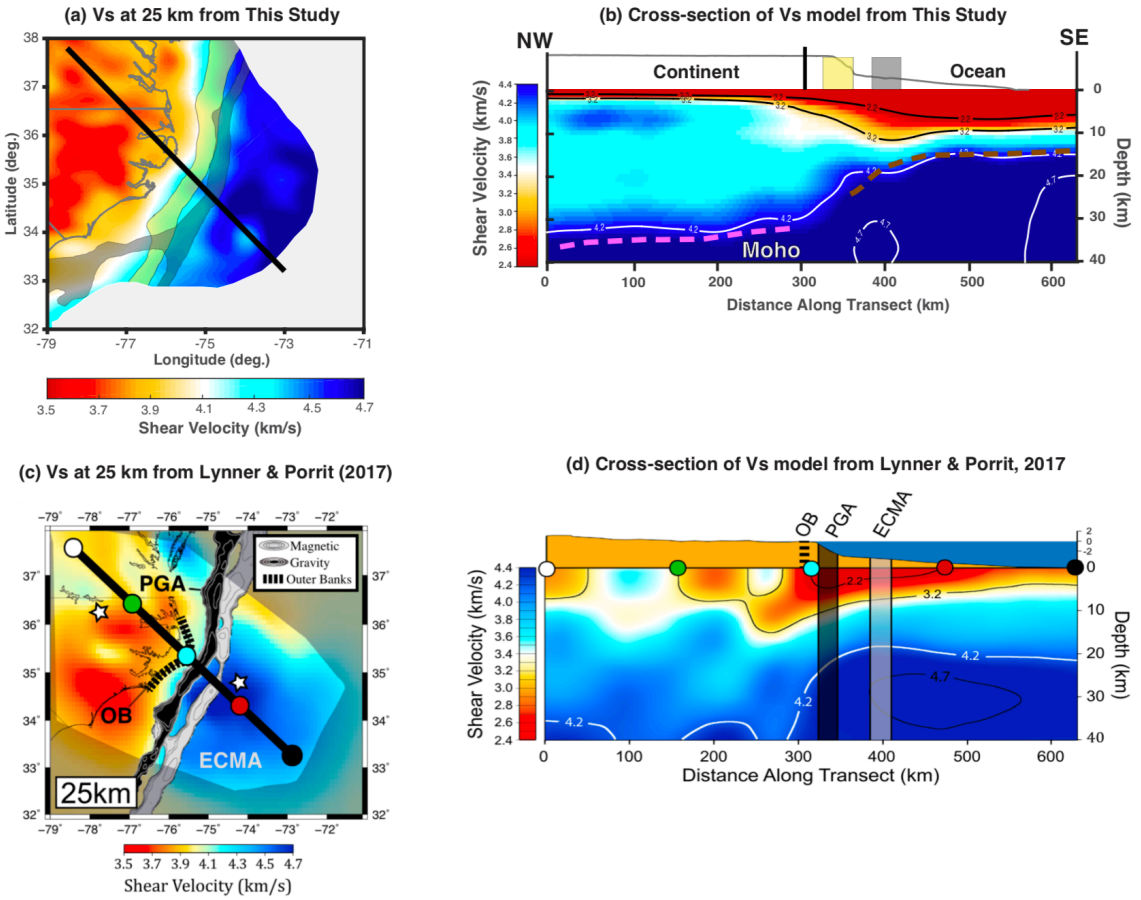

Figure C.21. Comparison of S-wave velocity models from (a-b) this study and (c-d) Lynner and Porrit (2017). The yellow and gray patches in (a) and (b) denote the observed positive gravity anomaly (PGA) and the East Coast magnetic anomaly (ECMA), respectively. The pink and brown dashed line in (b) represents the Moho depth picked from teleseismic receiver function analysis by Li et al. (2020) and the active-source seismic surveys from Holbrook et al. (1994), respectively. The location of cross-sections in (b) and (d) is marked by the black solid lines in (a) and (c).

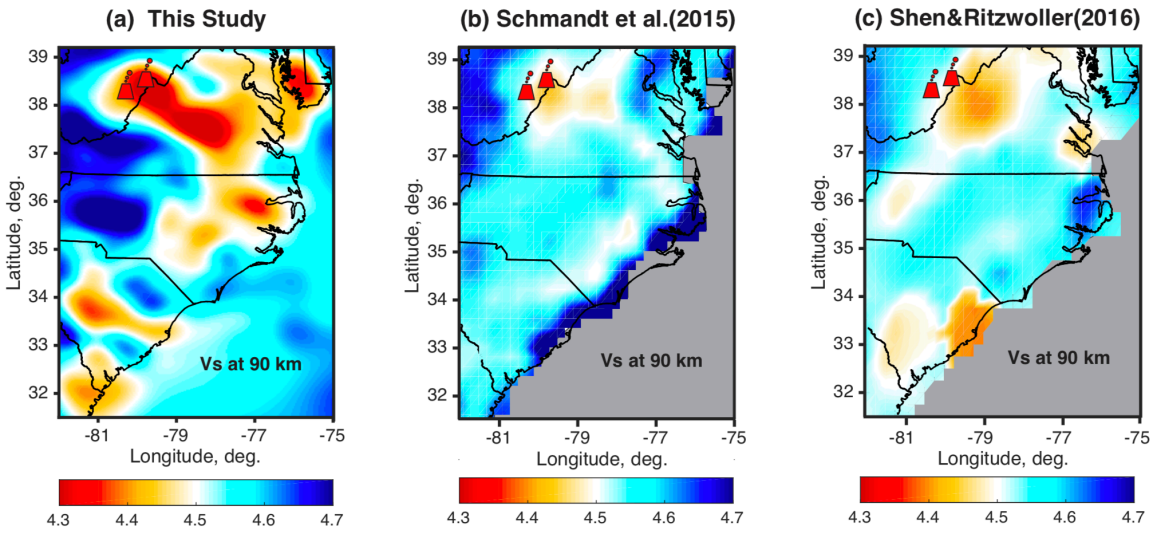

2214

2215 ***Figure C. 22. Comparison of S-wave velocities (in km/s) at the depth of 90 km from (a)***

2216 ***this study, (b) Schmandt et al. (2015), and (c) Shen and Ritzwoller (2016). The red cones***

2217 ***mark the location of Virginia volcanoes.***

BIBLIOGRAPHY

Accardo, N. J., Gaherty, J. B., Shillington, D. J., Hopper, E., Nyblade, A. A., Ebinger, C. J., et al. (2020). Thermochemical modification of the upper mantle beneath the northern Malawi Rift constrained from shear velocity imaging. *Geochemistry, Geophysics, Geosystems, 21*, 6. doi:10.1029/2019GC008843

Albuquerque Seismological Laboratory (ASL)/USGS. (1988). Global Seismograph Network (GSN - IRIS/USGS). International Federation of Digital Seismograph Networks. Other/Seismic Network. doi:10.7914/SN/IU.

Albuquerque Seismological Laboratory (ASL)/USGS. (1990). United States National Seismic Network. International Federation of Digital Seismograph Networks. Other/Seismic Network. doi:10.7914/SN/US

Albuquerque Seismological Laboratory (ASL)/USGS (1994): New England Seismic Network. International Federation of Digital Seismograph Networks. Other/Seismic Network. doi:10.7914/SN/NE

Allen, J. S., Thomas, W. A., & Lavoie, D. (2009). Stratigraphy and structure of the Laurentian rifted margin in the northern Appalachians: A low-angle detachment rift system. *Geology, 37*(4), 335-338. doi:10.1130/G25371A.1

Ammon, C. (1991). The isolation of receiver effects from teleseismic P waveforms. *Bulletin of the Seismological Society of America, 81*(6), 2504-2510. doi:10.1029/2005JB004161

Ando, C. J., Czuchra, B. L., Klemperer, S. L., Brown, L. D., Cheadle, M. J., Cook, F. A., et al. (1984). Crustal profile of mountain belt - COCORP deep seismic reflection profiling in New England Appalachians and implications for architecture of

convergent mountain chains. *The American Association of Petroleum Geologists Bulletin, 68*(7), 819-837.

Austin, J. A., Stoffa, P. L., Phillips, J. D., Oh, J., Sawyer, D. S., Purdy, G. M., et al. (1990). Crustal structure of the Southeast Georgia Embayment-Carolina Trough: preliminary results of a composite seismic image of a continental suture and a volcanic passive margin. *Geology, 18*(10), 1023-1027. doi:10.1130/00917613(1990)018<1023:CSOTSG>2.3.CO;2

Bakun, W., & Hopper, M. (2004). Magnitudes and locations of the 1811-1812 New Madrid, Missouri, and the 1886 Charleston, South Carolina, earthquakes. *Bulletin of the Seismological Society of America, 94*(1), 64-75. doi:10.1785/0120020122

Biryol, C. B., Wagner, L. S., Fischer, K. M., & Hawman, R. B. (2016). Relationship between observed upper mantle structures and recent tectonic activity across the Southeastern United States. *Journal of Geophysical Research: Solid Earth, 121*, 3393-3414. doi:10.1002/2015JB012698

Bonvalot, S., Balmino, G., Briais, A., Kuhn, M., Peyrefitte, A., Vales N., et al. (2012). *World Gravity Map* (scale 1:50000000). Paris: BGI-CGMW-CNES-IRD.

Bradley, D. C. (1983). Tectonics of the Acadian Orogeny in New England and adjacent Canada. *Journal of Geology, 91*(4), 381-400.

Bradley, D. C., Tucker, R. D., Lux, D. R., Harris, A. G., & McGregor, D. C. (2000). Migration of the Acadian Orogen and Foreland basin across the Northern Appalachians of Maine and adjacent areas. *US Geological Survey Professional Paper*, (1624), 44-50.

Bradley, D. C. (2008). Passive margins through earth history. *Earth-Science Reviews, 91*(1), 1-26. doi: 10.1016/j.earscirev.2008.08.001

Byrnes, J. S., Bezada, M., Long, M. D., & Benoit, M. H. (2019). Thin lithosphere beneath the central Appalachian Mountains: Constraints from seismic attenuation beneath the MAGIC array. *Earth and Planetary Science Letters, 519*, 297-307. doi: 10.1016/j.epsl.2019.04.045

Card, K. D. (1990). A review of the Superior Province of the Canadian Shield, a product of Archean accretion. *Precambrian Research, 48*(1-2), 99-156. doi:10.1016/0301-9268(90)90059-Y

Cassidy, J. F. (1992). Numerical experiments in broadband receiver function analysis. *Bulletin of the Seismological Society of America, 82*(3), 1453-1474. http://www.bssaonline.org/content/82/3/1453

Cheney, J. T., & Brady, J. B. (1992). Petrology of the high-alumina hoosac schist from the chloritoid+garnet through the kyanite+biotite zones in western Massachusetts. In Robinson, P. & Brady, J. B. (Eds.), *Guidebook for Field Trips in the Connecticut Valley Region of Massachusetts and Adjacent States* (pp. 332-357). Amherst, Massachusetts: University of Massachusetts, Amherst

Christensen, N. I., & Mooney, W. D. (1995). Seismic velocity structure and composition of the continental crust: A global view. *Journal of Geophysical Research: Solid Earth, 100*, B6. doi: 10.1029/95JB00259

Christensen, N. I. (1996). Poisson's ratio and crustal seismology. *Journal of Geophysical Research, 101*, 3139. doi:10.1029/95JB03446

Colorado Geological Survey (2016). Colorado Geological Survey Seismic Network. International Federation of Digital Seismograph Networks. Dataset/Seismic Network. doi:10.7914/SN/C0

Connolly, J. A. D. (2009). The geodynamic equation of state: What and how. *Geochemistry, Geophysics, Geosystems, 10*(10). doi:10.1029/2009GC002540

Cook, F. A., & Vasudevan, K. (2006). Reprocessing and enhanced interpretation of the initial COCORP Southern Appalachians traverse. *Tectonophysics, 420*(1-2), 161-174. doi:10.1016/j.tecto.2006.01.022

Culotta, R. C., Pratt, T., & Oliver, J. (1990). A tale of two sutures: COCORP's deep seismic surveys of the Grenville province in the eastern U.S. midcontinent. *Geology, 18*(7), 646-649. doi:10.1130/0091-7613(1990)018<0646:ATOTSC>2.3.CO;2

Darbyshire, F. A., Bastow, I. D., Petrescu, L., Gilligan, A., & Thompson, D. A. (2017). A tale of two orogens: Crustal processes in the Proterozoic Trans-Hudson and Grenville Orogens, eastern Canada. *Tectonics, 36*(8), 1633-1659. doi:10.1002/2017TC004479

Das, R. & Rai. S. S. (2016). Seismic interferometry and ambient noise tomography: theoretical background and application in south India. *Journal of Physics: Conference Series 759*(1). doi:10.1088/1742-6596/759/1/012006

David, J., Godin, L., Stevenson, R., O'Neil, J., & Francis, D. (2009). U-Pb ages (3.8-2.7 Ga) and Nd isotope data from the newly identified Eoarchean Nuvvuagittuq supracrustal belt, superior Craton, Canada. *Bulletin of the Geological Society of America, 121*(1-2), 150-163. doi:10.1130/B26369.1

Domeier, M. (2016). A plate tectonic scenario for the Iapetus and Rheic oceans.

Gondawana Research, 36, 275-295. doi:10.1016/j.gr.2015.08.003

Dong, M. D. T., & Menke, W. H. (2017). Seismic high attenuation region observed beneath southern New England from teleseismic body wave spectra: Evidence for high asthenospheric temperature without melt. *Geophysical Research Letters, 44*, 10,958-10,969. doi:10.1002/2017GL074953

Dorais, M. J., & Paige, M. L. (2000). Regional geochemical and isotopic variations of Northern New England plutons: Implications for magma sources and for Grenville and Avalon basement-terrane boundaries. *Bulletin of the Geological Society of America, 112*(6), 900-941. doi:10.1130/0016-7606(2000)112<900:RGAIVO>2.0.CO;2

Dorais, M. J., Atkinson, M., Kim, J., West, D. P., & Kirby, G. A. (2012). Where is the Iapetus suture in northern New England? A study of the Ammonoosuc Volcanics, Bronson Hill terrane, New Hampshire. *Canadian Journal of Earth Sciences, 49*(1), 189-205. doi:10.1139/e10-108

Dueker, K. G., & Sheehan, A. F. (1998). Mantle discontinuity structure beneath the Colorado Rocky Mountains and High Plains. *Journal of Geophysical Research: Solid Earth, 103*(B4), 7153-7169. doi:10.1029/97JB03509

Eaton, D. W., & Frederiksen, A. (2007). Seismic evidence for convection-driven motion of the North American plate. *Nature, 446*(7134), 428-431. doi:10.1038/nature05675

Evans, R. L., Benoit, M. H., Long, M. D., Elsenbeck, J., Ford, H. A., Zhu, J., et al. (2019). Thin lithosphere beneath the central Appalachian Mountains: A combined seismic

and magnetotelluric study. *Earth and Planetary Science Letters, 519*, 308-316. doi:10.1016/j.epsl.2019.04.046

Field, E., & Jacob, K. (1993). The theoretical response of sedimentary layers to ambient seismic noise. *Geophysical Research Letters, 20*(24), 2925-2928. doi:10.1029/93GL03054

Fischer, K. M. (2002). Waning buoyancy in the crustal roots of old mountains. Nature, 417(6892), 933-936. doi:10.1038/nature00855

Fischer, K. M., Hawman, R. B.,& Wagner L. S., (2010). Southeastern Suture of the Appalachian Margin Experiment. International Federation of Digital Seismograph Networks. Dataset/Seismic Network. doi:10.7914/SN/Z9_2010

Frederiksen, A. W., & Bostock, M. G. (2000). Modelling teleseismic waves in dipping anisotropic structures. Geophysical Journal International, 141(2), 401-412. doi:10.1046/j.1365-246X.2000.00090.x

Frizon de Lamotte, D., Fourdan, B., Leleu, S., Leparmentier, F., & Clarens, P. de (2015). Style of rifting and the stages of Pangea breakup. *Tectonics, 34*, 1009-1029. doi:10.1002/2014TC003760

Gaherty, J. B., & Dunn, R. A. (2007). Evaluating hotspot-ridge interaction in the Atlantic from regional-scale seismic observations. *Geochemistry, Geophysics, Geosystems, 8*(5). doi:10.1029/2006GC001533

Gaherty, J. B., Dalton, C., & Levin, V. (2011). *A three-dimensional model of crustal structure in the central and eastern US derived from broadband ambient-noise surface waves and receiver functions*. United State: U.S. Geological Survey.

Gaherty, J. B., Wagner, L. S., Becel, A., Benoit, M., Long, M. D., Shillington, D., Dugan,

B., et al. (2014). Eastern North American Margin Community Seismic Experiment. International Federation of Digital Seismograph Networks. Dataset/Seismic Network. doi:10.7914/SN/YO_2014

Gao, H. & Shen, Y. (2014). Upper mantle structure of the Cascades from full-wave ambient noise tomography: Evidence for 3D mantle upwelling in the back-arc. *Earth and Planetary Science Letters, 309*, 222-233. doi:10.1016/j.epsl.2014.01.012

Gao, H. (2018). Three-dimensional variation of the slab geometry correlate with earthquake distributions at the Cascadia subduction system. *Nature Communication.* doi:10.1038/s41467-018-03655-5

Geological Survey of Canada. (1989). Canadian National Seismograph Network. International Federation of Digital Seismograph Networks. Other/Seismic Network. doi:10.7914/SN/CN

Geological Survey of Canada. (2000). Portable Observatories for Lithospheric Analysis and Research Investigating Seismicity (POLARIS). International Federation of Digital Seismograph Networks. Other/Seismic Network.

Goes, S., Armitage, J. J., Harmon, N., Smith, H., & Huismans, R. (2012). Low seismic velocities below mid-ocean ridges: Attenuation versus melt retention. *Journal of Geophysical Research, 117*, B12403. doi:10.1029/2012JB009637

Guo, W., Zhao, S., Wang, F., Yang, Z., Jia, S., & Liu, Z. (2019). Crustal structure of the eastern Piedmont and Atlantic coastal plain in North Carolina and Virginia, eastern North American margin. *Earth, Planets and Space, 71*(1). doi:10.1186/s40623-019-1049-z

2375 Guo, Z., Xue, M., Aydin, A., & Ma, Z. (2020). Exploring source regions of single-and
2376 double-frequency microseisms recorded in eastern North American margin
2377 (ENAM) by cross-correlation. *Geophysical Journal International, 220*(2), 1352-
2378 1367. doi:10.1093/gji/ggz470

2379 Hales, A. L., Helsley, C. E., Dowling, J. J., Nation, J. B. (1968). The east coast onshore-
2380 offshore experiment, I. The first arrival phases. *Bulletin of the Seismological*
2381 *Society of America, 58*(3):757-819.

2382 Hansen, S., & Dueker, K. (2009). P- and S-wave receiver function images of crustal
2383 imbrication beneath the Cheyenne belt in southeast Wyoming. *Bulletin of the*
2384 *Seismological Society of America, 99*(3), 1953-1961. doi:10.1785/0120080168

2385 Harrison, T. M., Spear, F. S., & Heizler, M. T. (1989). Geochronologic studies in central
2386 New England II: post-Acadian hinged and differential uplift. *Geology, 17*(2), 185-
2387 189. doi:10.1130/0091-7613(1989)017<0185:GSICNE>2.3.CO;2

2388 Hatcher, R. D. (2010). The Appalachian orogen: A brief summary, from Rodinia to Pangea:
2389 The Lithotectonic Record of the Appalachian Region. *The Geological Society of*
2390 *America, Memoir 206*, 1-19. doi:10.1130/2010.1206(01)

2391 Heaman, L. M., & Kjarsgaard, B. A. (2000). Timing of eastern North American kimberlite
2392 magmatism: Continental extension of the Great Meteor hotspot track? *Earth and*
2393 *Planetary Science Letters, 178*(3-4), 253-268. doi:10.1016/S0012-
2394 821X(00)00079-0

2395 Hennet, C. G., Luetgert, J. H., & Phinney, R. A. (1991). The crustal structure in central
2396 Maine from coherency processed refraction data. *Journal of Geophysical*
2397 *Research, 96*(B7), 12023-12037.

Hibbard, J. P., Van Staal, C. R., Rankin, D. W., & Williams, H. (2006). *Lithotectonic map of the Appalachian orogen* (MAP NO. 2096A, scale 1:5000000). Canada-United States of America: Geological Survey of Canada.

Hibbard, J. P., van Staal, C. R., & Rankin, D. W. (2007). A comparative analysis of pre-Silurian crustal building blocks of the northern and the southern Appalachian orogen. *American Journal of Science, 307*(1), 23-45. doi:10.2475/01.2007.02

Hibbard, J. P., & Karabinos, P. (2013). Disparate paths in the geologic evolution of the northern and southern Appalachians: a case for inherited contrasting crustal/lithospheric substrates. *Geoscience Canada, 40*(4), 303-317. doi:10.12789/geocanj.2013.40.021

Holbrook, W. S., Purdy, G. M., Sheridan, R. E., Glover, L., Talwani, M., Ewing, J., et al. (1994). Seismic structure of the U.S. mid-Atlantic continental margin. Journal of Geophysical Research Atmospheres, 991(B9), 17871-17891. doi:10.1029/94JB00729

Holbrook, W. S., & Kelemen, P. B. (1993). Large igneous province on the US Atlantic margin and implications for magmatism during continental breakup. Nature, 364, 433-436. doi:10.1038/364433a0

Hopper, E., Fischer, K. M., Wagner, L. S., & Hawman, R. B. (2017). Reconstructing the end of the Appalachian orogeny. *Geology, 45*(1), 15-18. doi:10.1130/G38453.1

Horton, J. W., Chapman, M. C., & Green, R. A. (2015). The 2011 Mineral, Virginia, earthquake, and its significance for seismic hazards in eastern North America - Overview and synthesis. *Geological Society of America Special Papers, 509*, 1-25. doi:10.1130/2015.2509(01)

Hughes, S., & Luetgert, J. H. (1991). Crustal structure of the western New England Appalachians and the Adirondack Mountains. *Journal Of Geophysical Research-Solid Earth, 96*(B10), 16471-16494. doi:10.1029/91jb01657

Hughes, S., & Luetgert J. H. (1992). Crustal structure of the southeastern Grenville Province, northern New York State and eastern Ontario. *Journal Of Geophysical Research-Solid Earth*, *97*(B12), 17455-17479.

Huismans, R. S., & Beaumont, C. (2008). Complex rifted continental margins explained by dynamical models of depth-dependent lithospheric extension. *Geology, 36*(2), 163-166. doi:10.1130/G24231A.1

Hynes, A., & Rivers, T. (2010). Protracted continental collision; evidence from the Grenville Orogen. *Canadian Journal of Earth Sciences, 47*(5), 591-620. doi:10.1139/E10-003

IRIS Transportable Array. (2003). USArray Transportable Array: International Federation of Digital Seismograph Networks. Other/Seismic Network. doi:10.7914/SN/TA.

Jackson, I., & Faul, U. H. (2010). Grainsize-sensitive viscoelastic relaxation in olivine: Towards a robust laboratory based model for seismological application. *Physics of the Earth and Planetary Interiors, 183*(1-2), 151-163. doi:10.1016/j.pepi.2010.09.005

James, D. E., Smith, T. J., Steinhart, J. S. (1968). Crustal structure of the Middle Atlantic states. *Journal of Geophysical Research, 73*(6). doi:10.1029/JB073i006p01983

Jamieson, R. A., Beaumont, C., Warren, C. J., & Nguyen, M. (2010). The Grenville Orogen explained? Applications and limitations of integrating numerical models with

geological and geophysical data. *Canadian Journal of Earth Sciences, 47*, 517-539. doi:10.1139/E09-070

Janiszewski, H. A., Gaherty, J. B., Abers, G. A., Gao, H., & Eilon, Z. C. (2019). Amphibious surface-wave phase-velocity measurements of the Cascadia subduction zone. *Geophysical Journal International, 217*(3), 1929-1948. doi:10.1093/gji/ggz051

Jourdan, F., Marzoli, A., Bertrand, H., Cirilli, S., Tanner, L. H., Kontak, D. J., et al. (2009). Ar-40/Ar-39 ages of CAMP in North America: Implications for the Triassic-Jurassic boundary and the K-40 decay constant bias. *Lithosphere, 110*(1-4), 167-180. doi: 10.1016/j.lithos.2008.12.011

Karabinos, P., MacDonald, F.A., & Crowley, J.L. (2017). Bridging the gap between the foreland and hinterland I: geochronology and plate tectonic geometry of Ordovician magmatism and terrane accretion on the Laurentian margin of New England. *American Journal of Science, 317*, 515-554. https:// doi: 10.2475/05.2017.01

Kennett, B. L. N., & Engdahl, E. R. (1991). Traveltimes for global earthquake location and phase identification. *Geophysical Journal International, 105*(2), 429-465. doi:10.1111/j.1365-246X.1991.tb06724.x

Kentucky Geological Survey/Univ. of Kentucky (1982). Kentucky Seismic and Strong Motion Network. University of Kentucky. Dataset/Seismic Network. doi:10.7914/SN/KY

Klitgord, K. D., Hutchinson, D. R., & Schouten, H. (1988). U.S. Atlantic continental margin; Structure and tectonic framework. In R. E. Sheridan & J. A. Grow (Eds.),

The Geology of North America, The Atlantic Continental Margin, U.S (vol. 12, pp. 19-55). Denver, CO: Geological Society of America.

Kuiper, Y. D. (2016). Development of the Norumbega fault system in mid-Paleozoic New England, USA: An integrated subducted oceanic ridge model. *Geology, 44*(6), 455-458. doi:10.1130/G37599.1

Lamont Doherty Earth Observatory (LDEO), Columbia University. (1970). Lamont-Doherty Cooperative Seismographic Network (LCSN). International Federation of Digital Seismograph Networks. Other/Seismic Network.

Langston, C. A. (1979). Structure under Mount Rainier, Washington, inferred from teleseismic body waves. *Journal of Geophysical Research, 84*(B9), 4749. doi:10.1029/JB084iB09p04749

Laske, G., Masters, G., Ma, Z., & Pasyanos, M., (2013). Update on CRUST1.0-A 1-degree Global Model of Earth's Crust: *Geophysical Research Abstracts, 15*, Abstract EGU2013-2658.

Levin, V., Kim, W. Y., & Menke, W. (1995). Seismic velocities in the shallow crust of western New England and northern New York. *Bulletin of the Seismological Society of America*, *85*(1), 207-219.

Levin, V., & Park, J. (1997). P-SH conversions in a flat-layered medium with anisotropy of arbitrary orientation. *Geophysical Journal International, 131*(2), 253-266. doi:10.1111/j.1365-246X.1997.tb01220.x

Levin, V., Park, J., Brandon, M. T., & Menke, W. (2000). Thinning of the upper mantle during late Paleozoic appalachian orogenesis. Geology, 28(3), 239-242. doi:10.1130/0091-7613(2000)28<239:TOTUMD>2.0.CO;2

2488 Levin, V., Servali, A., Van Tongeren, J., Menke, W., & Darbyshire, F. (2017). Crust-
2489 mantle boundary in eastern North America, from the (oldest) craton to the
2490 (youngest) rift: The Crust-Mantle and Lithosphere-Asthenosphere Boundaries:
2491 Insights From Xenoliths, Orogenic Deep Sections and Geophysical Studies. In G.
2492 Bianchini et al. (Eds.), *The Geological Society of America special paper* (Vol. 526,
2493 pp. 107-131). Denver, Colorado: Geological Society of America.
2494 doi:10.1130/2017.2526(06)

2495 Li, A., Fischer, K. M., van der Lee, S., & Wysession, M. E. (2002). Crust and upper mantle
2496 discontinuity structure beneath eastern North America. *Journal of Geophysical*
2497 *Research: Solid Earth, 107*(B5), ESE 7-1-ESE 7-12. doi:10.1029/2001JB000190

2498 Li, A., Forsyth, D. W., & Fischer, K. M. (2003). Shear velocity structure and azimuthal
2499 anisotropy beneath eastern North America from Rayleigh wave inversion. *Journal*
2500 *of Geophysical Research: Solid Earth, 108*(B8), 2362. doi:10.1029/2002JB002259

2501 Li, C., Gao, H., Williams, M. L., & Levin, V. (2018). Crustal Thickness Variation in the
2502 Northern Appalachian Mountains: Implications for the Geometry of 3-D Tectonic
2503 Boundaries Within the Crust. *Geophysical Research Letters, 45*(12), 6061-6070.
2504 doi:10.1029/2018GL078777

2505 Li, Z. X., Bogdanova, S. V., Collins, A. S., Davidson, A., De Waele, B., Ernst, R. E., et al.,
2506 (2008). Assembly, configuration, and break-up history of Rodinia: A synthesis.
2507 *Precambrian Research, 160*(1-2), 179-210. doi:10.1016/j.precamres.2007.04.021

2508 Loewy, S. L., Connelly, J. N., Dalziel, I. W. D., & Gower, C. F. (2003). Eastern Laurentia
2509 in Rodinia: constraints from whole-rock Pb and U/Pb geochronology.
2510 *Tectonophysics, 375*, 169-197. doi:10.1016/S0040-1951(03)00338-X

Long, M. D., Benoit, M. H., Chapman, M. C., & King, S. D. (2010). Upper mantle anisotropy and transition zone thickness beneath southeastern North America and implications for mantle dynamics. *Geochemistry Geophysics Geosystems, 11*(10). doi:10.1029/2010GC003247

Long, M. D., Jackson, K. G., & McNamara, J. F. (2016). SKS splitting beneath Transportable Array stations in eastern North America and the signature of past lithospheric deformation. *Geochemistry Geophysics Geosystems, 17*, 2-15. doi:10.1002/2015GC006088

Long, M., Ford, H. A., Abrahams, L., & Wirth, E. A. (2017). The seismic signature of lithospheric deformation beneath eastern North America due to Grenville and Appalachian orogenesis. Lithosphere, 9(5), 987-1001. doi:10.1130/L660.1

Long, M. D., Benoit, M. H., Aragon, J. C., & King, S. D. (2019). Seismic imaging of mid-crustal structure beneath central and eastern North America: Possibly the elusive Grenville deformation? *Geology*, 47(4), 371-374. doi:10.1130/G46077.1

Lynner, C., & Porritt, R. W. (2017). Crustal structure across the eastern North American margin from ambient noise tomography. *Geophysical Research Letters, 44*, 6651-6657. doi:10.1002/ 2017GL073500

Lynner, C., & Bodmer, M. (2017). Mantle flow along the eastern North American margin inferred from shear wave splitting. *Geology, 45*(10), 867-870. doi:10.1130/G38980.1

Maria, A., Hermes, O.D. (2001). Volcanic rocks in the Narragansett basin, southeastern New England. *American Journal of Science, 301,* 286-312. doi: 10.2475/ajs.301.3.286

2534 Ma, X., & Lowry, A. R. (2017). USArray Imaging of Continental Crust in the
2535 Conterminous United States. *Tectonics, 36*(12), 2882-2902.
2536 doi:10.1002/2017TC004540

2537 Martignole, J., & Calvert, A. J. (1996). Crustal-scale shortening and extension across the
2538 Grenville Province of western Québec. *Tectonics, 15*(2), 376-386.
2539 doi:10.1029/95TC03748

2540 Marzoli, A., Renne, P. R., Piccirillo, E. M., Ernesto, M., Bellieni, G., & De Min, A. (1999).
2541 Extensive 200-million-year-old continental flood basalts of the Central Atlantic
2542 Magmatic Province. *Science, 284*(5414), 616-618. doi:
2543 10.1126/science.284.5414.616

2544 Marzoli, A., Callegaro, S., Dal Corso, J., Davies, J. H. F. L., Chiaradia, M., Youbi, N., et
2545 al. (2018). The Central Atlantic Magmatic Province (CAMP): A review. In Tanner,
2546 L. H., (Eds.), *The Late Triassic World, Topics in Geobiology* (Vol. 46, pp. 91-125).
2547 New York, NY: Springer.

2548 Marzen, R. E., Shillington, D. J., Lizarralde, D., et al. (2020). Limited and localized
2549 magmatism in the Central Atlantic Magmatic Province. *Nature Communication,*
2550 *11*, 3397. doi:10.1038/s41467-020-17193-6

2551 Mazza, S. E., Gazel, E., Johnson, E. A., Kunk, M. J., McAleer, R., Spotila, J. A., et al.
2552 (2014). Volcanoes of the passive margin: The youngest magmatic event in eastern
2553 North America. *Geology, 42*(6), 483-486. doi:10.1130/G35407.1

2554 Mazza, S. E., Gazel, E., Johnson, E. A., Bizimis, M., McAleer, R., & Biryol, C. B. (2017).
2555 Post-rift magmatic evolution of the eastern North American “passive- aggressive”
2556 margin. *Geochemistry, Geophysics, Geosystems, 18*. doi:10.1002/ 2016GC006646

McHone, J. G., & Butler, J. R. (1984). Mesozoic igneous provinces of New England and the opening of the North Atlantic Ocean. *Geological Society of America Bulletin, 95*(7), 757-765. doi:10.1130/0016-7606(1984)95<757:MIPONE>2.0.CO;2

McHone, J. G. (2000). Non-plume magmatism and rifting during the opening of the central Atlantic Ocean. *Tectonophysics, 316*(3-4), 287-296. doi:10.1016/S0040-1951(99)00260-7

McLelland, J. M., Selleck, B. W., & Bickford, M. E. (2010). Review of the Proterozoic evolution of the Grenville Province, its Adirondack outlier, and the Mesoproterozoic inliers of the Appalachians. *The Geological Society of America Memoir, 206*(02), 21-49. doi:10.1130/2010.1206(02)

McLelland, J. M., Selleck, B. W., & Bickford, M. E. (2013). Tectonic Evolution of the Adirondack Mountains and Grenville Orogen Inliers within the USA. *Geoscience Canada, 40*(4), 318. doi:10.12789/geocanj.2013.40.022

Meltzer, A., (2011). RAMP Virginia. International Federation of Digital Seismograph Networks. Dataset/Seismic Network. doi:10.7914/SN/YC_2011

Menke W., Levin V., & Darbyshire F., (2012). Deep Structure of Three Continental Sutures in Eastern North America. International Federation of Digital Seismograph Networks. http://www.fdsn.org/networks/detail/X8_2012/

Menke, W., Skryzalin, P., Levin, V., Harper, T., Darbyshire, F., & Dong, T. (2016). The Northern Appalachian Anomaly: A modern asthenospheric upwelling. *Geophysical Research Letters, 43*(19), 10,173-10,179. doi:10.1002/2016GL070918

Montagner, J. (1994). Can seismology tell us anything about convection in the mantle? *Reviews of Geophysics, 32*, 115-37. doi: 10.1029/94RG00099

Mooney, W. D., & Kaban, M. K. (2010). The North American upper mantle: Density, composition, and evolution. *Journal of Geophysical Research: Solid Earth, 115*(12). doi:10.1029/2010JB000866

Mount, V. S. (2014). Structural style of the Appalachian Plateau fold belt, north-central Pennsylvania. *Journal of Structural Geology, 69*(PB), 284-303. doi:10.1016/j.jsg.2014.04.005

Musacchio, G., Mooney, W. D., Luetgert, J. H., & Christensen, N. I. (1997). Composition of the crust in the Grenville and Appalachian Provinces of North America inferred from Vp/Vs ratios. *Journal of Geophysical Research, 102,* 15225-15241. doi:10.1029/96jb03737

Murphy, B. S., & Egbert, G. D. (2019). Synthesizing seemingly contradictory seismic and magnetotelluric observations in the southeastern United States to image physical properties of the lithosphere. *Geochemistry, Geophysics, Geosystems, 20*. doi:10.1029/2019GC008279

Mustelier, E., & Menke, W. (2020). Seismic Anomalies in the Southeastern North American Asthenosphere as Characterized with Body Waves Travel Times from High Qualities Teleseisms. *Tectonophysics.* In press.

Nolet, G. (2008). A breviary of seismic tomography: Imaging the interior of the Earth and Sun. Cambridge: Cambridge University Press. doi:10.1017/CBO9780511984709

Olsen, P. E., Kent, D. V., Et-Touhami, M., & Puffer, J. (2003). Cyclo-, magneto-, and bio-stratigraphic constraints on the duration of the CAMP event and its relationship to

2602 the triassic-jurassic boundary. In Hames, W., Mchone, J. G., Renne, P., Ruppel, C.,
2603 (Eds.), *Geophysical Monograph Series* (Vol. 136, pp. 7-32). Washington, D.C:
2604 AGU, doi:10.1029/136GM02

2605 Park, J., & Levin, V. (2016). Statistics and frequency-domain moveout for multiple-taper
2606 receiver functions. *Geophysical Journal International, 207*(1), 512-527.
2607 doi:10.1093/gji/ggw291

2608 Parker, H. E., Hawman, R. B., Fischer, K. M., & Wagner, L. S. (2015). Constraining
2609 lithologic variability along the Alleghanian detachment in the southern
2610 Appalachians using passive-source seismology. *Geology, 43*(5), 431-434.
2611 doi:10.1130/G36517.1

2612 Pavlis, G. L. (2011). Three-dimensional, wavefield imaging of broadband seismic array
2613 data. *Computers and Geosciences, 37*(8), 1054-1066.
2614 doi:10.1016/j.cageo.2010.11.015

2615 Penn State University. (2004). Pennsylvania State Seismic Network. International
2616 Federation of Digital Seismograph Networks. Other/Seismic Network.
2617 doi:10.7914/SN/PE.

2618 Penn State University. (2013). PASEIS Network. International Federation of Digital
2619 Seismograph Networks. Other/Seismic Network.

2620 Petrescu, L., Bastow, I. D., Darbyshire, F. A., Gilligan, A., Bodin, T., Menke, W., et al.
2621 (2016). Three billion years of crustal evolution in eastern Canada: Constraints from
2622 receiver functions. *Journal of Geophysical Research: Solid Earth, 121*(2), 788-811.
2623 doi:10.1002/2015JB012348

Percival, J. A., Bleeker, W., Cook, F. A., Rivers, T., Ross, G., & van Staal, C. (2004). PanLITHOPROBE workshop IV: Intra-orogen correlations and comparative orogenic anatomy. *Geoscience Canada, 31*(1), 23-39.

Perry, H. K. C., Forte, A. M., & Eaton, D. W. S. (2003). Upper-mantle thermochemical structure below North America from seismic-geodynamic flow models. *Geophysical Journal International, 154*(2), 279-299. doi:10.1046/j.1365-246X.2003.01961.x

Porter, R. C., van der Lee, S., & Whitmeyer, S. J. (2019). Synthesizing EarthScope data to constrain the thermal evolution of the continental U.S. lithosphere. *Geosphere, 15*(6), 1722-1737. doi:10.1130/GES02000.1

Ramsay, T., & Pysklywec, R. (2011). Anomalous bathymetry, 3-D edge driven convection, and dynamic topography at the western Atlantic passive margin. *Journal of Geodynamics, 52*(1), 45-56. doi:10.1016/j.jog.2010.11.008

Rimando, R. E., & Benn, K. (2005). Evolution of faulting and paleo-stress field within the Ottawa graben, Canada. *Journal of Geodynamics, 39*(4), 337-360. doi:10.1016/j.jog.2005.01.003

Rivers, T. (1997). Lithotectonic elements of the Grenville Province: review and tectonic implications. *Precambrian Research, 86*(3-4), 117-154. doi:10.1016/S0301-9268(97)00038-7

Rivers, T. (2015). Tectonic setting and evolution of the Grenville Orogen: An assessment of progress over the last 40 years. *Geoscience Canada, 42*(1), 77-124. doi:10.12789/geocanj.2014.41.057

Robinson, P., Tucker, R. D., Bradley, D., Berry, H. N., & Osberg, P. H. (1998). Paleozoic orogens in New England, USA. *GFF, 120*(2), 119-148. doi:10.1080/11035899801202119

Rondenay, S. (2009). Upper mantle imaging with array recordings of converted and scattered teleseismic waves. Surveys in Geophysics. doi:10.1007/s10712-009-9071-5

Savage, B., Covellone, B. M., & Shen, Y. (2017). Wave speed structure of the eastern North American margin. *Earth and Planetary Science Letters, 459,* 394-405. doi:10.1016/j.epsl.2016.11.028

Stanley, S. M. (1999). Earth system history. New York: Freeman, W. H.

Schmandt, B., & Lin, F. C. (2014). P and S wave tomography of the mantlebeneath the United States. *Geophysical Research Letters, 41*, 6342-6349. doi:10.1002/2014GL061231

Schmandt, B., Lin, F. C., & Karlstrom, K. E. (2015). Distinct crustal isostasy trends east and west of the Rocky Mountain Front. *Geophysical Research Letters, 42*(23), 10290-10298. doi:10.1002/2015GL066593

Schulte-Pelkum, V., Monsalve, G., Sheehan, A., Pandey, M. R., Sapkota, S., Bilham, R., & Wu, F. (2005). Imaging the Indian subcontinent beneath the Himalaya. *Nature, 435*(7046), 1222-1225. doi:10.1038/nature03678

Sella, G. F., Stein, S., Dixon, T. H., Craymer, M., James, T. S., Mazzotti, S., et al. (2007). Observation of glacial isostatic adjustment in “stable” North America with GPS. *Geophysical Research Letters, 34*(2). doi:10.1029/2006GL027081

2668 Shapiro, N. M., & Ritzwoller, M. H. (2002). Monte-Carlo inversion for a global shear
2669 velocity model of the crust and upper mantle. *Geophysical Journal International,*
2670 *151*, 88-105. doi:10.1046/j.1365-246X.2002.01742.x
2671 Shen, W., & Ritzwoller, M. H. (2016). Crustal and uppermost mantle structure beneath the
2672 United States. *Journal of Geophysical Research: Solid Earth, 121*(6), 4306-4342.
2673 doi:10.1007/s13398-014-0173-7.2
2674 Skogseid, J., Planke, S., Faleide, J. I., Pedersen, T., Eldholm, O., & Neverdal, F. (2000).
2675 NE Atlantic continental rifting and volcanic margin formation. *Geological Society,*
2676 *London, Special Publications, 167*(1), 295-326.
2677 doi:10.1144/GSL.SP.2000.167.01.12
2678 Smith, W. H. F., & Sandwell, D. T. (1997). Global seafloor topography from satellite
2679 altimetry and ship depth soundings. *Science, 277*, 1957-1962.
2680 doi:10.1126/science.277.5334.1956
2681 Soto-Cordero, L., Meltzer, A., Stachnik, J. C. (2018). Crustal structure, intraplate
2682 seismicity, and seismic hazard in the Mid-Atlantic United States. *Seismological*
2683 *Research Letters, 89*(1), 241-252. doi:10.1785/0220170084
2684 Spencer, C., Green, A., Morelalhuissier, P., Milkereit, B., Luetgert, J., Stewart, D., et al.
2685 (1989). The extension of Grenville Basement beneath the northern Appalachians:
2686 Results from the Quebec-Maine seismic reflection and refraction
2687 surveys. *Tectonics, 8*(4), 677-696. doi:10.1029/TC008i004p00677
2688 Stanley, R. S., & Ratcliff, N. M. (1985). Tectonic synthesis of the Taconian orogeny in
2689 western New England: *Geological Society of America Bulletin, 96*(10), 1227-1250.
2690 doi:10.1130/0016-7606(1985)96<1227:TSOTTO>2.0.CO;2

Stein, C. A., Stein, S., Elling, R., Randy Keller, G., & Kley, J. (2018a). Is the "Grenville Front" in the central United States really the midcontinent rift? *GSA Today. Geological Society of America, 28*. doi:10.1130/GSATG357A.1

Stein, S., Stein, C. A., Elling, R., Kley, J., Keller, G. R., Wysession, M., et al., (2018b). Insights from North America's failed Midcontinent Rift into the evolution of continental rifts and passive continental margins. *Tectonophysics, 744*, 403-421. doi:10.1016/j.tecto.2018.07.021

Taylor, S. R., & Toksöz, M. N. (1982). Crust and upper-mantle velocity structure in the Appalachian orogenic belt: Implications for tectonic evolution. *Geological Society of America Bulletin, 93*(4), 315-329. doi:10.1130/0016-7606(1982)93<315:CAUVSI>2.0.CO;2

Thomas, W. A. (1977). Evolution of Appalachian-Ouachita salients and recesses from reentrants and promontories in the continental margin. *American Journal of Science, 277,* 1233-1278. doi:10.2475/ajs.277.10.1233

Thomas, M. D., & Teskey, D. J. (1994). An interpretation of gravity anomalies over the Mid-continent Rift, Lake Superior, constrained by GLIMPCE seismic and aeromagnetic data. *Canadian Journal of Earth Sciences, 31*, 682-697, doi:10.1139/e94-061.

Thomas, W. A. (2006). Tectonic inheritance at a continental margin. *GSA Today, 16*(2), 4-11. doi:10.1130/1052-5173(2006)016[4:TIAACM]2.0.CO;2

Till, C. B., Elkins-Tanton, L. T., & Fischer, K. M. (2010). A mechanism for low-extent melts at the lithosphere-asthenosphere boundary. *Geochemistry, Geophysics, Geosystems, 11*(10). doi:10.1029/2010GC003234

Thurber, C. & Aki, K. (1987). Three-dimensional seismic imaging. *Annual Review of Earth and Planetary Sciences 15*, 115-39. doi:10.1146/ 15.050187.000555

UC San Diego. (2013). Central and Eastern US Network. International Federation of Digital Seismograph Networks. Other/Seismic Network. doi:10.7914/SN/N4.

University of Memphis (1982). CERI Southern Appalachian Seismic Network. International Federation of Digital Seismograph Networks. Dataset/Seismic Network.

University of Western Ontario (UWO Canada). (1991). The Southern Ontario Seismic Network. International Federation of Digital Seismograph Networks. Other/Seismic Network.

van Avendonk, H. J. A., Lavier, L. L., Shillington, D. J., & Manatschal, G. (2009). Extension of continental crust at the margin of the eastern Grand Banks, Newfoundland. *Tectonophysics, 468*(1-4), 131-148. doi:10.1016/j.tecto.2008.05.030

van der Velden, A. J., van Staal, C. R., & Cook, F. A. (2004). Crustal structure, fossil subduction, and the tectonic evolution of the Newfoundland Appalachians: Evidence from a reprocessed seismic reflection survey. *Bulletin of the Geological Society of America, 116*(11-12), 1485-1498. doi:10.1130/B25518.1

van Staal, C. R., Whalen, J. B., Valverde-Vaquero, P., Zagorevski, A., & Rogers, N. (2009). Pre-Carboniferous, episodic accretion-related, orogenesis along the Laurentian margin of the northern Appalachians. *Geological Society, London, Special Publications, 327*(1), 271-316. doi:10.1144/SP327.13

van Staal, C.R. & Barr, S.M. (2012). Lithospheric architecture and tectonic evolution of the Canadian Appalachians and associated Atlantic margin. In Percival, J. A., Cook, F .A., & Clowes., R.M. (Eds.), *Tectonic Styles in Canada: the LITHOPROBE Perspective* (Vol. 49, pp. 41-95). Newfoundland, Canada: Geological Association of Canada.

Viegas, G. M., Baise L. G., & Abercrombie R. E. (2010). Regional wave propagation in New England and New York, Bulletin of the Seismological Society of America, 100(5A), 2196-2218, doi:10.1785/0120090223.

Wang, Y. D., Lin, F. C., Schmandt, B., Farrell, J. (2017). Ambient noise tomography across Mount St. Helens using a dense seismic array, *Journal of Geophysical Research: Solid Earth, 122*(6). doi: 10.1002/2016JB013769

Wagner, L., (2009). Appalachian Seismic Transect. International Federation of Digital Seismograph Networks. Dataset/Seismic Network. doi:10.7914/SN/Z4_2009

Wagner, L., (2012). Pre-Hydrofracking Regional Assessment of Central Carolina Seismicity. International Federation of Digital Seismograph Networks. Dataset/Seismic Network. doi:10.7914/SN/XQ_2012

Wagner, L. S., Long, M. D., Johnston, M. D., & Benoit, M. H. (2012). Lithospheric and asthenospheric contributions to shear-wave splitting observations in the southeastern United States. *Earth and Planetary Science Letters, 341*, 128-138. doi:10.1016/j.epsl.2012.06.020

Wagner, L. S., Fischer, K. M., Hawman, R., Hopper, E., & Howell, D. (2018). The relative roles of inheritance and long-term passive margin lithospheric evolution on the

modern structure and tectonic activity in the southeastern United States. *Geosphere, 14*(4), 1385-1410. doi:10.1130/GES01593.1

Wang, Y., & Pavlis, G. L. (2016). Generalized iterative deconvolution for receiver function estimation. *Geophysical Journal International, 204*(2), 1086-1099. doi:10.1093/gji/ggv503

Wang, H., Zhao, D., Huang, Z., & Wang, L. (2019). Tomography, Seismotectonics, and Mantle Dynamics of Central and Eastern United States. *Journal of Geophysical Research: Solid Earth, 124*(8). doi:10.1029/2019JB017478

Whalen, L., Gazel, E., Vidito, C., Puffer, J., Bizimis, M., Henika, W., et al. (2015). Supercontinental inheritance and its influence on supercontinental breakup: The Central Atlantic Magmatic Province and the breakup of Pangea. *Geochemistry, Geophysics, Geosystems, 16*, 3532-3554. doi:10.1002/2015GC005885

White, R., & McKenzie, D. (1989). Magmatism at rift zones: The generation of volcanic continental margins and flood basalts. *Journal of Geophysical Research, 94*, 7685-7729. doi:10.1029/JB094iB06p07685

White, D. J., Forsyth, D. A., Asudeh, I., Carr, S. D., Wu, H., Easton, R. M., & Mereu, R. F. (2000). A seismic-based cross-section of the Grenville Orogen in southern Ontario and western Quebec. *Canadian Journal of Earth Sciences, 37*(2-3), 183-192. doi:10.1139/CJES-37-2-3-183

Whiteside, J. H., Olsen, P. E., Kent, D. V., Fowell, S. J., & Et-Touhami, M. (2007). Synchrony between the Central Atlantic magmatic province and the Triassic-Jurassic mass extinction event? *Palaeogeography, Palaeoclimatology, Palaeoecology, 224*(1-4), 345-367. doi:10.1016/j.palaeo.2006.06.035

Withjack, M. O., Schlische, R. W., & Olsen, P. E. (2012). Development of the passive margin of Eastern North America: Mesozoic rifting, igneous activity, and breakup. *Regional Geology and Tectonics: Phanerozoic Rift Systems and Sedimentary Basins*, 300-335, Elsevier Inc. doi:10.1016/B978-0-444-56356-9.00012-2

Whitmeyer, S., & Karlstrom, K. E. (2007). Tectonic model for the Proterozoic growth of North America. *Geosphere, 3*(4), 220-259. doi:10.1130/GES00055.1

Williams, M. L., Dumond, G., Mahan, K., Regan, S., & Holland, M. (2014). Garnet-forming reactions in felsic orthogneiss: Implications for densification and strengthening of the lower continental crust. Earth and Planetary Science Letters, 405, 207-219. doi:10.1016/j.epsl.2014.08.030

Wintsch, R. P., Kunk, M. J., Boyd, J. L., & Aleinikoff, J. N. (2003). P-T-t paths and differential Alleghanian loading and uplift of the Bronson Hill terrane, south central New England. *American Journal of Science, 303*, 410-446. doi: 10.2475/ajs.303.5.410

Wintsch, R. P., Yi, K., & Dorais, M. J. (2014). Crustal thickening by tectonic wedging of the Ganderian rocks, southern New England, USA: Evidence from cataclastic zircon microstructures and U-Pb ages. *Journal of Structural Geology, 69*(PB), 428-448. doi:10.1016/j.jsg.2014.07.019

Xia, J. H., Miller, R. D., & Park, C. (1999). Estimation of near-surface shear-wave velocity by inversion of Rayleigh waves. *Geophysics, 64*(3). doi:10.1190/1.1444578

Yao, H., et al., Estimation of surface wave Green's functions from correlation of direct waves, coda waves, and ambient noise in SE Tibet. Physics of the Earth and Planetary Interiors. (2009), doi:10.1016/j.pepi.2009.07.002

Yang, X., Pavlis, G. L., Hamburger, M. W., Marshak, S., Gilbert, H., Rupp, J., … Carpenter, N. S. (2017). Detailed crustal thickness variations beneath the Illinois Basin area: Implications for crustal evolution of the midcontinent. *Journal of Geophysical Research: Solid Earth, 122*(8), 6323-6345. doi:10.1002/2017JB014150

Yang, X., & Gao, H. (2018). Full-wave seismic tomography in the northeastern United States: New insights into the uplift mechanism of the Adirondack Mountains. *Geophysical Research Letters, 45*, 5992-6000. doi:10.1029/ 2018GL078438

Yeck, W. L., Sheehan, A. F., & Schulte-Pelkum, V. (2013). Sequential H-κ stacking to obtain accurate crustal thicknesses beneath sedimentary basins. *Bulletin of the Seismological Society of America, 103*(3), 2142-2150. doi:10.1785/0120120290

Yuan, X., Ni, J., Kind, R., Mechie, J., & Sandvol, E. (1997). Lithospheric and upper mantle structure of southern Tibet from a seismological passive source experiment. *Journal of Geophysical Research: Solid Earth,* 102(B12), 27491-27500. doi:10.1029/97JB02379

Zhang, Z., & Shen, Y. (2008). Cross-dependence of finite-frequency compressional waveforms to shear seismic wave-speeds. *Geophysical Journal International, 174,* 941-948. doi:10.1111/j.1365-246X.2008.03840.x

Zhang, W., Shen, Y., & Zhao, L. (2012). Three-dimensional anisotropic seis- mic wave modelling in spherical coordinates by a collocated-grid finite difference method. *Geophysical Journal International, 188,* 1359-1381. doi:10.1111/j.1365-246X.2011.05331.x

Zhao, L., Jordan, T. H., Olsen, K. B., & Chen, P. (2005). Frechet kernels for imaging regional earth structure based on three-dimensional reference models. *Bulletin of the Seismological Society of America, 95,* 2066-2080. doi:10.1785/0120050081